

# Physical Models of the Lunar Wake and Data-Model Comparisons

by

Hossna Gharaee

A thesis submitted in partial fulfillment of the requirements for the degree of

Doctor of Philosophy

Department of Physics

University of Alberta

© Hossna Gharaee, 2019

# Abstract

In this thesis, the lunar wake is investigated with a hybrid-kinetic model to simulate the dynamics of the ions as particles as well as in the fluid approximations. Two-fluid models of the entire wake whether interacting (the method of characteristics) or not (the analytic model) are developed based on a simple single-fluid description of only one edge of the lunar wake. A finite element code is also used to study the lunar wake as a single-fluid and with the two-fluid interacting and, two-fluid non-interacting models. All these models are two dimensional, in a plane of the solar wind velocity and the interplanetary magnetic field (IMF). The orientation of the IMF is one of the essential elements controlling the formation of the wake and is discussed in this thesis. To validate these models, two different IMF oriented in-situ observations of the density in the lunar wake from the ARTEMIS mission are presented. Cross-comparisons between densities calculated by these models are also provided. These 2D models can capture the conical shape of the lunar wake, the density depletion, and the relation between the length of the wake and the IMF orientation. However, the formation of the standing shock wave behind the Moon can only be seen from the finite element approach. A relatively good qualitative and quantitative agreement between the results of the observations and each model is achieved. To check the consistency of the assumptions made in the fluid model, a test particle method is applied to calculate the distribution function of the ions on their trajectories in the terminator very close to the Moon surface by using the approximate fields from an analytic

model. The calculated macroscopic variables from the distribution functions are compared with the ones assumed in the analytic-fluid description, and an excellent agreement is obtained.

# Preface

Parts of Chapter 2 and Chapter 3 of this thesis are based on a paper by H. Gharaee, R. Rankin, R. Marchand, and J. Paral, published in *Journal of Geophysical Research: Space Physics*, doi.org/10.1002/2014JA020907, 2015. In this paper I was responsible for deriving the analytic model presented, in carrying out the calculations, plotting and analyzing the results. R. Rankin and R. Marchand helped with discussions concerning the theoretical approach, and J. Paral provided input for the use of the two-dimensional hybrid code that he had developed. .

*To Mom, Dad, Michael, and Omeed*

# Acknowledgements

I acknowledge funding from the Canadian Space Agency and the Natural Sciences and Engineering Research Council of Canada (NSERC). I want to thank Westgrid Compute Canada as I benefited from access to their facilities for some of my simulations.

I extend thanks to THEMIS software manager Jim Lewis for his help on using ARTEMIS satellite data.

I gratefully acknowledge the assistance of my supervisors Prof. Richard Marchand and Prof. Robert Rankin for their valuable advice.

The completion of my dissertation would not have been possible without the support and nurturing of my co-supervisor Prof. Richard Marchand, who never let me down.

I am grateful to my husband and son Michael and Omeed, who have provided me through moral and emotional support in my life.

Exceptional gratitude goes out to my parents and siblings for their encouragement and care.

Thanks also to my friends by providing a happy distraction to rest my mind outside of my research.

# Contents

<b>1</b>	<b>Introduction</b>	<b>1</b>
1.1	Thesis outline . . . . .	1
1.2	The plasma state . . . . .	4
1.3	The solar wind . . . . .	4
1.4	Obstacles in the solar wind . . . . .	6
1.5	The Moon . . . . .	10
1.6	Different approaches for studying space plasma physics . . . . .	14
1.6.1	Kinetic simulations . . . . .	15
1.6.2	Hybrid models . . . . .	16
1.6.3	Fluid simulations . . . . .	17
1.6.4	Test-particle simulations . . . . .	22
1.6.5	Observations . . . . .	23
<b>2</b>	<b>The method of characteristics</b>	<b>25</b>
2.1	Introduction . . . . .	25
2.2	Approximate analytic models to study the lunar wake . . . . .	26
2.2.1	Single-fluid model of the lunar wake (Hutchinson's model)	26
2.2.2	Two-fluid non-interacting model of the lunar wake (the analytic model) . . . . .	31
2.2.3	Results of the analytic analysis ( $\alpha = 90^\circ$ ) . . . . .	34
2.3	Two-fluid interacting model of the lunar wake (the method of characteristics) . . . . .	40
2.3.1	Results from the method of characteristics (with coupling) and the analytic model (without coupling) ( $\alpha = 90^\circ$ )	48
2.3.2	Comparisons between the method of characteristics and the analytic model ( $\alpha \neq 90^\circ$ ) . . . . .	61
<b>3</b>	<b>Hybrid-kinetic and Finite element models</b>	<b>67</b>
3.1	Hybrid-kinetic model . . . . .	67
3.1.1	Implementation the hybrid code . . . . .	68
3.1.2	Results obtained from the method of characteristics, and the hybrid model . . . . .	71
3.2	Two-dimensional finite element model . . . . .	76
3.2.1	Finite element code validation . . . . .	77
3.2.2	Use of the finite element code for the lunar wake case . . . . .	82
3.2.3	Comparisons between results obtained with the finite element model and the method of characteristics . . . . .	91
3.3	Comparisons between the densities obtained from the method of characteristics, the finite element model, and the hybrid model	93

<b>4</b>	<b>Test-particle simulations</b>	<b>99</b>
4.1	Algebraic expression for parallel velocities . . . . .	100
4.2	Maxwellian distribution function . . . . .	105
4.3	Results . . . . .	105
4.3.1	Moments of the distribution function . . . . .	106
<b>5</b>	<b>Comparisons with ARTEMIS observations</b>	<b>114</b>
5.1	Mapping a 3D wake into 2D . . . . .	115
5.2	Coordinate transformation . . . . .	115
5.3	Results . . . . .	118
5.3.1	Case 1: 13 February 2010 between 08:53 and 09:29 UT	118
5.3.2	Case 2: 13 March 2013 between 08:35 and 09:35 UT . .	123
<b>6</b>	<b>Summary and conclusions</b>	<b>128</b>
	<b>References</b>	<b>134</b>

# List of Tables

1.1	Properties of the solar wind at 1 AU . . . . .	6
1.2	Properties of planets and their moons. . . . .	7
1.3	Early missions on and above the Moon. . . . .	11
1.4	Recent missions on and above the Moon. . . . .	13
3.1	Main similarities and differences between the method of characteristics and the hybrid model . . . . .	71
3.2	Comparisons of computed oblique shock angle analytically and with the finite element code . . . . .	81
3.3	Main similarities and differences between the method of characteristics and the finite element code . . . . .	91
3.4	Main similarities and differences between the finite element model and the hybrid models . . . . .	94
4.1	Comparisons between the moments calculated from the distribution function and the assumption of the analytic model . . .	112

# List of Figures

1.1	Schematic diagram of solar wind interactions with different obstacles in the solar system. . . . .	3
1.2	The 2D structure of the Parker spiral. . . . .	5
1.3	Schematic illustration of the Earth magnetosphere . . . . .	8
1.4	Schematic illustration of the lunar orbit . . . . .	9
1.5	ARTEMIS spacecraft near the lunar wake. . . . .	14
1.6	Different approaches to studying space plasma physics . . . . .	15
2.1	Illustration of the unperturbed solar wind and lunar wake regions	27
2.2	The angle between the magnetic field and the solar wind flow velocity. . . . .	33
2.3	Normalized plasma density in the approximate analytic model ( $\alpha = 90^\circ$ ) . . . . .	36
2.4	Parallel velocity in the approximate analytic model ( $\alpha = 90^\circ$ )	37
2.5	Normalized plasma parallel flux in the approximate analytic model ( $\alpha = 90^\circ$ ) . . . . .	39
2.6	Normalized density in the method of characteristics ( $\alpha = 90^\circ$ )	48
2.7	Differences in absolute value between the total density in the method of characteristics and the approximate analytic model ( $\alpha = 90^\circ$ ) . . . . .	51
2.8	Normalized total density in the method of characteristics and the approximate analytic model ( $\alpha = 90^\circ$ ) . . . . .	53
2.9	Parallel velocity in the method of characteristics ( $\alpha = 90^\circ$ ) . .	54
2.10	Parallel velocity in the method of characteristics and the approximate analytic model ( $\alpha = 90^\circ$ ) . . . . .	56
2.11	Normalized plasma parallel flux in the method of characteristics ( $\alpha = 90^\circ$ ) . . . . .	57
2.12	Normalized total parallel flux in the method of characteristics and the approximate analytic model ( $\alpha = 90^\circ$ ) . . . . .	58
2.13	Normalized parallel flux 1 in the method of characteristics and the approximate analytic model ( $\alpha = 90^\circ$ ) . . . . .	60
2.14	Normalized plasma parallel flux in the method of characteristics ( $\alpha = 33^\circ$ ) . . . . .	62
2.15	Normalized total density in the method of characteristics and the approximate analytic model ( $\alpha = 33^\circ$ ) . . . . .	63
2.16	Normalized total parallel flux in the method of characteristics and the approximate analytic model ( $\alpha = 33^\circ$ ) . . . . .	65
2.17	Total density with the method of characteristics for $\alpha = 30^\circ$ , $\alpha = 60^\circ$ and $\alpha = 90^\circ$ . . . . .	66
3.1	Perpendicular Mach number in the hybrid simulation ( $\alpha = 90^\circ$ )	73
3.2	Normalized ion density in the hybrid simulation ( $\alpha = 90^\circ$ ) . .	73

3.3	Ion density in the hybrid code and the method of characteristics ( $\alpha = 90^\circ$ ) . . . . .	75
3.4	Oblique shock illustration . . . . .	79
3.5	Oblique shock computed with the finite element model . . . . .	81
3.6	The orientation of the interplanetary magnetic field $\mathbf{B}$ and velocity (Mach number) in the solar wind $M_{sw}$ . . . . .	84
3.7	The domain of the lunar wake in the TOPO code. . . . .	86
3.8	Normalized total density from the finite element code for three different cases. . . . .	87
3.9	Parallel Mach number from the finite element code for three different cases. . . . .	89
3.10	Normalized total parallel flux computed with the finite element code for three different cases. . . . .	90
3.11	Ion density in the finite element code and the method of characteristics ( $\alpha = 90^\circ$ ) . . . . .	95
3.12	Normalized total density from finite element and the hybrid model at $X = 5R_M$ , and $X = 3R_M$ . . . . .	96
3.13	Normalized total density from finite element and the hybrid model at $X = 7 R_m$ , and $X = 8 R_m$ . . . . .	97
3.14	Normalized total density from finite element model, the hybrid model and, the method of characteristics along $Y$ at different cuts in $X$ . . . . .	98
4.1	Geometry of lunar wake . . . . .	101
4.2	Negative characteristic vs $M_{1\parallel}$ . . . . .	103
4.3	Lunar Wake boundaries . . . . .	104
4.4	A curve region where the test-particle calculations are made. . . . .	106
4.5	Distribution function of ions at $\eta = -0.45\pi$ & $-0.40\pi$ . . . . .	107
4.6	Distribution function of ions at $\eta = -0.35\pi$ & $-0.30\pi$ . . . . .	108
4.7	Density calculated from moment of the distribution function and the analytic model . . . . .	109
4.8	Calculating $M_\perp$ from distribution function obtained with test-particle code . . . . .	110
4.9	Variations of $v_z$ in the test-particle code . . . . .	110
4.10	Parallel Mach number calculated from the analytic model and the test-particle code . . . . .	111
4.11	Diagonal elements of pressure tensor of the test-particle code with the Analytic pressure . . . . .	113
5.1	2D plane of $\mathbf{V}_{SW}$ and $\mathbf{B}$ . . . . .	116
5.2	The coordinates related to the trajectory of P1 spacecraft of ARTEMIS mission(Case 1) . . . . .	118
5.3	Trajectory of P1 spacecraft of ARTEMIS mission (Case 1) . . . . .	119
5.4	Ion density in ARTEMIS data with the method of characteristics ( $\alpha = 90^\circ$ ) . . . . .	120
5.5	Ion density from the finite element model and ARTEMIS data ( $\alpha = 90^\circ$ ) . . . . .	122
5.6	Ion density from the method of characteristics, finite element model and, ARTEMIS data ( $\alpha = 90^\circ$ ) . . . . .	123
5.7	Trajectory of p1 spacecraft of ARTEMIS mission (Case 2) . . . . .	124
5.8	Coordinates related to the trajectory of P1 spacecraft of ARTEMIS mission (Case 2) . . . . .	125
5.9	Ion density from the method of characteristics, finite element model and, ARTEMIS data ( $\alpha = 33^\circ$ ) . . . . .	126

5.10 Ion density from the method of characteristics and finite element model ( $\alpha = 33^\circ$ ) . . . . .	127
---	-----

# Chapter 1

## Introduction

### 1.1 Thesis outline

In this chapter, a short introduction to the interaction between the solar wind and obstacles in the solar system is given with a particular emphasis on lunar-type interactions. Kinetic and fluid models to study the dynamics of plasma in the lunar wake are described. In addition a short review of the missions that have been sent to investigate the lunar wake is briefly presented.

In Ch. 2, a set of two-fluid equations is presented for describing the parallel expansion of ions in the wake region of a Moon-like object. These equations are then solved fully analytically following an approach proposed by Hutchinson [31]. In this solution, assumptions are made and justified that reduce the wake problem to be cast as a two-dimensional problem in the plane defined by the solar wind velocity and the local interplanetary magnetic field. Hutchinson [31] developed a simple single-fluid model to study only one edge of the lunar wake by assuming that the magnetic field and the perpendicular velocity are constant. Hutchinson's original model is then extended to account for the interaction between two fluid flows entering the wake from different directions, that are counterstreaming in the direction parallel to the magnetic field. Then the interacting two-fluid equations are solved with "the method of characteristics" for the first time in this thesis. The results of these two-fluid models (the analytic model and the method of characteristics) are discussed and compared. The good qualitative and quantitative agreement between the two models validate the assumption of ignoring the coupling between the two

ion fluids.

In Ch. 3, other computer models to simulate the wake of the Moon are presented. Paral's hybrid code [58] and a finite element code [48] are modified and used for simulating the wake downstream of the Moon. The density profiles calculated from these models are then compared. The finite element model can capture shock waves forming in the lunar wake as predicted by [53], [54] while the hybrid model does not demonstrate the sharp density depletion in the wake. Results obtained with these models are compared with ones calculated with the method of characteristics and are found to be in good qualitative agreement.

In Ch. 4, a test-particle code [50] is applied to calculate the trajectory of ions by using the electric fields obtained from the analytic model. By taking moments of the computed distribution functions, the consistency of assumptions made in the derivation of the two-dimensional fluid model can be checked. The calculated moments from the distribution function are in general agreement with the ones assumed in the analytic model, although differences appear when looking at details of the moments and the distribution function in the wake region.

In Ch. 5, data from two different IMF oriented "Acceleration, Reconnection, Turbulence and Electrodynamics of the Moon's Interaction with the Sun", ARTEMIS, satellite observations are reported. Measured densities from ARTEMIS are compared with densities computed from all models presented in this thesis. Similarities and differences are also discussed.

In Ch. 6, a summary of the findings in this thesis along with some concluding remarks, and possible topics for future work are presented.

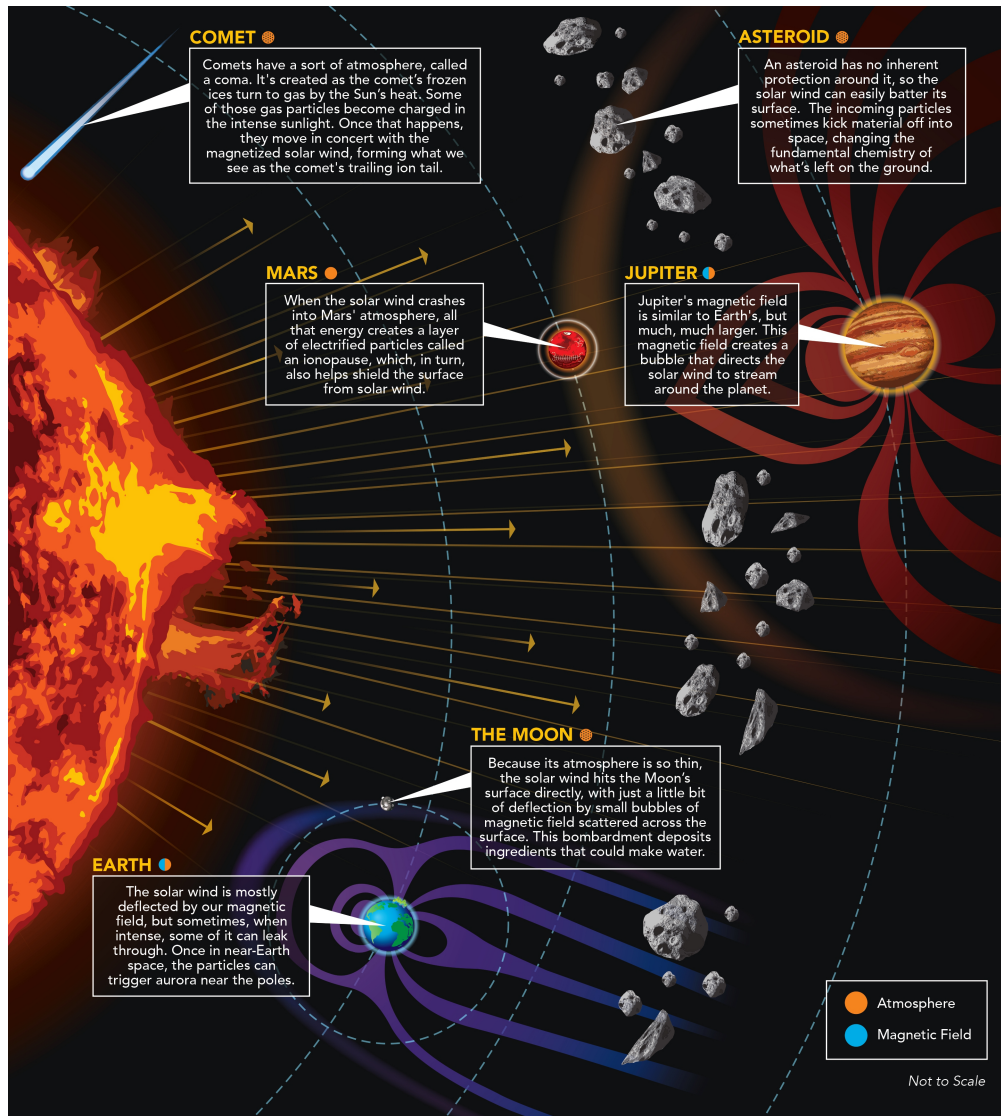


Figure 1.1: Schematic diagram of solar wind interactions with different obstacles in the solar system [courtesy of NASA].

## 1.2 The plasma state

Plasma is described as a quasineutral gas of charged particles that exhibit collective behavior [7]. In fact, the plasma is able to rearrange its charged particles (electrons and ions) to be locally neutral. The volume enclosing this neutral area of the plasma is called the Debye sphere. This means that a plasma approaches neutrality if one looks at it on a scale larger than the radius of this sphere. The electron Debye length,  $\lambda_{De}$  is defined as,

$$\lambda_{De} = \left( \frac{\epsilon_0 k T_e}{n_e e^2} \right)^{1/2}, \quad (1.1)$$

where,  $\epsilon_0 = 8.85^{-12} \text{ C}^2/\text{Nm}^2$  is the free space permittivity,  $k = 1.38 \times 10^{-23} \text{ J/K}$  is the Boltzmann constant,  $n_e$  is electron number density,  $T_e$  is electron temperature, and  $e$  is electron charge. In order for a plasma to be quasineutral, the length scale of the system must be large compared to the Debye length which is one of the criteria for an ionized gas to behave a plasma. In addition, the number of particles inside the sphere with radius of Debye length must be much larger than 1 to meet the second criterion for being a plasma. Another important characteristic of a plasma is called the plasma frequency  $\omega_{pe}$  which is defined as,

$$\omega_{pe} = \left( \frac{n_e e^2}{\epsilon_0 m_e} \right)^{1/2}, \quad (1.2)$$

where,  $m_e$  is the electron mass. The average time between two collisions,  $\tau_n$ , must be larger than the inverse of the plasma frequency which is the third criterion for an ionized medium to be in a state of plasma [2], [3], [7], [20].

## 1.3 The solar wind

The solar wind is a stream of charged particles flowing outward from the sun. The outer layer of the sun's atmosphere, the corona, gets to a very high temperature, around  $10 \times 10^6 \text{ K}$ . The gravity of the sun is not sufficiently strong to confine plasma particles at such temperatures, which then extend out into interplanetary space and become the source of the solar wind. In other words the gas pressure differences between the solar corona and the interstellar space

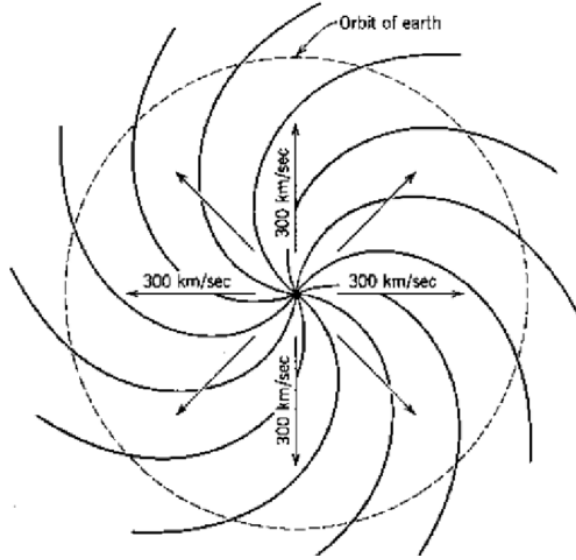


Figure 1.2: The 2D structure of the Parker spiral. (Figure from a paper by Krista 2012 [42])

make the plasma stream out into the interplanetary space at speeds ranging between  $\sim 300 - 1400$  km/s [2]. The temperature of the corona decreases gradually to a value of the order  $10^5$  K at the Earth orbit [29]. Another important physical parameter, besides the temperature and velocity, is the interplanetary magnetic field (IMF). Because the solar wind plasma is highly conductive, the interplanetary magnetic field (IMF) does not diffuse efficiently across the plasma. The magnetic field lines are "frozen in"; that is, they are constrained to move with the plasma [41]. The solar rotation combined with the radial expansion of the solar wind, cause the frozen-in interplanetary magnetic field lines to take a spiral shape known as the Parker spiral [59], [42].

Table 1.1 shows some of the typical properties of the solar wind at one astronomical unit ( $1 \text{ AU} = 1.5 \times 10^{13}$  cm). These parameters can change significantly and abruptly in time depending on space weather conditions. This is the case in particular in a solar storm, during which solar wind plasma density and speed can increase by more than 100%.

Speed	300-1400 km/s
Density	1-10 cm <sup>-3</sup>
Magnetic field	1-7 nT
Sound speed	60 km/s
Alfvén speed	40 km/s
Proton gyroradius	80 km
Temperature	1-8×10 <sup>5</sup> K

Table 1.1: Some of the observed and derived properties of the solar wind near the orbit of the Earth (1 AU) which are taken from Kivelson and Russell [41].

## 1.4 Obstacles in the solar wind

The plasma flows outward from the Sun supersonically and super-Alfvénically into the solar system. In fact, it carries charged particles and magnetic fields which interact with planets, moons, and other bodies in the solar system. Plasma in the solar wind is approximately collisionless. The objects that the solar wind interacts with are very different in size, from submicrometer dust to giant planets (refer to Fig. 1.1). They also have various degrees of magnetization, internal conductivity, and atmospheric density [22]. The nature of this interplay depends on the characteristics of the obstacle. Table 1.2 shows some of the main characteristics for a number of the planets and some of their moons in the solar system [9]. There are four types of object-solar wind interactions in the solar system that can be identified. They are as follows:

**1-Lunar type:** This class of interaction is characterized by the absence of an atmosphere for an unmagnetized planet. The solar wind directly impacts the surface of the unmagnetized object and is absorbed by it. With this type of interaction, a vacuum region, or wake appears downstream of the body. There are various factors at play in this type of interaction such as, the size of the unmagnetized body, the typical solar wind Debye length which is  $\sim 10$  m, the ion and electron gyroradii  $r_{gi} \sim 120$  km and  $r_{ge} \sim 3$  km, the ion Mach cone angle  $\tan^{-1}(C_s/V_{SW}) \sim 6^\circ$ , where  $C_s \sim 42$  km/s is the ion sound speed and  $V_{SW} \sim 400$  km/s is the solar wind flow speed. For smaller objects, that are comparable in size to the Debye length, the day and night processes

Table 1.2: Some of the main properties of the planets and their moons in the solar system which are taken from Cravens 1997's book [9].

Planet	Mass ( $10^{23}$ kg)	Equatorial Radius (km)	Average heliocentric distance (AU)
Mercury	3.33	2,439	0.46
Venus	48.7	6,050	0.72
Mars	6.42	3,398	1.52
Earth	59.8	6,378	1
Jupiter	18,990	71,400	5.2
Saturn	5,686	60,330	9.51
Moon	0.73	1,737	384,400 km to Earth
Io	0.89	1816	421,700 km to Jupiter
Titan	1.36	2,575	$1.2 \times 10^6$ km to Saturn
Phobos	$10.6 \times 10^{15}$ kg	11.267	9380 km to Mars

Planet	Period of rotation(days)	Magnetic dipole moment relative to Earth	Surface pressure of atm. (bar)
Mercury	58.6	$3.8 \times 10^{-4}$	$10^{-14}$
Venus	-243	$< 5 \times 10^{-5}$	80
Mars	1.03	$< 2 \times 10^{-4}$	$5 \times 10^{-3}$
Earth	1	1.0	1
Jupiter	0.41	$1.9 \times 10^4$	0.3
Saturn	0.43	$6.0 \times 10^2$	0.5
Moon	27.3	0	0
Phobos	0.32	0	0
Titan	15.9	0	1.50
Io	0.77	0	$(0.3-3.0) \times 10^{-9}$

1

AU= $1.49 \times 10^6$  km

Earth's magnetic dipole moment is  $7.9 \times 10^{15} \text{Tm}^3$

can be intertwined. However, in the Moon case, the lunar size  $R_m$  is much larger than the Debye length  $R_m \gg c/\omega_{pi} \gg \lambda_D$  and a wake is formed on the night side which is clearly distinct from the processes occurring on the dayside [5], [16], [22], [79]. The Earth's Moon, asteroids, and certain satellites of other planets such as Phobos (Mars) are in this category. A full description of this type of interaction will be discussed later in Ch. 2.

**2-Earth type:** The strong magnetic field of these objects creates a

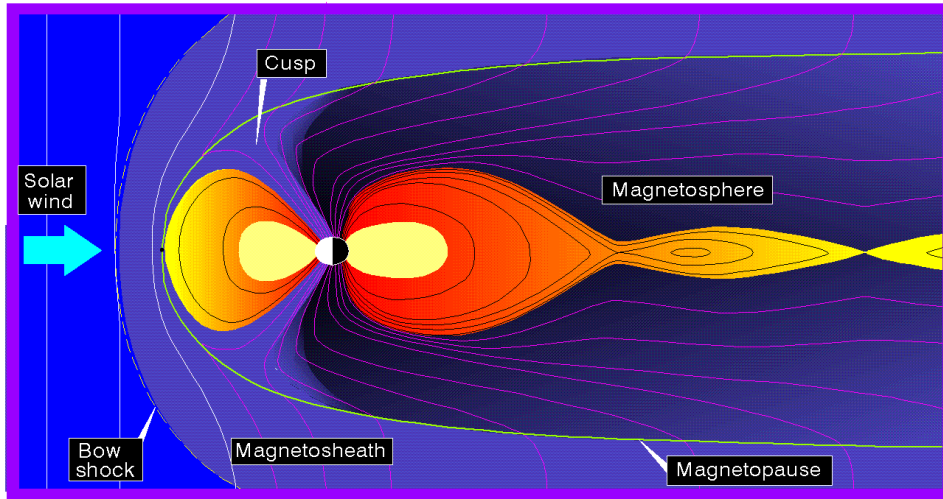


Figure 1.3: Schematic illustration of the Earth magnetosphere, and the regions of importance such as, Bowshock, Magnetopause. (taken from <http://bloggie-360.blogspot.com/2014/03/us-magnetic-field-map-from-w3.html>)

magnetosphere which prevents the solar wind from penetrating into it. As a consequence a bow shock appears upstream in the solar wind flow around the magnetosphere obstacle (see Fig. 1.3). On the dayside of the planet, the magnetic field is compressed by the solar wind dynamic pressure and, On the nightside, the magnetic field is confined into a long tail stretching anti-sunward [25]. The Earth, Mercury, and Jupiter belong to this kind of interplay.

**3-Venus type:** These celestial bodies are not magnetized but they have a dense atmosphere and ionosphere. Ionospheric plasma is a very good electrical conductor that can act as an obstacle to the solar wind flow and cause a bow

shock. Mars, Titan and, Venus are among this group.

*4-Comet type:* Comets are unmagnetized bodies which are composed of rock, dust, water and, frozen gases. When they are close to the Sun, the frozen gases sublimate, producing a coma. In this case they are in a Venus type group. Otherwise, when they are far from the Sun, their interaction with the solar wind is of the lunar-type [9], [46].

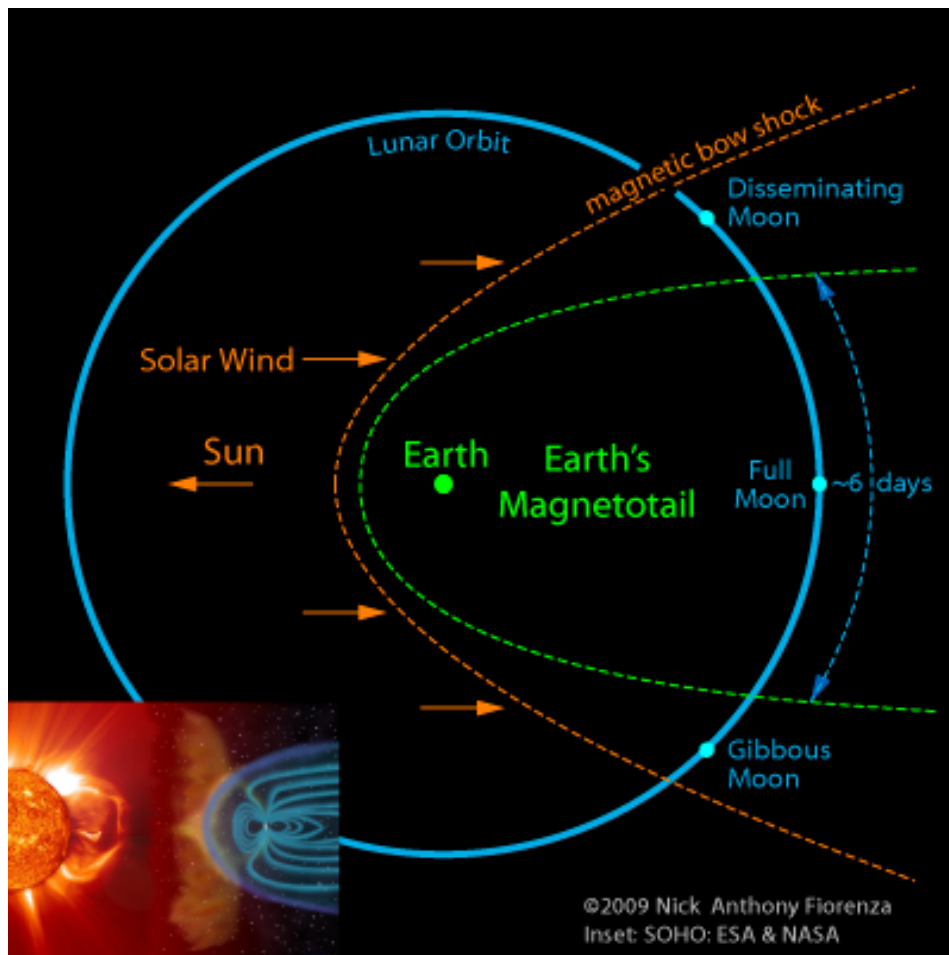


Figure 1.4: Schematic illustration of the lunar orbit. Taken from NASA's illustration Inset: SOHO: ESA and NASA [courtesy of NASA].

## 1.5 The Moon

The Moon orbits the Earth with an orbital radius of  $\simeq 60R_E$  ( $R_E = 6,378$  km). The Moon passes through different regions such as solar wind and the Earth's magnetotail as is illustrated in Fig. 1.4. The density and energy of the plasma at the Moon varies widely in each of these regions. Different types of plasma hit the lunar surface as the Moon does not have a global magnetic field or a thick atmosphere. As the solar wind flows supersonically through the solar system, it interacts with the Moon. The lunar surface can absorb the plasma on the day-side and a plasma density depletion region, or wake is formed on the night-side. Electrons which are lighter, more mobile, and have a higher thermal speed fill the wake ahead of ions. Then, ions are accelerated into the wake because of the resulting the ambipolar electric field. The simple theory of plasma expansion into the wake predicts the density decreases exponentially from its edge towards its center which was seen by the WIND spacecraft crossing the lunar wake at a distance of 6.5 lunar radii ( $R_m$ ) on December 1994 [56]. Simple one-dimensional self-similar solutions have been derived to investigate electron parameters and magnetic field perturbations in the lunar wake for plasma expansion into the wake and considering a non-Maxwellian distribution function for electrons [21]. Such simple one-dimensional models of expansion used in the above papers cannot explain the velocity of ions parallel to the magnetic field filling the lunar wake because they do not account for the spherical shape of the Moon [19], [21], [56], [64].

An analytic self-consistent electrostatic expansion model of the near-Moon wake has also been derived and applied to predict the proper velocity of ions which was observed by the Chandrayaan-1 spacecraft [30], [31], [33].

Studying the Moon-solar wind interaction is of interest because of possible future inhabited missions to the Moon. The night-side of the Moon downstream of the solar wind, has been studied from the Explorer 35 and Apollo missions which made the first observations of the lunar wake [39], and more

Table 1.3: Some of the early missions on and above the Moon. Modified from [25] and <https://www.nationalgeographic.com/science/space/space-exploration/moon-exploration/>

Mission	Year	Instrument	Note
Luna 2, Soviet Union	1959	Magnetometer	First spacecraft landed on the Lunar surface.
Luna 3, Soviet Union	1959		Captured the first images of the Moon's far-side.
Luna 9, Soviet Union	1966		The first vehicle to land safely on the surface.
Luna 10, Soviet Union	1966	Magnetometer, charged particle detector	The first spacecraft to orbit the Moon.
LRO, USA	1966-1967	An imaging system	%99 of the lunar surface was photographed for the subsequent crewed landings.
Explorer 35, USA	1967-1973	Magnetometer, Faraday cup plasma detector	
Apollo 11, USA	1969		The first mankind lands on the Moon.
Apollo 12, USA	1969-1977	Magnetometer, Faraday cup, plasma detector, electrostatic ion analyzer	To explore the surface.
Apollo 14, USA	1971-1977	Magnetometer, Faraday cup plasma detector, electrostatic ion analyzer, electrostatic electron and ion analyzer	
Luna 24, Soviet Union	1976		The last spacecraft to land on the Moon.

recently, by the ARTEMIS flybys through the lunar wake [1]. The important features of the Moon and solar wind interactions were discovered with Explorer 35 observations such as the formation of the lunar wake behind the Moon because of the absorption of solar wind plasma by the lunar surface [47]. Ambipolar electric fields near the boundary of the lunar wake were another fundamental feature of the lunar wake captured by the observations in the 1990s [25] and [56]. In fact, the inner planets can give us a clearer picture of the history of the solar system. In this case, the Moon constitutes a valuable stepping stone for better understanding the origin of the solar system. The original state of this natural satellite is not altered by volcanism, plate tectonics, and atmospheric processes that tend to destroy the information on the Venus-type planets [10], [39]. Knowing more about the Moon can therefore provide valuable information on the early formation of the solar system, and on the evolution of other terrestrial planets such as Mars and Venus. In order to achieve this purpose, robots and/or humans may travel to the lunar surface in the near future. Future missions require an excellent understanding of space conditions in the Moon environment in order to yield optimal scientific results. Several missions have already been sent to study this environment and the interaction between the solar wind and the Moon, including the structure of the wake. Tables 1.3 and 1.4 list some of the missions on and in orbit around the Moon.

Table 1.4: Some of the recent missions on and above the Moon. Modified from [25] and <https://www.nationalgeographic.com/science/space/space-exploration/moon-exploration/>

Mission	Year	Instrument	Note
Wind, USA	1994	Magnetometer, electric field sensor, Faraday cup plasma detector, electrostatic electron and ion analyzer	
NOZOMI, Japan	1998	Electrostatic electron and ion analyzer	
Lunar Prospector, USA	1998-1999	Magnetometer, electrostatic electron analyzer	Confirmed the ice at the lunar poles.
Kaguya, Japan	2007-2009	Magnetometer, electric field sensor, electrostatic electron and ion analyzer	
Chandryaan-1, India	2008-2009	Electrostatic ion analyzer, energetic neutral atom analyzer	
LRO, USA	2009		Found super cold temperature on the surface.
Chang-E2, China	2010-2011	Electrostatic ion analyzer	
ARTEMIS, USA	2010-Present	Magnetometer, electric field sensor, electrostatic electron and ion analyzer, solid state telescope (electron, ion)	
Chang-E4, China	2019		First landing on the far-side.

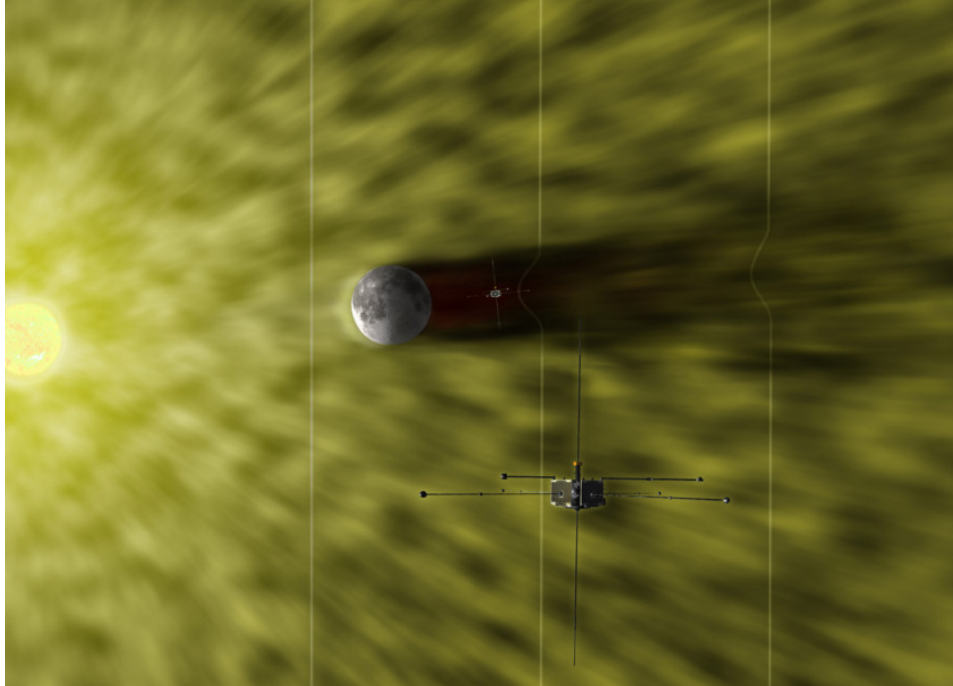


Figure 1.5: Illustration of the ARTEMIS spacecraft near the lunar wake. Taken from: <http://www.planetary.org/multimedia/space-images/earth/artemis-lunar-wake.html>

## 1.6 Different approaches for studying space plasma physics

Traditionally, a complex physical system has been investigated through experiments and theoretical approaches. Computer modeling has been used in scientific research to simulate different physical systems. To validate a model, its results should be compared with observations. In addition, the results of simulation models can be used to predict the findings of the experiments that have not been done or are even doable [11]. Obviously, computer simulations have an essential role in the development of plasma physics (see Figure 1.6). John Dawson and Oscar Buneman were pioneers in the use of computers to simulate plasma by following large numbers of particles in the late 1950's and early 1960's [6]. In general, computer simulations of a plasma are classified into two main groups: *kinetic and moment descriptions*.

### Different Approaches to study Space Plasma Physics

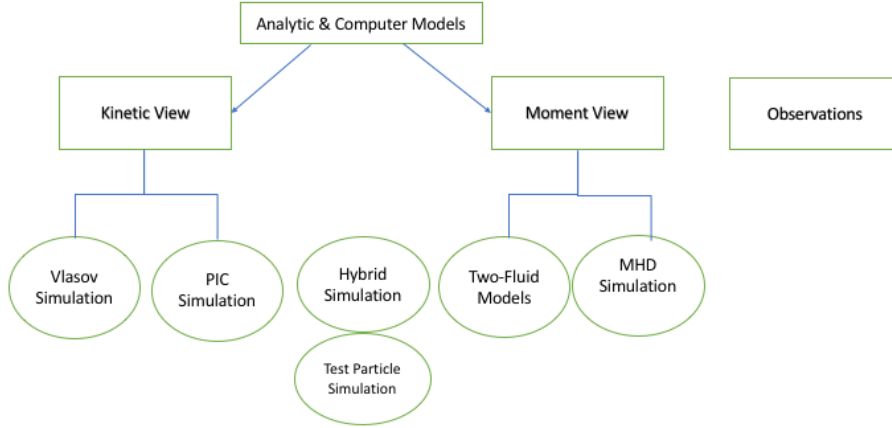


Figure 1.6: Different approaches to studying space plasma physics.

#### 1.6.1 Kinetic simulations

Kinetic simulations provide a macroscopic and comprehensive microscopic picture of a plasma, including the interactions between particles and electromagnetic fields. The physics of individual particles is investigated by either numerically solving the plasma kinetic equations or computing the motion of a group of charged particles in their self-consistent electric and magnetic fields as is done for example, in Particle In Cell (PIC) simulations. In PIC codes the interplay between particles together with the external fields are considered [11]. In kinetic models, each particle is characterized by position  $\mathbf{r}$  and velocity  $\mathbf{v}$  in phase space. The probability density of points in this  $(\mathbf{r}, \mathbf{v})$  space at the time  $t$  is proportional to the distribution function  $f(\mathbf{r}, \mathbf{v}, t)$ , which is a function of seven independent variables  $f(x, y, z, v_x, v_y, v_z, t)$  [60]. Actually, by taking the total time derivative of  $f$  and ignoring the collisional forces in comparison with collective interaction, one of the fundamental equations of motion for collisionless plasma, the Vlasov equation (1.3), is derived. The Vlasov equation governs the evolution of the distribution function in phase space.

$$\frac{\partial f}{\partial t} + \mathbf{v} \cdot \nabla f + \frac{q}{m} \left( \mathbf{E} + \frac{\mathbf{v} \times \mathbf{B}}{c} \right) \cdot \frac{\partial f}{\partial \mathbf{v}} = 0, \quad (1.3)$$

where  $\mathbf{E}$  and  $\mathbf{B}$  are electric and magnetic fields, respectively. It is important to realize that people have already studied the Moon-solar wind interactions kinetically. For example, Farrell et al. [12] used a 1D electrostatic PIC code to study different features of the lunar wake. They showed that the counter-streaming ion beams which are generated by ambipolar E fields are consistent with WIND observations. In addition, a 2D electromagnetic PIC simulation predicts that the negatively charged lunar surface can generate an intense electric field that is in the same direction as the ambipolar electric field at the wake edge [40]. Tao et al. [68] also performed kinetic simulations with a 1-D Vlasov code and showed that the observed electrostatic waves by the Acceleration, Reconnection, Turbulence and Electrodynamics of the Moon's Interaction with the Sun (ARTEMIS) satellite are on the electron beam mode branch.

### 1.6.2 Hybrid models

In this method ions are treated kinetically, and electrons as a fluid. Hybrid codes are used to model phenomena that occur on shorter time and distance scales than can be treated with the MHD formalism and yet do not resolve processes that occur on electron particle scales. The relevant scales are then the ion gyro-radius and ion inertial length for spacial scales, and inverse ion gyrofrequency for time scale. In space physics, these length scales typically are on the order of 10's to 100's of Km and times are on the order of seconds. These ion scales are readily resolved by satellite instrumentation [45], [63], [76]. With attention to the Moon-solar wind interactions, Kallio [38] presented the first 3D hybrid simulation of the Moon-solar wind interaction and showed that a long tail ( $> 10R_m$ ) of depleted plasma density forms on the night side, along with an enhancement of the magnetic field in the wake boundary and a decreased field in the center of the wake. Wang et al. [74] used a 3D hybrid code to study electromagnetic disturbances in the solar wind, and showed that the magnetic field was enhanced by a factor of about 1.4 in the middle of the lunar wake, with depletion at the two sides due to the lunar absorption effect. A

similar approach used by Holmstrom et al.[28] predicts the occurrence of kinks in the magnetic field at the wake boundary. In addition, Wiehle et al. [75] used the dynamic solar wind data as input parameters to the 3D hybrid code to show that the magnetic field tilt (nonzero x-component of magnetic field) causes an asymmetry in the velocity magnitude. In Ch. 3 a 2D hybrid code is applied to simulate the lunar wake.

### 1.6.3 Fluid simulations

In problems with slow time variations, it is more convenient to calculate certain macroscopic averages such as, particle density and thermodynamical pressure instead of the microscopic information of the distribution function [2]. Fluid dynamics treats a group of particles as an entity and the particles are considered to be non-interacting [20], [60]. Conservation equations are solved in the fluid description. By multiplying the Vlasov equation by powers of velocity and integrating over all of velocity space, fluid equations are derived,

**-Zeroth moment:** Equation (1.3) is multiplied by ( $v^0 = 1$ ) and integrated over the velocity space  $V$ , which gives the continuity equation in real space,

$$\frac{\partial n_s}{\partial t} + \nabla \cdot (n_s \mathbf{V}_s) = 0. \quad (1.4)$$

It states that by changing the number density per unit volume in time, particles are leaving the volume to conserve the number density. Here,  $n_s \mathbf{V}_s$  is known as the number flux,  $\mathbf{V}_s$  is the flow velocity,  $n_s$  is the average number density, and the subscript  $s$  represents a species.

**-First moment:** If the Vlasov equation is multiplied by ( $\mathbf{V}^1 = \mathbf{V}$ ) and integrated over the entire velocity space  $V$ , the result is,

$$\frac{\partial(m_s n_s \mathbf{V}_s)}{\partial t} + \nabla \cdot (m_s n_s \mathbf{V}_s \mathbf{V}_s) = n_s q_s (\mathbf{E} + \mathbf{V}_s \times \mathbf{B}) - \nabla \cdot \overleftrightarrow{\mathbf{P}}_s. \quad (1.5)$$

This is the *momentum* equation which shows that the momentum is conserved. In Eq. 1.5,  $\overleftrightarrow{\mathbf{P}}_s$  is the stress tensor and  $m_s$  is the mass corresponding to species  $s$ . The first and the second terms on the left side of this equation correspond

to the time and spatial variations of momentum per unit volume respectively. With some transformations, and considering the continuity equation (1.4), the left side of this equation can be expressed as the total time derivative,

$$\frac{d\mathbf{V}_s}{dt} = \frac{\partial\mathbf{V}_s}{\partial t} + (\mathbf{V}_s \cdot \nabla)\mathbf{V}_s. \quad (1.6)$$

Equation (1.6) in fluid mechanics is called the convective derivative. Henceforth, the right-hand side of the momentum equation represents the forces per unit volume; the first term is the electromagnetic force, the second term is the pressure gradient force [20], [43], [44], [60].

By increasing the moments new useful equation can be obtained but they do not form a closed set of equations, because the numbers of unknowns are more than the numbers of equations. Therefore some other assumptions need to be made according to the specific problem. Actually, the  $n$ th moment equation contains  $n + 1$  unknowns. The closure problem is settled by specifying the  $n+1$ th unknown in terms of the first  $n$  moments. For instance, if the continuity and momentum equations need to be solved, the pressure tensor  $\overleftrightarrow{\mathbf{P}}_s$  should be defined in terms of  $n_s$  or  $v_s$ . These ad hoc assumptions are often taken from thermodynamical considerations. For the different fluid components such as electrons or ions, the equation of state is chosen differently. Next, some of these assumptions are mentioned.

**-Ideal gas :** An ideal gas is a gas of non-interacting particles. The only interaction between particles in the ideal gas would be an elastic collision. In fact there is not any spatial correlations among the particles [61]. An ideal gas is identified by three macroscopic variables; the number of particles  $N$ , the space volume  $V$ , and the thermodynamic temperature  $T$ ,

$$pV = NkT = nRT, \quad (1.7)$$

where,  $n$  is the total number of moles in the system,  $N = nN_A$  and  $N_A$  is the Avogadro number. In addition,  $R = kN_A$  is the gas constant and the universal constant  $K = 1.38 \times 10^{-23} \text{ m}^2 \text{ kg s}^{-2}\text{K}^{-1}$  is the Boltzmann constant,

$$p_s = n_s k T_s, \quad (1.8)$$

where  $n_s$ ,  $p_s$  and,  $T_s$  are the density, pressure and temperature of species  $s$  in the ideal gas law equation of state.

**-The adiabatic equation of state:** On one hand, the adiabatic equation of state is used when the gas is compressed so fast that there is not enough time for heat to flow. On the other hand, the compression of a gas should be slow enough that collisions can maintain the gas in its thermodynamic equilibrium. Hence, it seems that the adiabatic equation of state is not a good option for the collisionless plasma. But microscopic wave-particle interactions can be a good substitution for collisions in the gas because they can maintain the local thermodynamic equilibrium [20]. Therefore, the adiabatic equation of state is when the change in temperature is related to the change in density. In this case pressure is defined by adiabatic law,

$$PV^\gamma = \text{constant}, \quad (1.9)$$

here  $\gamma$ , is the adiabatic index, which is the ratio of the heat capacity at constant pressure to the heat capacity at constant volume.

**-Non-adiabatic equation of state:** The simplest non-adiabatic equation of state is the isothermal case, where  $T_s$  is constant ( $\gamma = 1$ ). In contrast to the adiabatic process in which there are no exchanges of heat with the surroundings, in the isothermal cases the temporal variations occur slowly enough for plasma to remain in equilibrium with a surrounding reservoir through heat exchange.

Another non-adiabatic equation of state is, the isobaric and isometric pressure.

**-Isotropic pressure:** The pressure is isotropic when the pressure tensor is diagonal with equal diagonal elements, i.e.,

$$\overleftrightarrow{\mathbf{P}}_s = \overleftrightarrow{\mathbf{1}} p_s, \quad (1.10)$$

where,  $\overleftrightarrow{\mathbf{1}}$  is the unit tensor and  $p_s$  is defined as an ideal gas Eq. (1.8). In matrix notation the pressure tensor of an isotropic gas follows as,

$$\overleftrightarrow{\mathbf{P}}_s = \begin{pmatrix} p_s & 0 & 0 \\ 0 & p_s & 0 \\ 0 & 0 & p_s \end{pmatrix}. \quad (1.11)$$

**-Anisotropic pressure:** In magnetized plasma, sometimes particles are unable to transfer their momentums effectively between the parallel and perpendicular directions (due to the magnetic field direction), then the diagonal elements of pressure tensor are not equal. If the magnetic field lies on the  $z$  axis, the pressure tensor can be defined as,

$$\overleftrightarrow{\mathbf{P}}_s = \begin{pmatrix} p_{s\perp} & 0 & 0 \\ 0 & p_{s\perp} & 0 \\ 0 & 0 & p_{s\parallel} \end{pmatrix}. \quad (1.12)$$

Where,  $p_{s\perp} = n_s k T_{s\perp}$  and  $p_{s\parallel} = n_s k T_{s\parallel}$ .

**-Cold plasma:** In this approximation, the temperature is very low such that the pressure can be neglected  $\overleftrightarrow{\mathbf{P}}_s = 0$ . The Earth's ionosphere is often approximated as a cold plasma [66].

## Two-Fluid models

In fluid theory the evolution of macroscopic moments of the particles is considered. In two-fluid plasmas, moments are derived for electrons and ions separately,  $s = e, i$ . In some cases there are two ion fluids used to describe the plasma. In related to the lunar wake, an analytic model is developed based on a two-fluid description to consider counterstreaming ion flow parallel to the magnetic field lines into the lunar wake from above and below the wake boundaries [18]. This formalism can be used to calculate the two counterstreaming ion fluxes into the wake that are not easily predicted with other models. This model is described in Ch. 2. One of the interesting computational techniques in fluid theory is called the finite element method. In this technique, an arbitrary geometry is divided into a large number of cells. The unknown functions are discretized and solved on the mesh. In Ch. 3, a 2D finite element code is used to simulate the lunar wake.

## Single-fluid models (MHD)

Macroscopic, or fluid equations governing the evolution of a plasma, can be written in different forms, at different levels of detail. Some formulations are obtained by taking successive moments of kinetic equations for each particle species. This then needs to be closed heuristically by expressing the higher order moment in terms of spatial and/temporal derivatives of lower moments. A simpler approach, used in this thesis, considers the equations of evolution for a single fluid. These equations are obtained by combining the conservation equations for mass, momentum, and energy for all species, into corresponding equations for a single fluid. In addition to conservation equations, single-fluid models also include a generalized Ohm's law obtained from the electron momentum equation, whenever currents and perturbed magnetic fields are involved. In the following, simplified single-fluid equations are used to model the wake downstream of the Moon, when it is exposed to the solar wind. For example, Harnett and Winglee [26] applied a 2.5D MHD model to simulate the solar wind interplay with localized magnetic fields at the surface of the Moon. They found structures similar to Earth's magnetopause and bow shock near magnetic field anomalies, with positions and shapes varying with solar wind conditions. ARTEMIS data supports the outward expansion of the lunar wake in the near-Moon region at magnetosonic velocities as is predicted with MHD models [78]. More recently Xie et al. [77] used the Space Weather Modeling Framework (SWMF) [69] to study asymmetries in the lunar wake associated with different orientations of the solar wind magnetic field and plasma flow velocity.

The set of single-fluid MHD variables are defined as,

1. The mass density:

$$\rho = (m_e n_e + m_i n_i), \quad (1.13)$$

2. The fluid velocity:

$$\mathbf{V} = \frac{(m_i n_i \mathbf{V}_i + m_e n_e \mathbf{V}_e)}{m_i n_i + m_e n_e}, \quad (1.14)$$

3. The charge density:

$$q = e(n_i - n_e), \quad (1.15)$$

4. The current density:

$$\mathbf{J} = e(n_i\mathbf{V}_i - n_e\mathbf{V}_e), \quad (1.16)$$

5. The pressure:

$$p = p_i + p_e, \quad (1.17)$$

here subscript  $i$  and  $e$  refer to ions and electrons respectively. By applying these variables and considering the plasma as quasi-neutral the single-fluid continuity and momentum equations can be written,

$$\frac{\partial \rho}{\partial t} + \nabla \cdot (\rho \mathbf{V}) = 0, \quad (1.18)$$

$$\frac{\partial \rho \mathbf{V}}{\partial t} + \nabla \cdot (\rho \mathbf{V} \mathbf{V}) = -\nabla p + \mathbf{J} \times \mathbf{B}, \quad (1.19)$$

where  $\mathbf{B}$  is the magnetic field. The adiabatic law is also taken into account,

$$\frac{d}{dt} \left( \frac{p}{\rho^\gamma} \right) = 0. \quad (1.20)$$

To close the set of equations, Maxwell equations are applied,

$$\nabla \times \mathbf{E} = -\frac{\partial \mathbf{B}}{\partial t}, \quad (1.21)$$

$$\nabla \times \mathbf{B} = \mu_0 \mathbf{J} + \epsilon_0 \mu_0 \frac{\partial \mathbf{E}}{\partial t}, \quad (1.22)$$

here  $\mathbf{E}$  is the electric field,  $\mu_0$  and  $\epsilon_0$  are magnetic permeability of free space and permeability of free space. Equations 1.21 and 1.22 are known as Farady's and Ampere's equations respectively. The ideal MHD equation is written by assuming the plasma is highly conductive,

$$\mathbf{E} = -\mathbf{V} \times \mathbf{B}. \quad (1.23)$$

In MHD approximation, a plasma can support three different types of normal modes; the fast mode, the slow mode and the shear Alfvén mode [4], [67].

### 1.6.4 Test-particle simulations

The test-particle method uses the approximated electromagnetic fields obtained from fluid or kinetic models, to compute particle trajectories without

solving a set of kinetic equations. The accuracy of the distribution functions obtained with this method depends on the accuracy of the fields used to compute particle trajectories. These estimated distributions can nonetheless be informative, and are useful to check for consistency in fluid simulation results. In Ch. 4 a test-particle code is used to trace ions flowing into the lunar wake and distribution functions are calculated. By taking moments of the distribution functions, some of the macroscopic quantities are obtained. The assumptions made in the fluid models are checked with these calculated moments, and found to be in reasonable agreement.

### 1.6.5 Observations

The planning of future lunar missions necessitates a good understanding of the space environment conditions near and at the Moon surface. Several missions have already been sent to study this environment and the interaction between the solar wind and the Moon, including examining the structure of the wake (see Tables 1.3 and 1.4). The first observations of the lunar wake were made by Explorer 35 and the Apollo missions [39]. Missions such as, WIND (1994), Lunar Reconnaissance Orbiter (LRO) (2009) and, Lunar Atmosphere and Dust Environment Explorer (LADEE) (2013) were sent to orbit the Moon, in order to collect data on its interaction with the solar wind [22]. The Acceleration, Reconnection, Turbulence and Electrodynamics of the Moon's Interaction with the Sun (ARTEMIS) satellites are the latest lunar mission deployed in 2010 by sending the two of five in-orbit spacecraft from the project "Time History of Events and Macroscale Interactions during Substorms" (THEMIS) to orbit the Moon [1]. On February 2010 the P1 spacecraft of the ARTEMIS (formerly THEMIS-B) for the first time went through the lunar wake at a distance of  $\sim 3.5R_m$  from the Moon center downstream while the Moon was outside of the magnetosphere [68], [75]. ARTEMIS observations show that the diamagnetic fields in the lunar wake can exceed twice the ambient magnetic field during high plasma beta conditions [62]. Two different observations of interplanetary magnetic field orientations from ARTEMIS in

the lunar wake are also presented in order to compare with the density calculated with all these 2D models and which is presented in Ch. 5.

More specifically, goals of this thesis are:

1. To assess the applicability of four relatively simple and computationally fast models, to reproduce some of the main features of the lunar wake. This is done by making cross-comparisons between the different models, and by comparing model predictions with ARTEMIS observations.
2. To check the validity of the approximations made in the construction of the fluid models, using test-particle simulations.

# Chapter 2

## The method of characteristics

### 2.1 Introduction

Plasma expansion into a vacuum is an important topic in space plasma research because it applies to solar wind phenomena, such as plasma interactions with planets and their natural satellites and interplay of the solar wind with artificial obstacles orbiting the Earth and other planets. The first paper on this physical process introduced a simple one-dimensional model and showed that ions in a collisionless plasma are accelerated up to thermal velocities of electrons to fill the void [19]. Depending on density, temperature, and velocity, plasma expansion can cause a variety of physical phenomena, as for example, ion acceleration into the vacuum, rarefaction wave, and plasma instabilities [64]. As the supersonic solar wind flows through the solar system, it interacts with the planets and their moons. In Earth environment, the Moon surface can absorb the plasma in the day-side, and a wake characterized by strong density depletion is formed on the night-side. Electrons with their higher thermal speed are partly filling the wake ahead of ions. Ions are then accelerated into the wake by the resulting Ambipolar electric field. Theoretical models of plasma expansion into the wake predict that the plasma density decreases exponentially from its edge towards its middle of the wake as confirmed in the WIND spacecraft crossing the lunar wake at a distance of 6.5 lunar radii ( $R_m$ ) on December 1994 [56]. Self-similar solutions have been constructed to describe electron density, temperature and magnetic field perturbations in the lunar wake for plasma expansion into the wake, considering a non-Maxwellian

distribution function [21]. However, such one-dimensional models cannot explain the velocity of ions parallel to the magnetic field filling the lunar wake because they do not consider the spherical shape of the Moon [19], [21], [56], [64]. Following initial one-dimensional models, Hutchinson applied an analytic self-consistent electrostatic expansion model of the near-Moon wake to predict the proper velocity of ions which was observed with the Chandrayaan-1 spacecraft [30], [31], [33]. In this chapter, I describe a 2D fluid model in the plane of magnetic field  $\mathbf{B}$  and the solar wind velocity  $\mathbf{V}_{SW}$  to demonstrate the expansion of counterstreaming ion fluids parallel to  $\mathbf{B}$  into the lunar wake from both sides. This model is an extension to the two-dimensional single-fluid approach proposed by Hutchinson to describe the edge of the lunar wake [30], [31], [33]. The equations governing the dynamics of the flowing ions are derived under certain assumptions. They are analyzed with the method of characteristics.

## 2.2 Approximate analytic models to study the lunar wake

### 2.2.1 Single-fluid model of the lunar wake (Hutchinson's model)

The basic assumptions Hutchinson made to develop a single-fluid model to study only one edge of the lunar wake, are listed as,

1. Particle gyro-radii are much smaller than any macroscopic scale length in the problem,
2. Plasma is quasi-neutral,
3. Ions can be described as single isothermal fluids,
4. The solar wind magnetic field is constant and uniform,
5. The ion polarization drift is negligible,
6. The plasma equation of state is that of an ideal gas,
7. Electrons are described as a massless isothermal fluid.

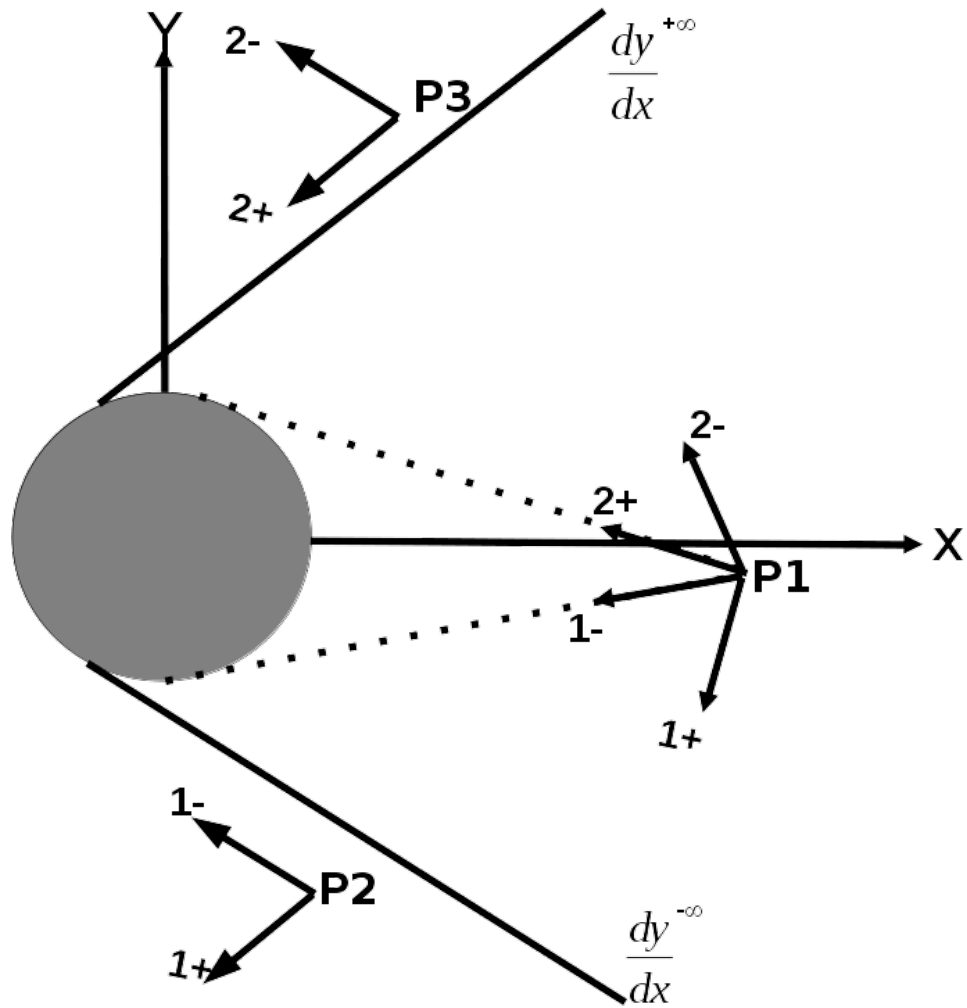


Figure 2.1: Illustration of the unperturbed solar wind and lunar wake regions. Points P2 and P3 are located, respectively, below and above the wake in the unperturbed region of the solar wind, while P1 is in the wake. Vectors identified with + and - are pointing in the  $-X$  direction along the positive and negative characteristics, respectively. The labels 1 and 2 on these vectors refer to plasma below and above the wake in the unperturbed plasma, or entering the wake from below and above the wake boundaries, respectively. The two lines labeled  $\frac{dy}{dx}|^{\pm\infty}$  show the boundary between the unperturbed solar wind and the wake. Their slope is that of the + and - upstream characteristic, and they are tangent to the Moon above and below the lunar disk respectively.

The dynamics of the ions as a fluid are studied by solving the steady-state continuity and momentum equations.

$$\frac{\partial n}{\partial t} + \nabla \cdot (n\mathbf{V}) = 0, \quad (2.1)$$

$$\frac{\partial(n\mathbf{V})}{\partial t} + \nabla \cdot (n\mathbf{V}\mathbf{V}) = \frac{-nZe}{m} \nabla \phi - \frac{1}{m} \nabla p_i + \frac{nZe}{m} (\mathbf{V} \times \mathbf{B}), \quad (2.2)$$

in these expressions,  $m$ ,  $n$ ,  $p_i$ ,  $\mathbf{V}$ ,  $Z$ ,  $\phi$  and  $e$  are, respectively, ion mass, number density, pressure, velocity, ion charge-number, electric potential, and electron charge. The subscript  $i$  refers to ions. Under the assumption of steady-state the momentum equation 2.2 is written in terms of the components parallel ( $\parallel$ ) and perpendicular ( $\perp$ ) to the magnetic field  $\mathbf{B}$ . The cross-product of the perpendicular momentum with  $\mathbf{B}$  gives

$$\mathbf{V}_\perp = - \left[ \frac{m}{Ze} (\mathbf{V} \cdot \nabla \mathbf{V}_\perp) \times \frac{\mathbf{B}}{B^2} + \frac{1}{nZe} \nabla_\perp p_i \times \frac{\mathbf{B}}{B^2} + \nabla_\perp \phi \times \frac{\mathbf{B}}{B^2} \right]. \quad (2.3)$$

The first term in this equation is the polarization drift which is ignorable, which results in the "drift-approximation". This approximation is justified because the ion gyroradius (in the background magnetic field  $\mathbf{B}_{IMF}$ ) is much smaller than any perpendicular length-scale. The last two terms of Eq. 2.3 are known as the diamagnetic and the  $\mathbf{E} \times \mathbf{B}$  drifts. The diamagnetic drift is perpendicular to the magnetic field  $\mathbf{B}$ . The assumption of constant magnetic field leads to eliminate the grad-B and curvature drifts. A more complete description on particle drifts in a plasma can be found, for example, in [2], [20], [55]. With the ideal gas ( $p_i = nT_i$ ) and isothermal ion flow ( $T_i$  is a constant) approximations, Eq. 2.3 reads,

$$\mathbf{V}_\perp = - \left[ \frac{T_i}{Ze} \nabla_\perp \ln(n) \times \frac{\mathbf{B}}{B^2} + \nabla_\perp \phi \times \frac{\mathbf{B}}{B^2} \right]. \quad (2.4)$$

The continuity equation becomes,

$$\nabla n \cdot \mathbf{V} + n(\nabla \cdot \mathbf{V}) = 0, \quad (2.5)$$

$$\mathbf{V} \cdot \nabla n + n [\nabla \cdot (\mathbf{V}_\parallel + \mathbf{V}_\perp)] = 0. \quad (2.6)$$

Substituting Eq. 2.4 in Eq. 2.6 we find,

$$\mathbf{V} \cdot \nabla n + n \left[ \nabla \cdot \left( \mathbf{V}_\parallel + - \left[ \frac{T_i}{Ze} \nabla_\perp \ln(n) \times \frac{\mathbf{B}}{B^2} + \nabla_\perp \phi \times \frac{\mathbf{B}}{B^2} \right] \right) \right] = 0. \quad (2.7)$$

Making use of the fact that curl of a gradient is zero and  $\mathbf{B}$  is constant, the third and fourth terms in the Eq. 2.7 are zero, and Eq. 2.7 reduces to

$$\mathbf{V} \cdot \nabla n + n \nabla_{\parallel} \mathbf{V}_{\parallel} = 0. \quad (2.8)$$

Finally, the continuity equation becomes,

$$\mathbf{V} \cdot \nabla \ln(n) + \nabla_{\parallel} \mathbf{V}_{\parallel} = 0. \quad (2.9)$$

The steady-state parallel momentum Eq. 2.2 is written as,

$$\mathbf{V} \cdot \nabla \mathbf{V}_{\parallel} = -\left[\frac{T_i}{m} \nabla_{\parallel} \ln(n) + \frac{Ze}{m} \nabla_{\parallel} \phi\right]. \quad (2.10)$$

Assuming the massless electron fluid gives a relation between the electric field and pressure gradient. Using the parallel electron momentum equation and assuming that plasma is quasi-neutral because the Debye length is much smaller than any length scale in the problem ( $n_e = Zn$ ), one finds the familiar adiabatic relation between the electric potential and parallel pressure gradients,

$$\mathbf{E}_{\parallel} = -\nabla_{\parallel} \phi = -\frac{1}{eZn} \nabla_{\parallel} p_e = -\frac{T_e}{Ze} \nabla_{\parallel} \ln(n). \quad (2.11)$$

It can then be shown that Eq. 2.9, Eq. 2.10, and Eq. 2.11 reduce to the following two coupled normalized equations for the ion density  $n$  and Mach number  $M$ :

$$\mathbf{M} \cdot \nabla \ln(n) + \nabla_{\parallel} M_{\parallel} = 0, \quad (2.12)$$

and

$$\mathbf{M} \cdot \nabla M_{\parallel} + \nabla_{\parallel} \ln(n) = 0. \quad (2.13)$$

Where, the velocity is normalized to the ion acoustic speed of the plasma fluid  $c_s = \sqrt{\frac{(ZT_e + \gamma T_i)}{m}}$  to gives the Mach number  $\mathbf{M} = \mathbf{V}/c_s$ . By adding and subtracting these equations, it follows that

$$(\mathbf{M} \cdot \nabla + \nabla_{\parallel})(\ln(n) + M_{\parallel}) = 0, \quad (2.14)$$

and

$$(\mathbf{M} \cdot \nabla - \nabla_{\parallel})(\ln(n) - M_{\parallel}) = 0, \quad (2.15)$$

are two decoupled equations for the two independent variables  $\ln(n) \pm M_{\parallel}$  that can be solved straightforwardly using the method of characteristics. Equations 2.14 and 2.15 describe the dynamics of ions in the lunar wake as a single-fluid to model only one edge of the lunar wake (Hutchinson model [31]). In particular, it follows from Eq. 2.14 and 2.15 that  $\ln(n) \pm M_{\parallel}$  are constant, respectively, along the characteristics defined by the equations

$$\left. \frac{dx}{ds} \right|^{\pm} = M_x \pm \frac{B_x}{B} \quad (2.16)$$

and

$$\left. \frac{dy}{ds} \right|^{\pm} = M_y \pm \frac{B_y}{B}. \quad (2.17)$$

Where  $ds$  is the infinitesimal element of length along the characteristics, and the  $\pm$  superscripts refer to positive and negative characteristics, respectively. In the upstream solar wind  $\pm$  characteristics are straight lines with slopes obtained by taking the ratio of right-hand-sides of Eq. 2.17 to Eq. 2.16. Using this formalism, Hutchinson [33] was able to model the edge of the lunar wake. Referring to Fig. 2.1, and assuming that plasma entering the wake is coming predominantly from one side of the Moon, say from below, he argued that in the wake the parallel Mach number must be such that the negative characteristic is tangent to the Moon from below. Therefore, the following equation for the plasma density associated with the parallel flow coming from below becomes:

$$n = n_0 \exp(-|M_{\parallel} - M_{0\parallel}|), \quad (2.18)$$

where  $M_{0\parallel}$  and  $n_0$  are the upstream plasma parallel velocity and upstream number density.

## 2.2.2 Two-fluid non-interacting model of the lunar wake (the analytic model)

I now apply Hutchinson's approach to the full width of the wake by considering the plasma flow entering the wake from both below and above the 2D wake region, as shown in Fig. 2.1. Compared with Hutchinson's original analysis in which only one ion fluid was considered near the edge of the wake, I need to account for two ion fluids coming from either side of the Moon in this 2D model. As we shall see later when the solutions obtained are compared with the finite element model, these counterstreaming ion flows are essential in determining the properties of the wake region plasma. We account for the two ion fluids by labeling them with subscripts 1 and 2 (Fig. 2.1), corresponding to plasma entering from below and above, respectively, as discussed by [32]. Each ion fluid is characterized by a density  $n_{1,2}$  and a parallel Mach number  $M_{1,2\parallel}$ , and it is governed by two characteristic equations similar to Eqs. 2.14 and 2.15. The main difference here comes from the relation between the parallel electric field and the electron pressure gradient. Making use of the quasi-neutrality assumption, and accounting for the two ion fluids, Eq. 2.11 now reads

$$\nabla_{\parallel}\phi = \frac{T_e}{e} \left( \frac{n_1}{n_1 + n_2} \nabla_{\parallel} \ln(n_1) + \frac{n_2}{n_1 + n_2} \nabla_{\parallel} \ln(n_2) \right). \quad (2.19)$$

Then, following the same steps as outlined above for Hutchinson's model, one finds

$$\begin{aligned} & (\mathbf{M}_1 \cdot \nabla + \nabla_{\parallel})(\ln(n_1) + M_{1\parallel}) \\ &= \frac{ZT_e}{T_i + ZT_e} \frac{n_2}{n_1 + n_2} \nabla_{\parallel} (\ln(n_1) - \ln(n_2)), \end{aligned} \quad (2.20)$$

$$\begin{aligned} & (\mathbf{M}_1 \cdot \nabla - \nabla_{\parallel})(\ln(n_1) - M_{1\parallel}) \\ &= -\frac{ZT_e}{T_i + ZT_e} \frac{n_2}{n_1 + n_2} \nabla_{\parallel} (\ln(n_1) - \ln(n_2)), \end{aligned} \quad (2.21)$$

$$\begin{aligned} & (\mathbf{M}_2 \cdot \nabla + \nabla_{\parallel})(\ln(n_2) + M_{2\parallel}) \\ &= -\frac{ZT_e}{T_i + ZT_e} \frac{n_1}{n_1 + n_2} \nabla_{\parallel} (\ln(n_1) - \ln(n_2)), \end{aligned} \quad (2.22)$$

and,

$$\begin{aligned} & (\mathbf{M}_2 \cdot \nabla - \nabla_{\parallel})(\ln(n_2) - M_{2\parallel}) \\ &= \frac{ZT_e}{T_i + ZT_e} \frac{n_1}{n_1 + n_2} \nabla_{\parallel} (\ln(n_1) - \ln(n_2)). \end{aligned} \quad (2.23)$$

This system of four coupled inhomogeneous equations is more challenging to solve in general than the two equations derived by Hutchinson for a single-fluid. The reason is that owing to the non-zero right-hand-sides, the dependent variables are not precisely constant along the characteristics. Consequently, in contrast to the single-fluid case, the characteristics are not precisely straight lines. The solutions can be obtained iteratively using the method of characteristics which is discussed in the next section, or by discretization of Eqs. 2.20 to 2.23 using finite differences and specifying appropriate boundary conditions.

In the following, Eqs. 2.20 to 2.23 are solved approximately by neglecting the right-hand sides. This means that the two ion fluids streaming from above and below the wake do not interact with one another. In this case, the system of four homogeneous equations reduces to a set of two uncoupled homogeneous equations that can be solved as in Hutchinson's initial analysis. The resulting densities  $n_1$  entering from below, and  $n_2$ , entering from above are then added to give the total plasma wake density.

The approximations made in the analytic model, are further validated by the good agreement with results obtained using other models (which does not make these approximations) and with observations in chapters 3 and 5 respectively. In order to explain the solution procedure, it is useful to write explicit expressions for the characteristics. Assuming an angle  $\alpha$  between the magnetic field and the solar wind flow velocity (see Fig. 2.2), the magnetic field, the Mach number vector, and the parallel gradient are written as,

$$\mathbf{B} = B(\cos(\alpha)\hat{x} + \sin(\alpha)\hat{y}), \quad (2.24)$$

$$\begin{aligned} \mathbf{M} &= [M_{\perp} \sin(\alpha) + M_{\parallel} \cos(\alpha)]\hat{x} \\ &+ [-M_{\perp} \cos(\alpha) + M_{\parallel} \sin(\alpha)]\hat{y}, \end{aligned} \quad (2.25)$$

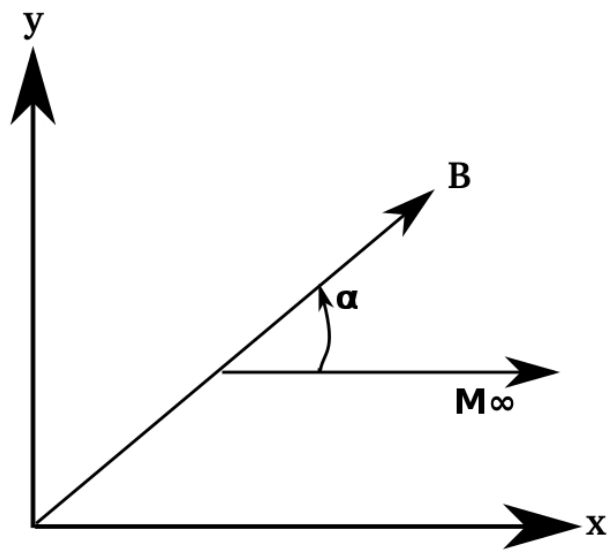


Figure 2.2: The angle between the magnetic field ( $B$ ) and the solar wind flow velocity ( $M_\infty$ ).

and,

$$\nabla_{\parallel} = (\cos(\alpha)\partial/\partial x)\hat{x} + (\sin(\alpha)\partial/\partial y)\hat{y}, \quad (2.26)$$

where, consistent with Hutchinson's model,  $M_{\perp}$  is assumed to be constant. Omitting subscripts 1 and 2 for brevity, the homogeneous approximation of Eqs. 2.20 to 2.23 then become

$$\begin{aligned} & [(M_{\perp} \sin(\alpha) + M_{\parallel} \cos(\alpha) + \cos(\alpha)) \frac{\partial}{\partial x} \\ & + (-M_{\perp} \cos(\alpha) + M_{\parallel} \sin(\alpha) + \sin(\alpha)) \frac{\partial}{\partial y}] [\ln(n) + M_{\parallel}] = 0, \end{aligned} \quad (2.27)$$

$$\begin{aligned} & [(M_{\perp} \sin(\alpha) + M_{\parallel} \cos(\alpha) - \cos(\alpha)) \frac{\partial}{\partial x} \\ & + (-M_{\perp} \cos(\alpha) + M_{\parallel} \sin(\alpha) - \sin(\alpha)) \frac{\partial}{\partial y}] [\ln(n) - M_{\parallel}] = 0. \end{aligned} \quad (2.28)$$

The equations for the two characteristics are then,

$$\left. \frac{dy}{dx} \right|^{\pm} = \frac{\pm \sin(\alpha) - M_{\perp} \cos(\alpha) + M_{\parallel} \sin(\alpha)}{\pm \cos(\alpha) + M_{\perp} \sin(\alpha) + M_{\parallel} \cos(\alpha)}. \quad (2.29)$$

In the upstream region ( $x \rightarrow -\infty$ ) where plasma is unperturbed, the Mach vector  $\mathbf{M}_0$  is purely along  $X$ , which leads to,

$$M_{0\perp} = M_0 \sin(\alpha), \quad (2.30)$$

$$M_{0\parallel} = M_0 \cos(\alpha). \quad (2.31)$$

From this and Eqs. 2.29 it follows that the equations for the upstream characteristics are

$$\left. \frac{dy}{dx} \right|_0^{\pm} = \frac{\pm \sin(\alpha)}{\pm \cos(\alpha) + M_0}. \quad (2.32)$$

### 2.2.3 Results of the analytic analysis ( $\alpha = 90^\circ$ )

In the following, I limit my attention to the particular case where the magnetic field is perpendicular to the upstream flow velocity; that is to  $\alpha = 90^\circ$ . From Eq. 2.32, it follows that the  $\pm$  characteristics are then straight lines with slopes  $\pm 1/M_0$ .

The equations for the upstream characteristics can be used to distinguish between the unperturbed solar wind and the wake regions. By assumption, the

upstream solar wind is unperturbed as  $x \rightarrow -\infty$ . Owing to the constancy of  $\ln(n) \pm M_{\parallel}$  along the  $\pm$  characteristics, it follows that the incoming solar wind at any point  $P$  in Fig. 2.1, will be unaffected; that is,  $n = n_0$  and  $M_{\parallel} = M_0$  if and only if  $P$  can be moved continuously toward  $x \rightarrow -\infty$  in such a way that none of the unperturbed characteristics given in Eqs. 2.32 intersect the Moon. Conversely, the wake is the region where points cannot be moved continuously toward  $x \rightarrow -\infty$  without at least one of the unperturbed characteristics intersecting the Moon. From this, it follows that the positive and negative characteristics tangent delimits the wake region, respectively, above and below the disk of the Moon, as illustrated in Fig. 2.1. The question then is how does one compute densities  $n_1$  and  $n_2$  in the wake region? This is done with a straightforward extension of Hutchinson's approach for the edge of the wake, in which a single ion density is considered. Recalling that  $n_1$  and  $n_2$  are the ion densities entering the wake, respectively, from below and above, and referring to Figure 2.1, these densities are obtained from the equation

$$n_{1,2} = n_0 \exp(-|M_{1,2\parallel} - M_0|). \quad (2.33)$$

$M_{1\parallel}$  is set in order for the negative characteristic to be tangent below the lunar disk for  $n_1$ , and similarly,  $M_{2\parallel}$  is set in order for the positive characteristic to be tangent above for  $n_2$ . Figure 2.3 shows the ion density computed with the analytic model. In this figure,  $\alpha = 90^\circ$  and the perpendicular Mach number is assumed to be  $M_{\perp} = 6.0$ .

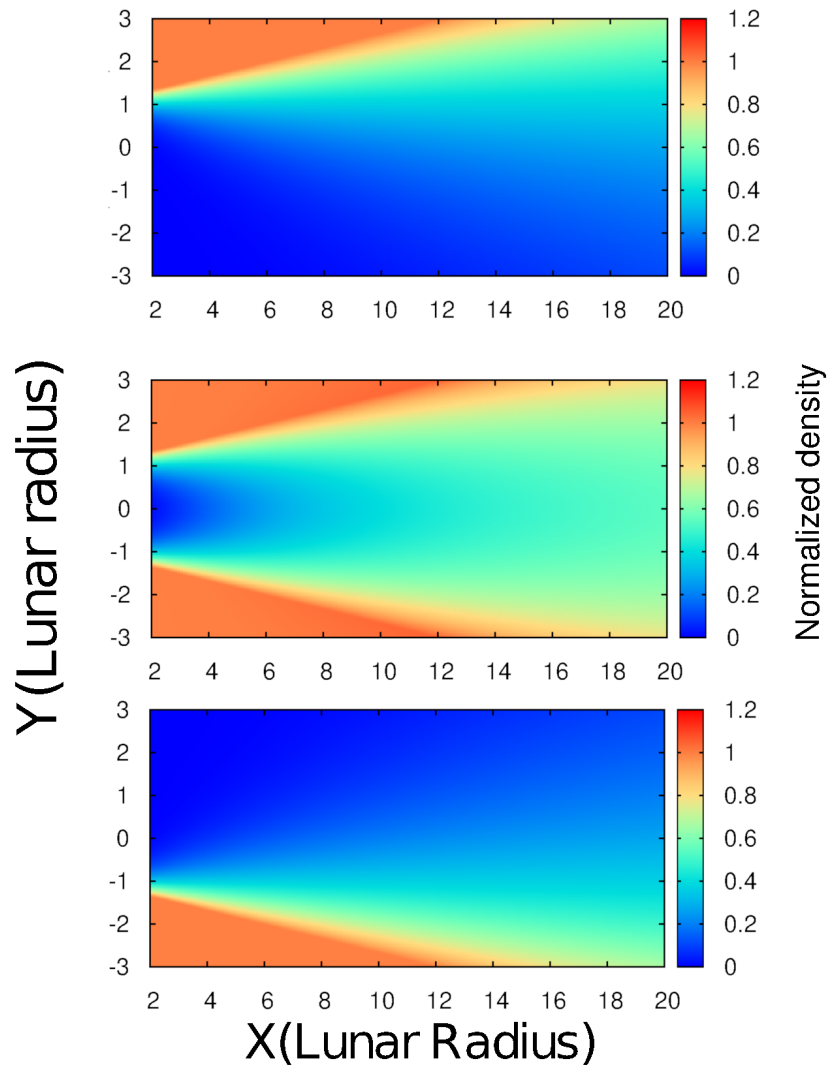


Figure 2.3: Normalized plasma density in the analytic model. The upper and lower panels show the density of ions entering the wake from above and below the wake, respectively. The middle panel shows the total ion density.

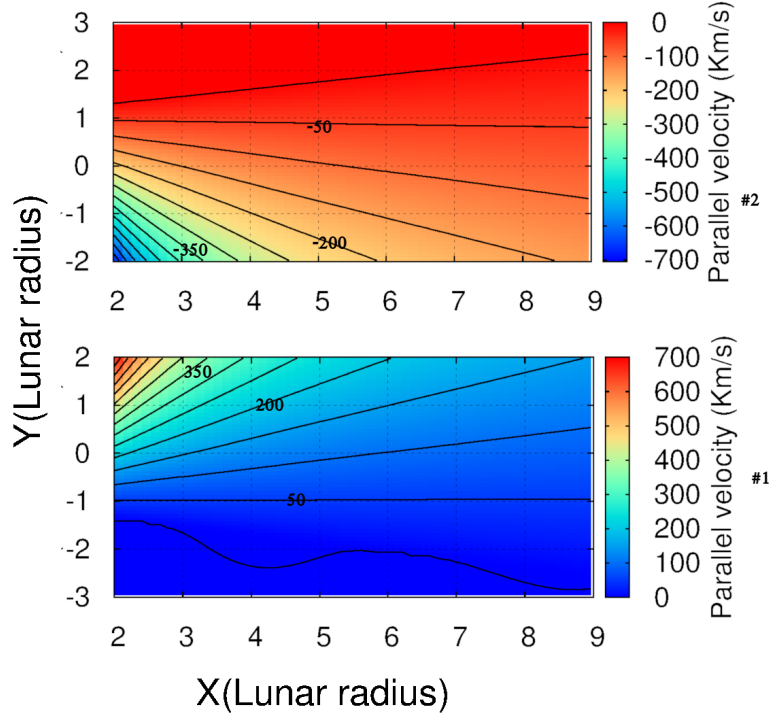


Figure 2.4: Parallel velocity of ions in the analytic model. The upper and lower panels show the parallel normalized velocity of ions entering the wake from above and below the wake, respectively.

### Parallel plasma flow

In addition to the density, the analytic model provides the parallel flow velocity of ions entering the wake. Because the magnetic field is perpendicular to the upstream flow velocity ( $\alpha = 90^\circ$ ), fluids are entering the wake in the opposite direction along the magnetic field  $M_{1\parallel} = -M_{2\parallel}$  as illustrated in Fig. 2.4.  $M_{1\parallel}$  in the solar wind ( $X = 2 R_m$  and  $Y = -3 R_m$ ) is zero and it gets larger as it penetrates the wake, thus leading to a lower density Eq. 2.33.  $M_{2\parallel}$  has a zero value in the solar wind ( $X = 2 R_m$  and  $Y = 3 R_m$ ) where the normalized density is  $n_2 = 1$ . However, as fluid 2 penetrates the wake from above, the parallel velocity gets more negative leading to a decrease in  $n_2$ . Velocities parallel to the magnetic field have a very high absolute value when they exit the wake, but minimal numbers of ions can get to that points. A result of the analytic model, which is not obtained from single-fluid numerical simulation models, is an explicit expression for the parallel flow velocity of

ions entering the wake from below and above. The pressure gradient at the lower edge of the wake drives parallel plasma flow upward and similarly, the pressure gradient at the upper edge drives parallel flow downward into the wake. This is illustrated in Fig. 2.5, which shows the normalized parallel ion flux  $\Gamma_{1,2 \parallel} = (n_{1,2} M_{1,2 \parallel})/n_{\text{sw}0}$ , where  $n_{\text{sw}0}$  is the upstream solar wind density and the net normalized flux  $\Gamma = \Gamma_{1 \parallel} + \Gamma_{2 \parallel}$ .

The middle panel shows the net flux which would be obtained from a fluid simulation: negative and positive parallel flow, above and below the  $X$  axis, corresponds to plasma entering the wake from above and below respectively. The net ion parallel flow at the center of the wake (at  $Y = 0$ ) vanishes by symmetry, but the fact that it is associated with two counterstreaming flows would be missing in single-fluid models. The middle panel shows positive flux in the solar wind above the wake boundary and negative flux below the wake boundary which means that some ions coming from below can reach and go beyond the upper wake boundary. Similarly, a fraction of ions can reach and go beyond the lower boundary of the wake. This may occur in part because, in this analysis, the two ion fluids are independent, so the interaction between the two fluids is neglected. In the next section, I will solve the set of equations by considering the interactions between the two ion fluids to better understand their mutual interaction.

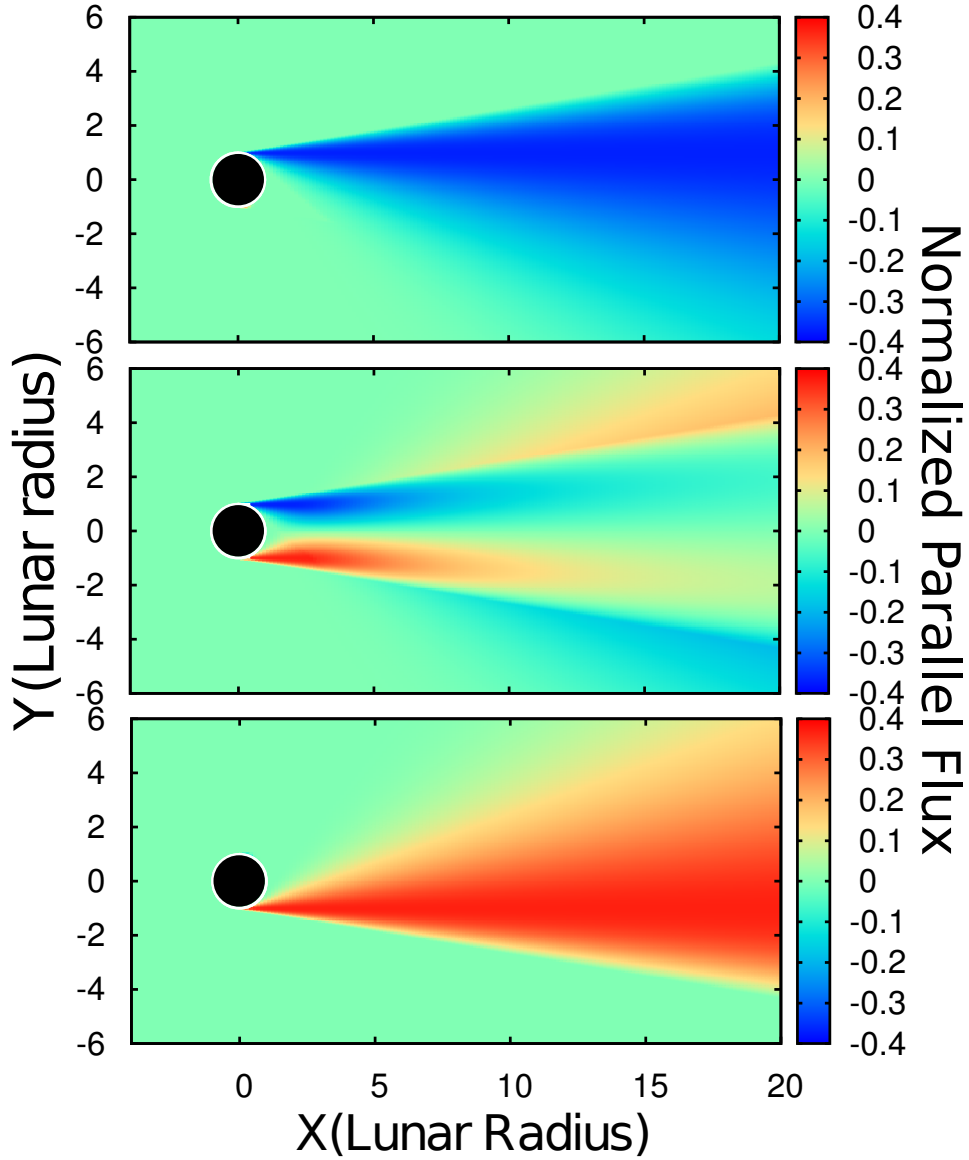


Figure 2.5: Normalized plasma parallel flux along the magnetic field in the analytic model. Plasma entering the wake from directions above and below the wake is shown in the upper and lower panels, respectively. The total normalized parallel flux is shown in the middle panel.

## 2.3 Two-fluid interacting model of the lunar wake (the method of characteristics)

In this section, I describe a method to solve a system of four-coupled, first-order, and non-linear equations given in Eqs. (2.20) to (2.23), while accounting for coupling in right hand sides (RHS). By doing so, the interactions between the two ion fluids counterstreaming into the lunar wake are taken into account. In this case, the characteristics are not exactly straight lines as they were for the single-fluid model. This system of equations is solved by using a technique described by Chester [8]. The most general first-order linear homogeneous system for  $n$  equations and  $n$  unknown functions of two independent variables  $(x, y)$  can be written as

$$\sum_{k=1}^n [a_{jk}(x, y)u_x^{(k)} + b_{jk}(x, y)u_y^{(k)}] = \sum_{k=1}^n [c_{jk}(x, y)u^{(k)}] \quad j = 1, 2, \dots, n, \quad (2.34)$$

where,  $u^1(x, y), u^2(x, y), u^3(x, y), \dots, u^n(x, y)$  are unknown functions and the subscripts show partial derivatives. In this equation, the superscript  $k$  refers to the unknown function and the subscript  $j$  refers to an equation. In Eqs. (2.20) to (2.23), the unknown functions,  $u^k(x, y)$ , appear only in derivative forms so the right hand side of Eq. (2.34) is set to zero in the discussion which follows. As a result, Eq. (2.34) reduces to

$$\sum_{k=1}^n [a_{jk}(x, y)u_x^{(k)} + b_{jk}(x, y)u_y^{(k)}] = 0 \quad j = 1, 2, \dots, n. \quad (2.35)$$

In order to describe the method used to solve this system of equations, first I should consider that the Eq. (2.35) is presented as the directional derivatives

$$\sum_{k=1}^n D_{jk}u^{(k)} = 0 \quad j = 1, 2, \dots, n, \quad (2.36)$$

where the  $n^2$  directional derivatives appear as  $D_{jk} = a_{jk}\frac{\partial}{\partial x} + b_{jk}\frac{\partial}{\partial y}$ . All the  $u^k$  in a single equation,  $j$ th equation, should be differentiated in a same direction in order for the method of characteristics to be applicable. However, in the general, in a given equation, different  $u^k$  are differentiated in different

directions. For example, by looking at Eq. (2.36) in the  $j$ th equation the characteristics for  $u^k$  and  $u^{k+1}$  are  $b^{jk}/a^{jk}$  and  $b^{j(k+1)}/a^{j(k+1)}$  respectively, which are not equal in general. I am looking for a way to find a linear combination of all the  $n$  equations such that in each linear combination all the unknown functions are differentiated in a same direction. In order to achieve this, each equation in Eq. (2.35) is multiplied by arbitrary constants,  $\lambda_j$ , and the resulting equations are added in order to form equations for linear combinations of the  $u^k$

$$\sum_{j,k=1}^n [\lambda_j a_{jk}(x, y) u_x^{(k)} + \lambda_j b_{jk}(x, y) u_y^{(k)}] = 0. \quad (2.37)$$

Thus, in the  $j$ th equation,  $u^k$  is differentiated in the direction with the slope given by

$$\frac{\sum_{j=1}^n \lambda_j b_{jk}}{\sum_{j=1}^n \lambda_j a_{jk}}. \quad (2.38)$$

Consequently, the direction of characteristic lines for all unknowns are the same if

$$\begin{aligned} \sum_{j=1}^n \lambda_j a_{jk} &= \mu \sum_{j=1}^n \lambda_j b_{jk} \quad k = 1, \dots, n, \\ \sum_{j=1}^n \lambda_j (a_{jk} - \mu b_{jk}) &= 0 \quad k = 1, \dots, n, \end{aligned} \quad (2.39)$$

where  $\mu$  is a constant. As can be seen, to find the desired PDE which is a linear combination of  $n$  equations in the Eq. (2.35), one must find  $\lambda_j$  and  $\mu$ . By considering the matrix form of the above equations,  $\mu$  is seen to be the root of an  $n$ th degree polynomial equation

$$\det(a_{jk} - \mu b_{jk}) = 0, \quad (2.40)$$

for which,  $\lambda_j$  can form a row vector  $\Lambda = (\lambda_1, \dots, \lambda_n)$  which is a left eigenvector of  $A - \mu B$ . I combined equations (2.37) and (2.39) to get

$$\sum_{k=1}^n [\lambda_j b_{jk} (\mu u_x^{(k)} + u_y^{(k)})] = 0, \quad (2.41)$$

where

$$\sum_{j=1}^n \lambda_j b_{jk} = \beta_k. \quad (2.42)$$

From Eq. (2.41) then it follows that

$$\sum_{k=1}^n \beta_k (\mu u_x^{(k)} + u_y^{(k)}) = 0. \quad (2.43)$$

Equation (2.40) is an  $n$ th-degree polynomial equation for  $\mu$ . Therefore, it has  $n$  real roots  $(\mu_1, \dots, \mu_r, \mu_n)$ . For each of these roots there is an eigenvector  $\Lambda_r = (\lambda_{r1}, \dots, \lambda_{rn})$ . Then the associated eigenvector  $\Lambda_r$  is applied to form the desired PDE. For each root,  $\mu_l$ , the directional derivative is defined as  $D_l = \mu_l \frac{\partial}{\partial x} + \frac{\partial}{\partial y}$ , in the direction with the slope  $\mu_l^{-1}$ . I set

$$\beta_{kl} = \sum_{j=1}^n \lambda_{jl} b_{jk}. \quad (2.44)$$

Then Eq. (2.43) can be written as

$$\sum_{k=1}^n \beta_{kl} D_l u^{(k)} = D_l \sum_{k=1}^n \beta_{kl} u^{(k)} - \sum_{k=1}^n (D_l \beta_{kl}) u^{(k)}. \quad (2.45)$$

If I define

$$\hat{u}^{(l)} = \sum_{k=1}^n \beta_{kl} u^{(k)} \quad \text{and} \quad \hat{C}_l = \sum_{k=1}^n (D_l \beta_{kl}) u^{(k)}. \quad (2.46)$$

Then, the abbreviated form of Eq. (2.41) can be written as

$$D_l \hat{u}^{(l)} = \hat{C}_l \quad l = 1, \dots, n. \quad (2.47)$$

To summarise, the solution of the given system of first-order linear PDEs Eq. (2.35) consists of the following steps:

- Solve for the  $n$  roots of,  $\det(A - \mu B)$ .
- For each root,  $\mu_l$ , determine eigenvector,  $\Lambda_l$ , associated with zero eigenvalue.
- Construct a linear superposition of the system of equation using this eigenvector as in Eq. (2.39).
- The  $n$  linear superposition of the unknown functions,  $\hat{u}^{(l)}$ , in Eq. (2.46) are constructed and by using Eq. (2.47), and all  $\hat{u}^{(l)}$  are advanced by one step.

- After each step, the original unknowns,  $u^k$ , are updated using the known linear relation, Eq. (2.46), between  $\hat{u}^{(l)}$  and functions  $u^k$ .
- Repeat the procedure until all the characteristics cover the entire domain of interest.

Coming back to Eqs. (2.20) to (2.23), there are two independent variables  $x, y$  and four unknowns

$$u^{(1)} = \ln(n_1), \quad u^{(2)} = M_{1\parallel}, \quad u^{(3)} = \ln(n_2), \quad u^{(4)} = M_{2\parallel}. \quad (2.48)$$

As in the previous section, I assume an angle  $\alpha$  is between the magnetic field line and the solar wind flow velocity Fig. 2.2  $M_\infty$ , which lies on the  $X$  axis. Equations (2.20) to (2.23) are built in terms of parallel and perpendicular components to the magnetic field direction but I need to rewrite them in terms of  $x, y$ . I have,

$$\begin{aligned} \hat{x} &= \cos(\alpha)\hat{b} + \sin(\alpha)\hat{n}, \\ \hat{y} &= \sin(\alpha)\hat{b} - \cos(\alpha)\hat{n}, \end{aligned} \quad (2.49)$$

where  $\hat{b}$  and  $\hat{n}$  are unit vectors parallel and perpendicular to the magnetic field line respectively. The parallel and perpendicular Mach numbers in the solar wind are given by

$$\begin{aligned} M_{\parallel sw} &= M_\infty \cos(\alpha), \\ M_{\perp sw} &= M_\infty \sin(\alpha). \end{aligned} \quad (2.50)$$

From Eq. (2.49), the derivatives of parallel and perpendicular in terms of  $x, y$  are

$$\begin{aligned} \hat{b} \cdot \nabla &= \cos(\alpha) \frac{\partial}{\partial x} + \sin(\alpha) \frac{\partial}{\partial y}, \\ \hat{n} \cdot \nabla &= \sin(\alpha) \frac{\partial}{\partial x} - \cos(\alpha) \frac{\partial}{\partial y}. \end{aligned} \quad (2.51)$$

Equations (2.20) to (2.23) from Eqs. (2.49) to (2.51) are written explicitly as

$$\begin{aligned}
& [(M_{1\parallel} + 1 - A_2) \cos(\alpha) + M_\infty \sin(\alpha)] \left( \frac{\partial \ln(n_1)}{\partial x} \right) + [(M_{1\parallel} + 1 - A_2) \sin(\alpha) - M_\infty \cos(\alpha)] \left( \frac{\partial \ln(n_1)}{\partial y} \right) \\
& + [(M_{1\parallel} + 1) \cos(\alpha) + M_\infty \sin(\alpha)] \left( \frac{\partial M_{1\parallel}}{\partial x} \right) + [(M_{1\parallel} + 1) \sin(\alpha) - M_\infty \cos(\alpha)] \left( \frac{\partial M_{1\parallel}}{\partial y} \right) \\
& + [A_2 \cos(\alpha)] \left( \frac{\partial \ln(n_2)}{\partial x} \right) + [A_2 \sin(\alpha)] \left( \frac{\partial \ln(n_2)}{\partial y} \right) \\
& = 0,
\end{aligned} \tag{2.52}$$

$$\begin{aligned}
& [(M_{1\parallel} - 1 + A_2) \cos(\alpha) + M_\infty \sin(\alpha)] \left( \frac{\partial \ln(n_1)}{\partial x} \right) + [(M_{1\parallel} - 1 + A_2) \sin(\alpha) - M_\infty \cos(\alpha)] \left( \frac{\partial \ln(n_1)}{\partial y} \right) \\
& + [(-M_{1\parallel} + 1) \cos(\alpha) - M_\infty \sin(\alpha)] \left( \frac{\partial M_{1\parallel}}{\partial x} \right) + [(-M_{1\parallel} + 1) \sin(\alpha) + M_\infty \cos(\alpha)] \left( \frac{\partial M_{1\parallel}}{\partial y} \right) \\
& + [-A_2 \cos(\alpha)] \left( \frac{\partial \ln(n_2)}{\partial x} \right) + [-A_2 \sin(\alpha)] \left( \frac{\partial \ln(n_2)}{\partial y} \right) \\
& = 0,
\end{aligned} \tag{2.53}$$

$$\begin{aligned}
& [A_1 \cos(\alpha)] \left( \frac{\partial \ln(n_1)}{\partial x} \right) + [A_1 \sin(\alpha)] \left( \frac{\partial \ln(n_1)}{\partial y} \right) + \\
& [(M_{2\parallel} + 1 - A_1) \cos(\alpha) + M_\infty \sin(\alpha)] \left( \frac{\partial \ln(n_2)}{\partial x} \right) + [(M_{2\parallel} + 1 - A_1) \sin(\alpha) - M_\infty \cos(\alpha)] \left( \frac{\partial \ln(n_2)}{\partial y} \right) \\
& + [(M_{2\parallel} + 1) \cos(\alpha) + M_\infty \sin(\alpha)] \left( \frac{\partial M_{2\parallel}}{\partial x} \right) + [(M_{2\parallel} + 1) \sin(\alpha) - M_\infty \cos(\alpha)] \left( \frac{\partial M_{2\parallel}}{\partial y} \right) \\
& = 0,
\end{aligned} \tag{2.54}$$

$$\begin{aligned}
& [-A_1 \cos(\alpha)] \left( \frac{\partial \ln(n_1)}{\partial x} \right) + [-A_1 \sin(\alpha)] \left( \frac{\partial \ln(n_1)}{\partial y} \right) + \\
& [(M_{2\parallel} - 1 + A_1) \cos(\alpha) + M_\infty \sin(\alpha)] \left( \frac{\partial \ln(n_2)}{\partial x} \right) + [(M_{2\parallel} - 1 + A_1) \sin(\alpha) - M_\infty \cos(\alpha)] \left( \frac{\partial \ln(n_2)}{\partial y} \right) \\
& + [(-M_{2\parallel} + 1) \cos(\alpha) - M_\infty \sin(\alpha)] \left( \frac{\partial M_{2\parallel}}{\partial x} \right) + [(-M_{2\parallel} + 1) \sin(\alpha) + M_\infty \cos(\alpha)] \left( \frac{\partial M_{2\parallel}}{\partial y} \right) \\
& = 0,
\end{aligned} \tag{2.55}$$

where  $A_{1,2} = \frac{ZT_e}{T_i + ZT_e} \times \frac{1}{1 + \exp[\ln(n_{2,1}) - \ln(n_{1,2})]}$ .

The coefficients  $a_{jk}$  and  $b_{jk}$  in the Eq. (2.35) can be written as

$$A = \begin{pmatrix} (M_1 + 1 - A_2) \cos(\alpha) + D & (M_1 + 1) \cos(\alpha) + D & 0 & 0 \\ (M_1 - 1 + A_2) \cos(\alpha) + D & (-M_1 + 1) \cos(\alpha) - D & A_2 \cos(\alpha) & 0 \\ A_1 \cos(\alpha) & 0 & -A_2 \cos(\alpha) & 0 \\ -A_1 \cos(\alpha) & 0 & (M_2 + 1 - A_1) \cos(\alpha) + D & (M_2 + 1) \cos(\alpha) + D \\ & & (M_2 - 1 + A_1) \cos(\alpha) + D & (-M_2 + 1) \cos(\alpha) - D \end{pmatrix}, \quad (2.56)$$

and,

$$B = \begin{pmatrix} (M_1 + 1 - A_2) \sin(\alpha) - E & (M_1 + 1) \sin(\alpha) - E & 0 & 0 \\ (M_1 - 1 + A_2) \sin(\alpha) - E & (-M_1 + 1) \sin(\alpha) + E & -A_2 \sin(\alpha) & 0 \\ A_1 \sin(\alpha) & 0 & (M_2 + 1 - A_1) \sin(\alpha) - E & (M_2 + 1) \sin(\alpha) - E \\ -A_1 \sin(\alpha) & 0 & (M_2 - 1 + A_1) \sin(\alpha) - E & (-M_2 + 1) \sin(\alpha) + E \end{pmatrix}, \quad (2.57)$$

where  $D = M_{\perp} \sin(\alpha)$  and  $E = M_{\perp} \cos(\alpha)$ . Parallel Mach numbers corresponding to plasma entering from below and above to the lunar wake are  $M_1$  and  $M_2$  respectively as shown in Fig. 2.1.

In order to calculate densities and parallel velocities in the wake of the Moon, I consider a 2D rectangular simulation domain which can perfectly cover the wake and beyond. The center of the Moon is at the origin; that is, at coordinates  $(0,0)$ , and in order to avoid singularity in the regions that are very close to the Moon surface in the wake, the calculations are started at around  $X = 2.0 R_m$  up to  $X = 15 R_m$ . In the simulations the spatial resolution in  $X$  and  $Y$  are  $dx = 0.064 R_m$  and  $dy = 0.029 R_m$ , respectively. Equations (2.52) to (2.55) are solved for each row of  $Y$  in the 2-D simulation domain to the next row to the right. As can be seen from Eqs. (2.52) to (2.55), there are nonlinear terms in this system of equations. To address this problem, the nonlinear terms are always evaluated from the previous row (in its left) in the simulation box. The nonlinear terms of the first row in the left boundary ( $X = 2.0 R_m$ ) are determined from the results of the analytic model which is described in the paper [18] and Sec. 2.2. Indeed it was shown in Sec. 2.2 that the analytic model can predict the parallel velocities and densities of the two ion fluids accurately close to the Moon. Therefore, it is a good approximation to use these quantities for the left boundary which lies at  $X = 2.0 R_m$  to solve the Eqs. (2.52) to (2.55). This is justified because at  $X = 2.0 R_m$ , there is a minimal overlap between plasma coming from the top and from the bottom. To calculate the unknowns at a grid point  $(X, Y)$ , matrices  $A$  and  $B$  are constructed, and the zeros of Eq. (2.40),  $\mu_l$ , are found. I assume that the characteristic lines have the same slope between two successive grid points in the  $X$  axis because their interval,  $dx$ , is relatively small. I adjusted  $dx$  in order to give the good accuracy in the results. This is also verified by varying  $dx$  to find the best resolution in  $X$ . Then I compute the characteristic lines associated with the calculated  $\mu_l$  starting at  $(x, y)$  and tracking one step back in  $X$  which the functions  $u^k$  are known. By interpolation, the solutions for  $u^k$  can be found at this new position  $(x-dx, \hat{y})$ , then the four linear superpositions of the unknown functions ( $\hat{u}^l$ ) are calculated by using Eq. (2.46). Hence, I am able to calculate the densities and velocities at the grid point  $(x, y)$  by using the fact that the updated linear superposition of the unknown functions ( $\hat{u}^l$ ) are constant along characteristic lines.

### 2.3.1 Results from the method of characteristics (with coupling) and the analytic model (without coupling) ( $\alpha = 90^\circ$ )

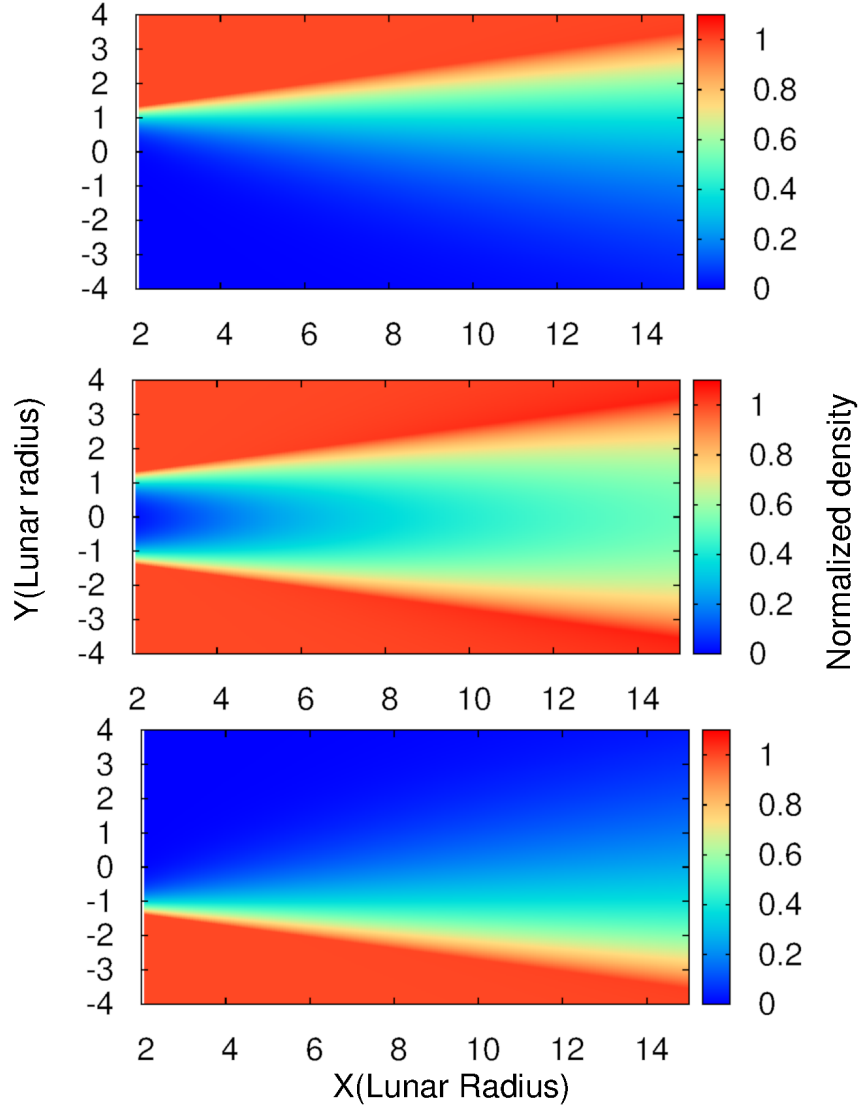


Figure 2.6: Normalized density in the method of characteristics. The upper and lower panels show the ion density of fluid 2 and 1 respectively and the middle panel shows the total normalized density.

In this section results obtained with the method of characteristics, as well as comparisons with results from the analytic model are presented. In the calculations, the solar wind flow velocity is assumed to be in the  $+x$  direction, and the solar wind magnetic field  $\mathbf{B}_{\text{IMF}}$  is in the  $+y$  direction ( $\alpha = 90^\circ$ ) with

a magnitude of  $\sim 6$  nT [68]. The solar wind speed is 295.6 km/s [75], the background density is  $n_{sw} = 3.14 \text{ cm}^{-3}$ , the electron and ion temperatures are  $T_e \simeq 14.3$  eV and  $T_i \simeq 5.7$  eV respectively. These parameters are chosen to be the same as those considered in the analytic model for comparison purposes. Specifically, with the parameters given above, the sound speed is  $c_s \sim 48.8$  km/s and the corresponding upstream Mach number is  $M_\perp \simeq 6$ , and  $M_\parallel = 0$ . In the special case  $\alpha = 90^\circ$ , matrices  $A$ , Eq. (2.56) and  $B$ , Eq. (2.57) are of the form

$$A = \begin{pmatrix} M_\perp & M_\perp & 0 & 0 \\ M_\perp & -M_\perp & 0 & 0 \\ 0 & 0 & M_\perp & M_\perp \\ 0 & 0 & M_\perp & -M_\perp \end{pmatrix}, \quad (2.58)$$

and,

$$B = \begin{pmatrix} M_1 + 1 - A_2 & M_1 + 1 & A_2 & 0 \\ M_1 - 1 + A_2 & -M_1 + 1 & -A_2 & 0 \\ A_1 & 0 & M_2 + 1 - A_1 & M_2 + 1 \\ -A_1 & 0 & M_2 - 1 + A_1 & -M_2 + 1 \end{pmatrix}. \quad (2.59)$$

The Moon blocks the plasma solar wind incident on its surface, thus creating its surface in the upstream, creating a depleted region in the downstream, in the wake region. The method of characteristics can reproduce the lunar wake and wake boundaries as shown in Fig. 2.6. The middle panel corresponds to the total ion density, and the upper and lower panel show the densities related to fluid 2 and 1, respectively. Since the magnetic field is perpendicular to the flow velocity in the upstream,  $n_1$  and  $n_2$  are up-down symmetric. The density gradient between the lunar wake and the solar wind drives plasma in the solar wind to refill the lunar wake along the magnetic field lines. Electrons rush into the wake ahead of ions and make the wake negatively charged. As a result, an ambipolar electric field Eq. 2.19 between the wake and the solar wind accelerates ions into the wake. Closer to the Moon, the density on the wake axis ( $Y = 0$ ) is almost zero because very few ions can reach this point from either side. For example, in the middle of the wake and very close to the Moon  $Y = 0$ ,  $X = 2 R_m$  the density measured by this model is estimated to be  $0.087 n_{sw}$ . It means there are just 0.27 ions in each  $\text{Cm}^3$  which corresponds a very high vacuum. The calculated total density at the

same point,  $Y = 0$ ,  $X = 2 R_m$  from the analytic model is  $0.084 n_{sw}$  which is smaller than the one is calculated from the method of characteristics. In order to compare the effect of interactions between the two ion fluids, an ad hoc coupling coefficient  $0.0 < r < 1.0$  is introduced to multiply the right hand side in the Eqs. 2.52-2.55. The interactions between the two fluids in the method of characteristics are artificially turned off when  $r = 0$ , otherwise the effects of couplings between these counterstreaming fluids are taken into account, when  $r = 1$ . In the method of characteristics, if the counterstreaming fluids do not interact with one another  $r = 0$ , the results of the analytic are recovered with small differences related to the discretization errors.

In Fig. 2.7, the absolute value of the difference between the densities of the two models is plotted in a 2D simulation plane. The lower color plot shows differences in the total density obtained with the analytic model and the one from the method of characteristics for the case when the interactions between the two fluids are artificially turned off ( $|n_{Anal} - n_{(r=0)}|$ ). It can be seen that the maximum difference does not exceed  $0.018 n_{sw}$ , which is found to occur at the wake boundaries. These discrepancies are related to the discretization error in the method of characteristics. However, the upper panel shows the effects of considering the interactions between the two fluids. The maximum differences are inside the wake, which is  $\sim 0.03 n_{sw}$ .

To be able to interpret the consequences of interactions between the two ion fluids, the normalized total ion density of both models are compared along three different cuts in  $X$  in front of the wake in Fig. 2.8. The densities are found to be minimum at the center of the wake and to increase as expected away from the Moon. Comparisons are made at  $X = 15 R_m$ ,  $X = 9 R_m$  and  $X = 3 R_m$  from top to bottom. Qualitatively, the analytic model creates a deeper wake as expected. Ions are accelerating into the wake from both sides; consequently, they have substantial parallel velocities as they are advancing to the wake. Since there is nothing to stop them in the absence of interactions, they reach the opposite side of the wake boundary and beyond without slowing down. As a result, the density in the wake center is smaller in comparison to the one obtained from the method of characteristics in which coupling between

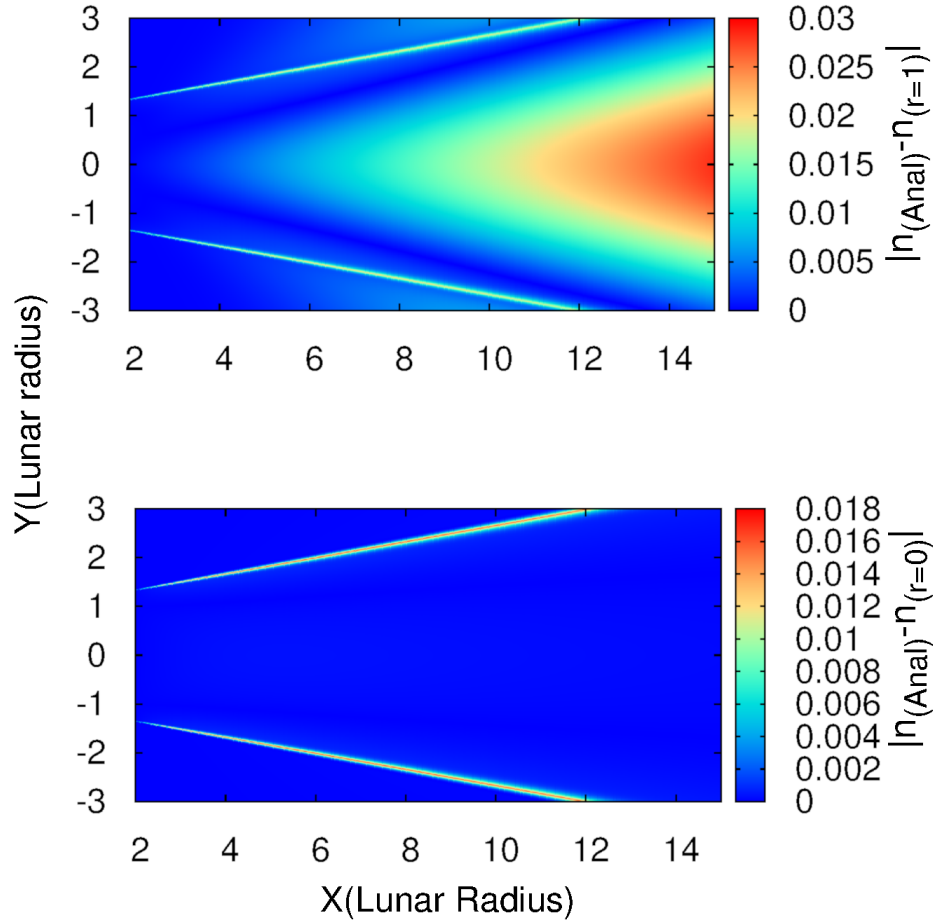


Figure 2.7: Differences in absolute value between the density of the analytic model ( $n_{Anal}$ ) and the density computed from the method of characteristics when: 1- the interactions between the two fluids are artificially turned off ( $n_{(r=0)}$ ) (lower panel), 2- the interactions are taken into account ( $n_{(r=1)}$ ) (upper panel).

the two fluids is taken into account. While the two fluids are interacting, their parallel velocities is reduced in absolute value due to the opposing ambipolar electric field of the counterstreaming fluid, leading to a larger density of ions on the axis of the wake; therefore, more ions can be found in the center of the wake. Closer to the Moon  $X = 3 R_m$  the density profiles from the two models are in a very good agreement. The maximum difference occurs in a narrow range at the wake edge where the differences do not exceed  $\sim 0.008 n_{sw}$  and at the center of the wake  $Y = 0$  the difference between total density from the two models is  $\sim 0.0029 n_{sw}$  which is very small. Further from the Moon surface, the differences between the two model are increasing. For instance, at  $X = 9 R_m$ , the largest difference happens at the wake center  $Y = 0$  which is  $\sim 0.018 n_{sw}$ , and at the edge of the wake  $Y = \pm 1.5 R_m$  it does not exceed  $\sim 0.012 n_{sw}$ . Finally, at  $X = 15 R_m$ , the maximum discrepancy occurs in the wake center which is  $\sim 0.03 n_{sw}$ . Quantitatively, the two densities agree within  $\simeq 6\%$  almost everywhere. The discrepancy occurs in the narrow range at the wake edge does not exceed  $\sim 0.018 n_{sw}$ , which comes from the discretization errors (refer to Fig. 2.7). Empirically, by reducing the  $X$  and  $Y$  resolution, the differences in densities in this area get smaller and the least discretization error happens when  $dx = 0.0065 R_m$  and  $dy = 0.004 R_m$ .

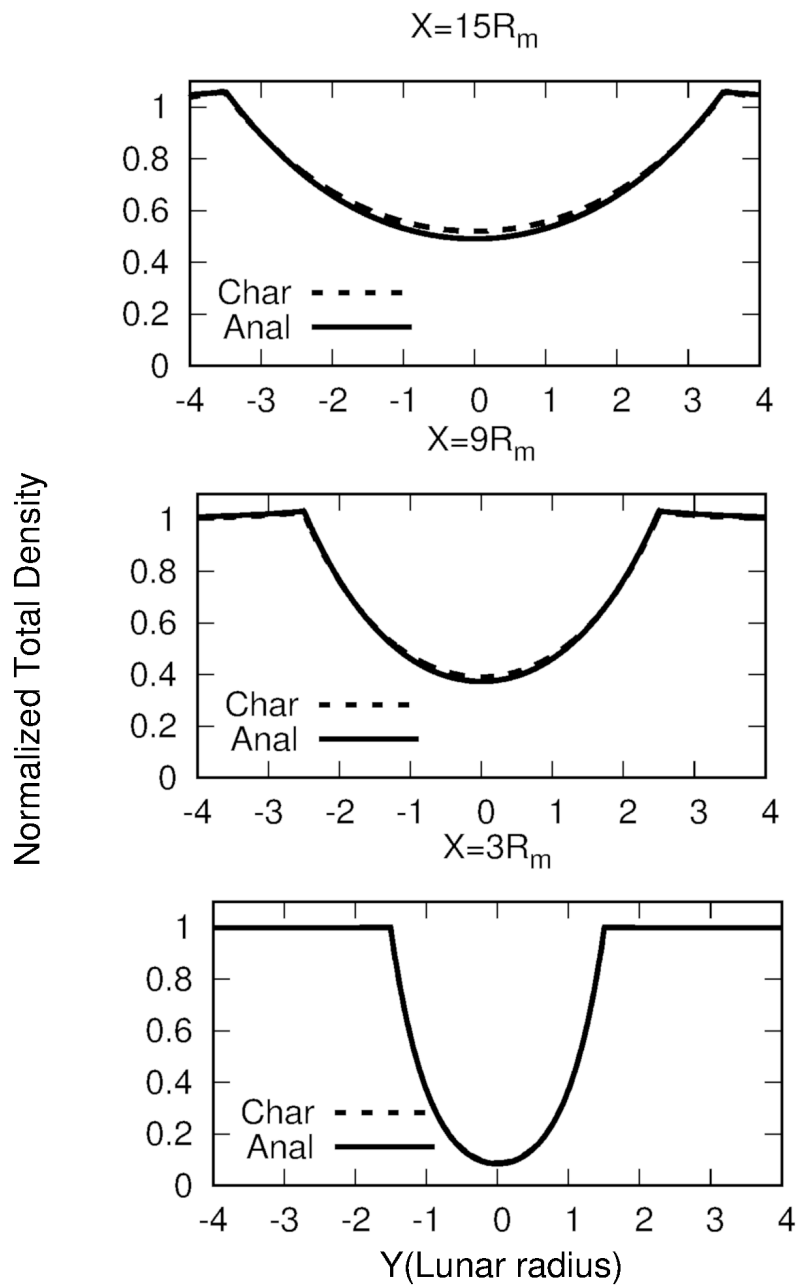


Figure 2.8: Comparison between the normalized total ion density calculated with the method of characteristics (dotted line) and analytic model (solid line) along  $Y$  at different cuts in  $X$ . From top to bottom,  $X = 15 R_m$ ,  $X = 9 R_m$  and  $X = 3 R_m$ .

**Parallel velocity:** Figure 2.9 shows the parallel velocity of ions calculated with the method of characteristics. The upper panel shows the parallel velocity of ions accelerating into the wake from above, and the lower panel shows the parallel velocity of ions enter the wake from below. As expected there is symmetry between the quantities related to the fluid 1 and fluid 2 because the magnetic field is perpendicular to the upstream flow velocity. Ions are moving along the magnetic field (along  $Y$  axis in this particular case) and create a void region. Similar to the analytic model ion parallel velocities increase in absolute value while expanding to the wake from both sides Fig. 2.9. Parallel

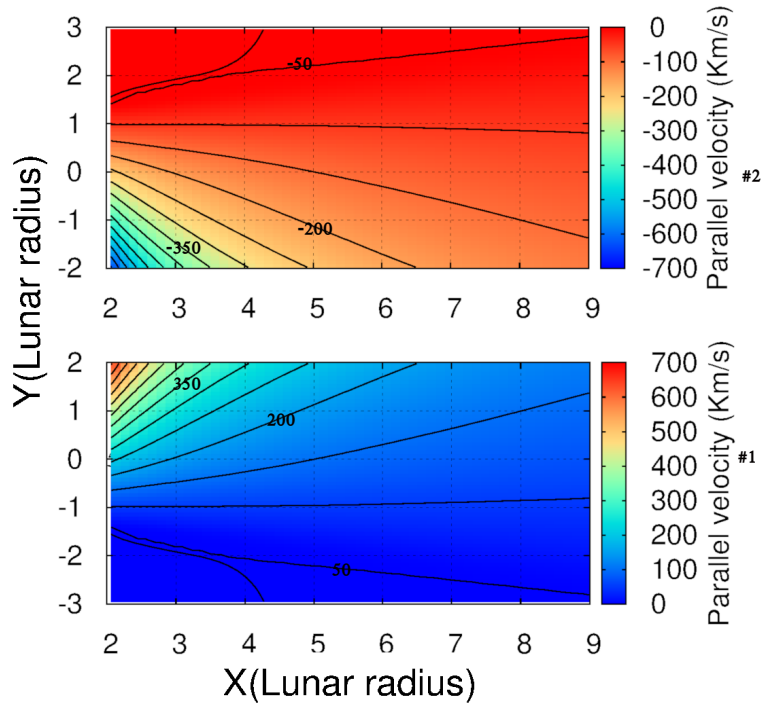


Figure 2.9: Parallel velocity of ions in the method of characteristics. Upper and lower panel shows the parallel velocity of ions entering the wake from above and below the wake respectively.

velocities of the fluid 1 computed from the two models are compared at three different cuts in  $X$ , from top to bottom,  $X = 15 R_m$ ,  $X = 9 R_m$  and  $X = 3 R_m$ . As discussed above, I expected to see ion parallel velocities to be smaller in absolute value when calculated with the method of characteristics compared to those obtained with the analytic model 2.10. Again, if the comparisons are

made closer to the Moon, the differences are less because the analytic model is very accurate close to the Moon surface. The parallel flow velocity of ions entering the wake is computed from the two models and is plotted in Fig. 2.12. Because magnetic field is perpendicular to the upstream flow velocity, fluids are moving to refill the vacuum in the opposite directions along magnetic field  $M_{1\parallel} = -M_{2\parallel}$ .  $M_{1\parallel}$  in the unperturbed solar wind region ( $X = 3 R_m, Y = -3 R_m$ ) is zero and it increases in absolute value as fluid 1 expands to the wake center (it is illustrated in Fig. 2.33).  $M_{2\parallel}$  is zero in the unperturbed region ( $X = 3 R_m, Y = 3 R_m$ ) where the upstream normalized density related to the fluid 2 is  $n_2 = 1$ . But as fluid 1 penetrates the wake from below the parallel velocity gets bigger while the density in the center of the wake gets very small. By this analysis the parallel velocity of ions on the opposite boundaries are very high, but a small fraction of the corresponding ions can reach there.

**Parallel flux:** Figure 2.11 shows the normalized parallel ion flux  $\Gamma_{1,2 \parallel} = (n_{1,2} M_{1,2 \parallel}) / n_{sw0}$ , where  $n_{sw0}$  is the upstream solar wind density and the net normalized flux is  $\Gamma = \Gamma_{1 \parallel} + \Gamma_{2 \parallel}$ . The middle panel shows the approximate net flux which would be obtained from a fluid simulation: negative and positive parallel flows, above and below the  $X$  axis, correspond to plasma entering the wake from above and below respectively. The net ion parallel flow at the center of the wake (at  $Y = 0$ ) vanishes by symmetry, but the fact that it is associated with two counter-streaming flows would be missing from single-fluid models (such as Hutchinson's model). Normalized parallel ion flux of the analytic model is compared with the ones computed from the method of characteristics at three different cuts along  $Y$ , from the top to bottom,  $X = 15 R_m$ ,  $X = 9 R_m$  and  $X = 3 R_m$  (look at Fig. 2.12). The net ion parallel flow at the center of the wake (at  $Y = 0$ ) vanishes by symmetry. Figure 2.13 shows the parallel flux of fluid from two models along  $Y$  at three cuts in  $X$ , from top to bottom,  $X = 15 R_m$ ,  $X = 9 R_m$  and  $X = 3 R_m$ .

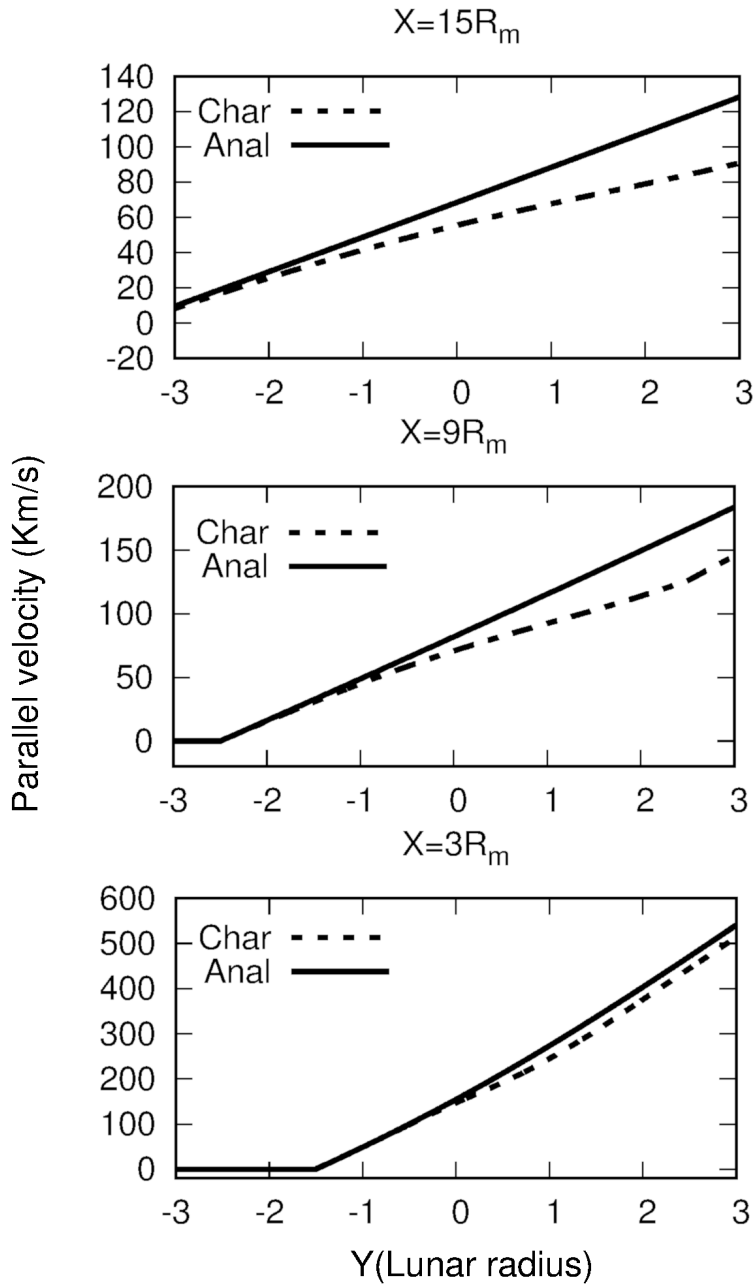


Figure 2.10: Comparison between the parallel velocity of particles penetrating into the wake from below computed by the method of characteristics (dotted line) and analytic model(solid line) along  $Y$  at different cuts in  $X$ . From top to bottom,  $X = 15 R_m$ ,  $X = 9 R_m$  and  $X = 3 R_m$ .

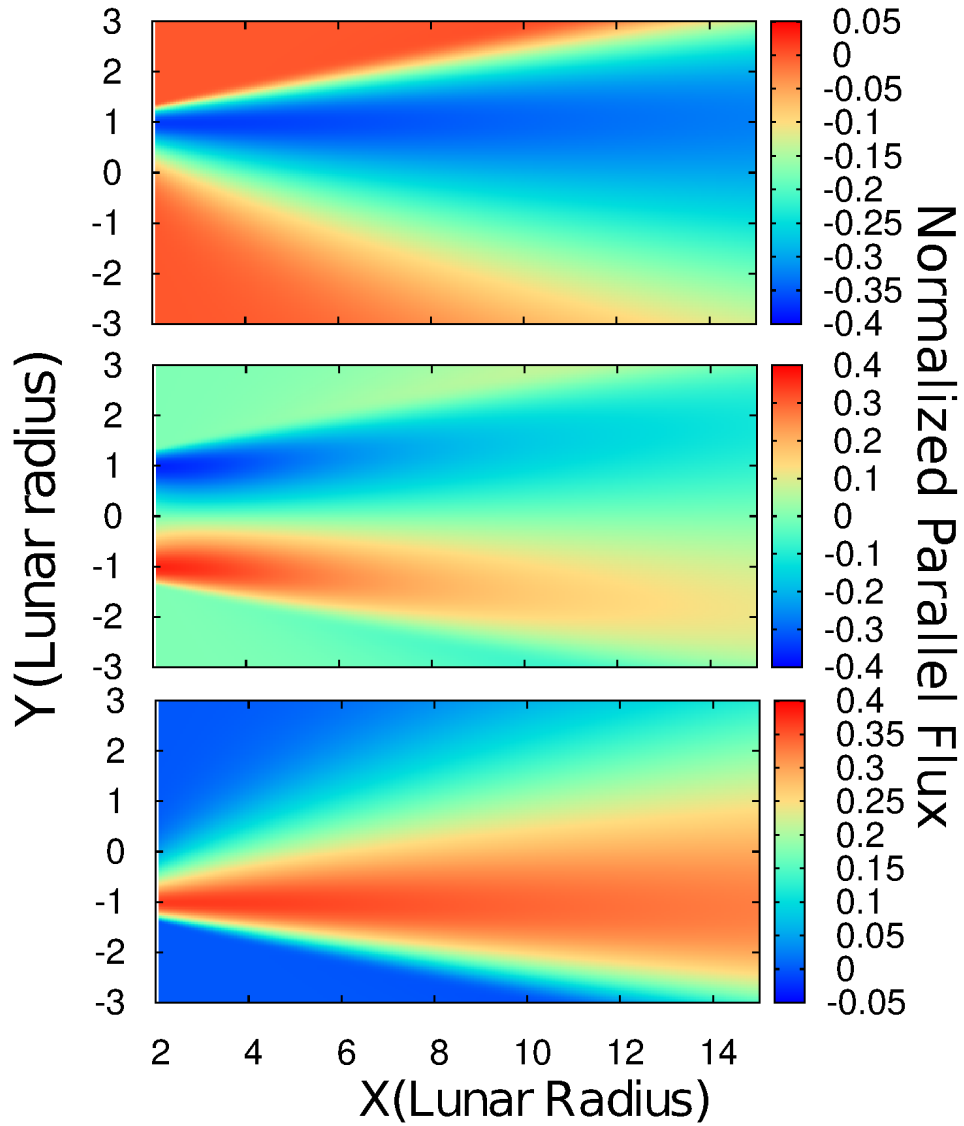


Figure 2.11: Normalized plasma parallel flux along the magnetic field in the method of characteristics. Plasma entering the wake from directions above and below the wake is shown in the upper and lower panels, respectively. The middle panel shows the net normalized parallel flux.

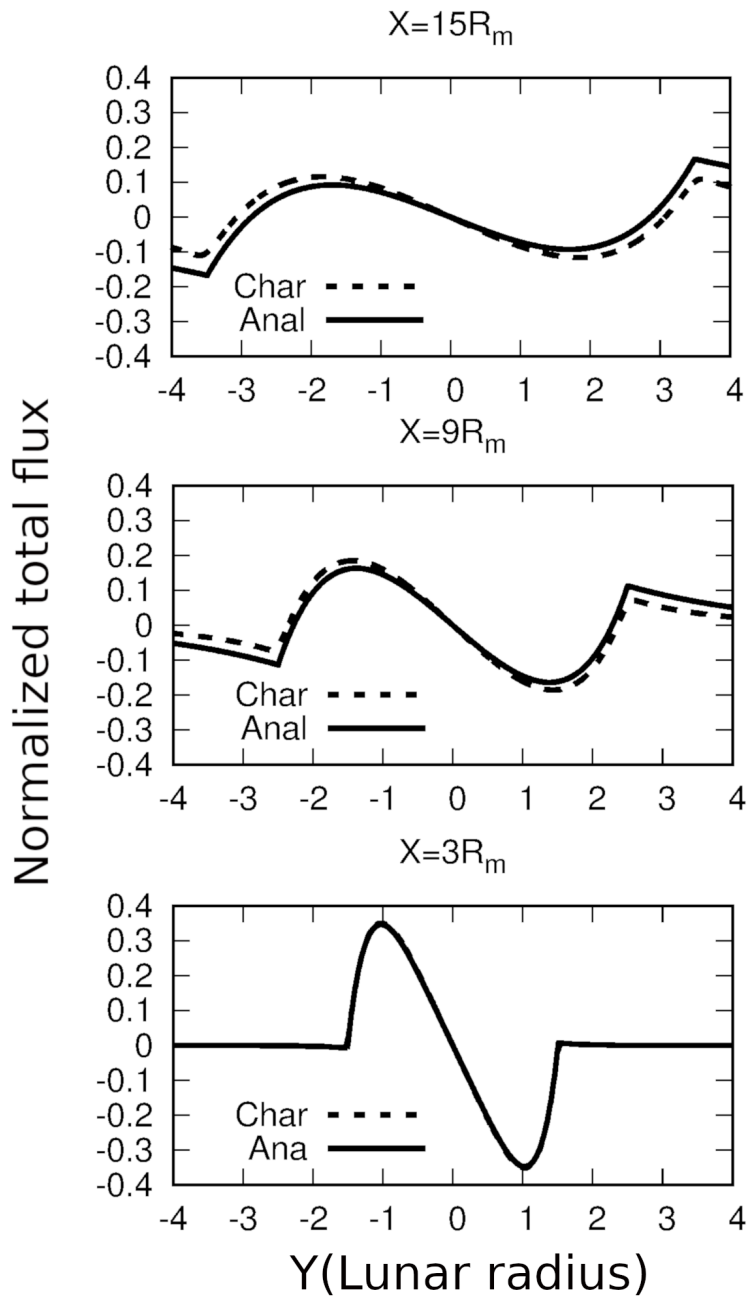


Figure 2.12: Comparison between the normalized total parallel ion flux of the method of characteristics (dotted line) and analytic model (solid line) along  $Y$  at different cuts in  $X$  when  $(\alpha = 90^\circ)$ . From top to bottom,  $X = 9 R_m$ ,  $X = 6 R_m$  and  $X = 3 R_m$ .

The total parallel flux shows some small negative/positive fluxes in the unperturbed region below/above the center of the void. As can be seen they are smaller in absolute value in the method of characteristics than from the approximate analytic model Fig. 2.12. A tiny amount of each fluid can reach the opposite wake boundary and beyond in the method of characteristics. In the analytic model the two ion fluids are independent, there is more negative/positive flux that can be seen beyond the lower/above wake boundaries in comparisons to the ones from the method of characteristics. This is the effect of the coupling between the two ion fluids. Qualitatively, the total flux computed from both models agrees. The maximum discrepancies between the flux from the two models do not exceed 0.07 of the upstream flux  $\Gamma_{sw}$ . Just like the density profile, closer to the Moon, the agreement is better. Interestingly, the good qualitative and quantitative agreement between the two models indicates that despite its simplicity the analytic model is capable of capturing much of the physics at play in the formation of the lunar wake in this approximate 2D model.

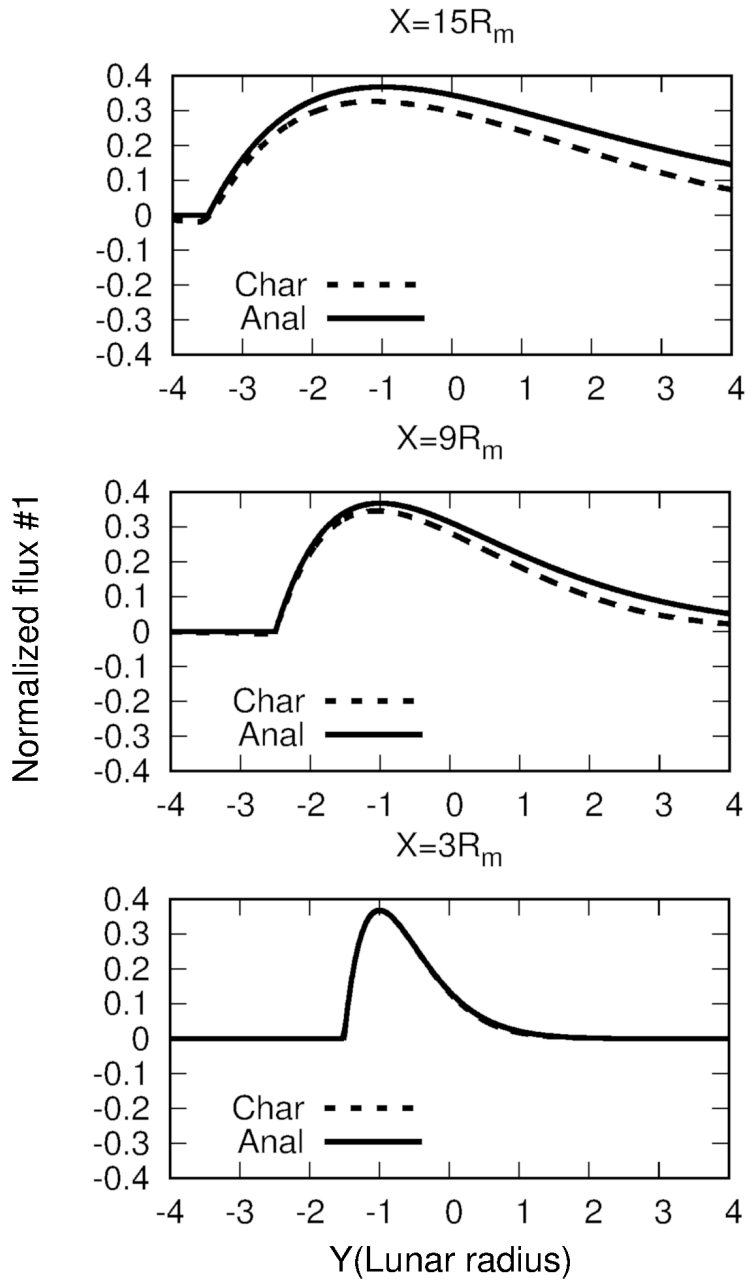


Figure 2.13: Comparison between the normalized parallel ion flux of fluid 1 computed from the method of characteristics (dotted line) and analytic model (solid line) along  $Y$  at different cuts in  $X$  when ( $\alpha = 90^\circ$ ). From top to bottom,  $X = 15 R_m$ ,  $X = 9 R_m$  and  $X = 3 R_m$ .

### 2.3.2 Comparisons between the method of characteristics and the analytic model ( $\alpha \neq 90^\circ$ )

In the previous section, I limited my attention to the special case where the magnetic field is perpendicular to the upstream flow velocity; that is to  $\alpha = 90^\circ$ . In this section, a general case is discussed where  $\alpha$  is not 90 degrees. The length of the wake depends on the interplanetary magnetic field (IMF) orientation. It is shorter when the perpendicular component of IMF is larger [28]. Michel [54] predicts that solar wind protons are accelerated to the ion-acoustic velocity into the wake. The wake is confined by the inner Mach cone of the angle  $\beta = C_s/V_{SW}$  [34]. However, in the general case where there is an angle  $\alpha$  between the  $\mathbf{B}_{IMF}$  and  $\mathbf{V}_{SW}$ , then the bulk plasma velocity of ions penetrating toward the wake center is different in the opposite sides of the wake. Asymmetries in the lunar wake structure are produced when the magnetic field is not perpendicular to the solar wind velocity [65]. The asymmetry in the lunar wake is observed by some of the lunar missions such as the Explorer 35 satellite [34], the Wind [56], LRO [21] and ARTEMIS [23]. The parameters used to plot the results in this section are as below [62]. Ion and electron temperatures  $T_i = 5\text{eV}$  and  $T_e = 9\text{eV}$ . The magnetic field is  $\mathbf{B}_{IMF} = [-1.5, 0.0, -1.0]\text{nT}$ . The solar wind flow velocity and density are  $\mathbf{V}_{sw} = 320\text{Km/s}$  and  $n_{sw} = 7.0 \text{ cm}^{-3}$ . Figure 2.17 shows the total density of ions computed with the method of characteristics for three different IMF orientations. In all cases, the solar wind velocity is in the  $X$  direction, and the interplanetary magnetic field has an angle  $\alpha$  with respect to  $X$  in this  $x - y$  plane. I also observed the different inner cone angles for the two counterstreaming fluid in the wake region in results obtained with the method of characteristics. Figure 2.14 shows normalized parallel flux calculated by the method of characteristics for the case  $\alpha = 33^\circ$ . The upper panel shows the flux of ions penetrating to the wake from above and the lower panel is the flux of ions entering the wake from below. The middle panel shows the net flux. Unlike the case where  $\mathbf{V}_{sw}$  and  $\mathbf{B}$  are perpendicular, there is no symmetry between the upper and lower panel. There is a small difference between the

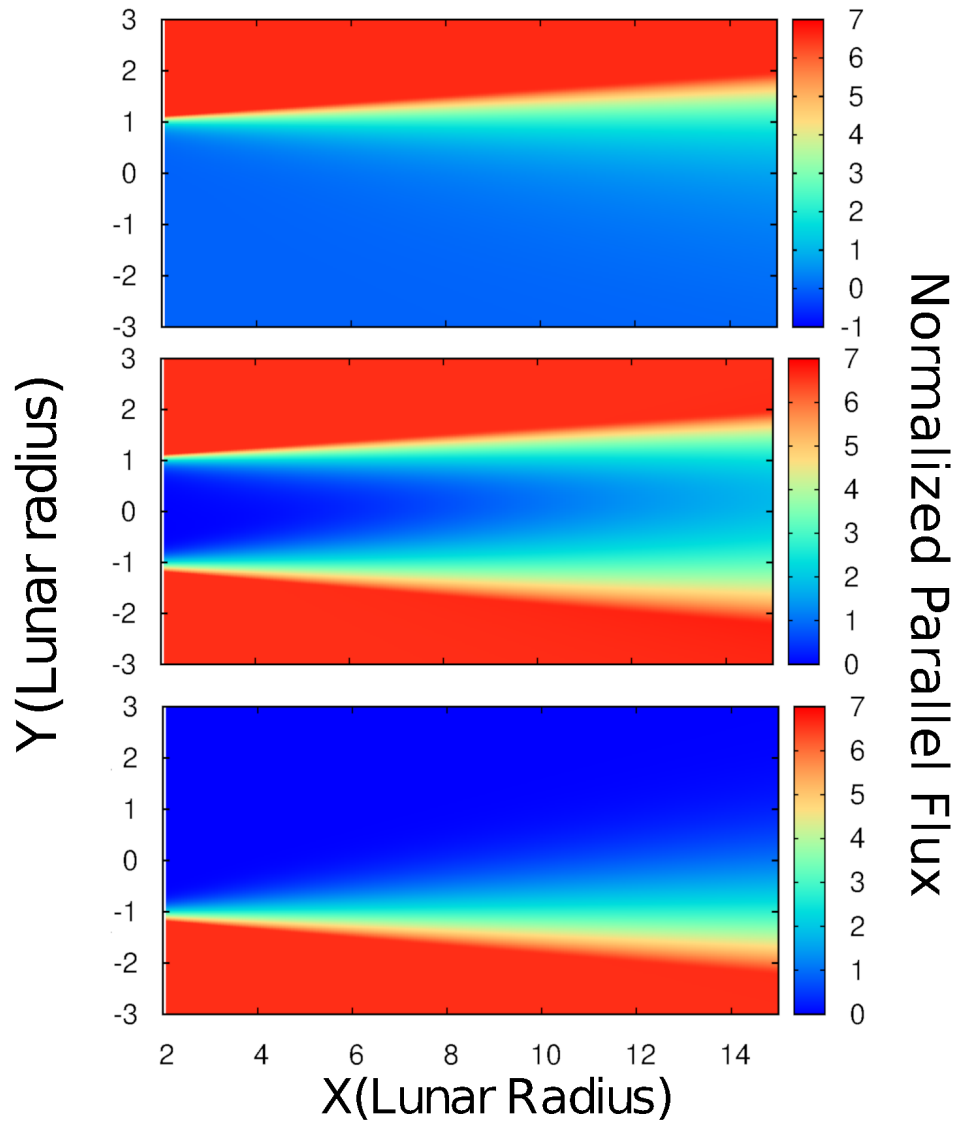


Figure 2.14: Normalized plasma parallel flux in the method of characteristics ( $\alpha = 33^\circ$ ). Plasma entering the wake from directions above and below the wake is shown in the upper and lower panels, respectively. The middle panel shows the net normalized parallel flux.

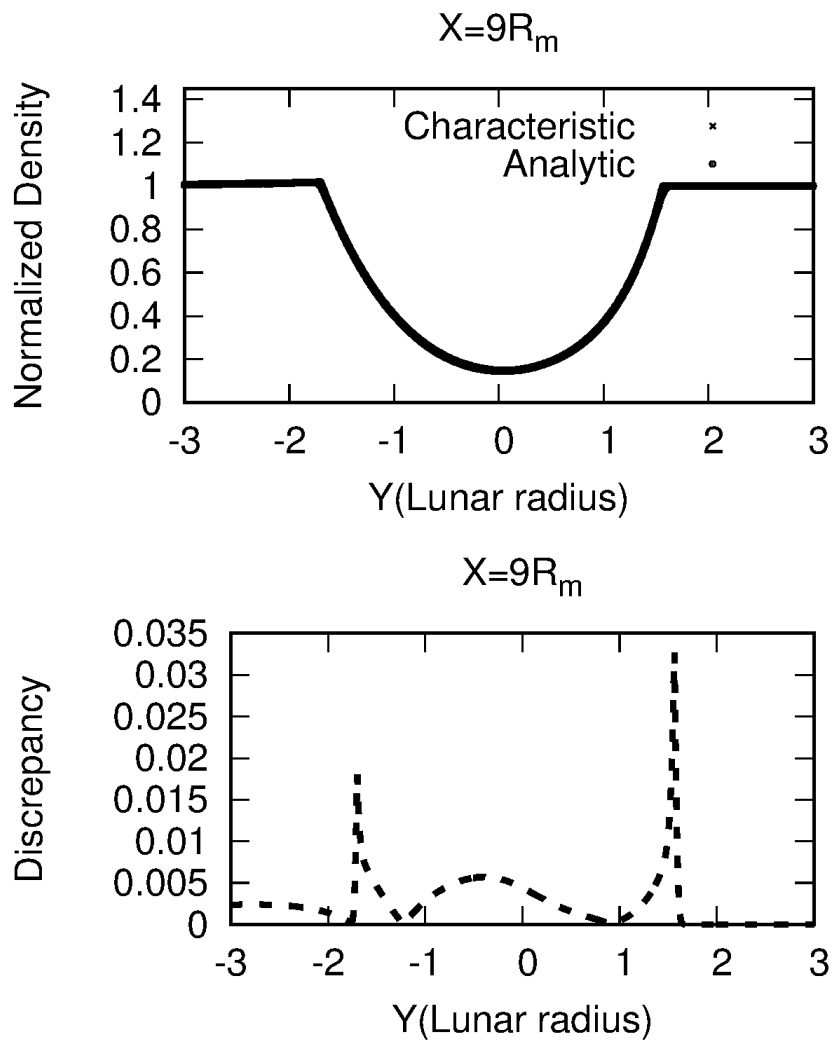


Figure 2.15: The normalized total ion density from the method of characteristics and the analytic model are plotted along  $Y$  at  $X = 9 R_m$  for the case where  $\alpha = 33^\circ$  (upper panel). The differences between the densities from the method of characteristics and the analytic model in absolute value is shown along  $Y$  at  $X = 9 R_m$  for the case where  $\alpha = 33^\circ$  (lower panel).

results obtained with the method of characteristics and the analytic model. In the method of characteristics, unlike the analytic model, the interaction between the two ion fluids coming to the center of the wake from both sides are considered. However, results show that the interaction between the two ion fluids does not generate a significant change in the density and flux profiles. Figure 2.15 shows comparisons between the density from the analytic model and that of the method of characteristics as a function of  $Y$  at a cut in  $X = 9 R_m$ . The lower figure shows the discrepancy between the two densities. Densities obtained with the two models are in a good agreement almost everywhere within  $\sim 1\%$  except at the two edges of the wake where the difference is within  $\sim 3.5\%$ . The total normalized flux from the two models is compared in Fig. 2.16. At the two edges the discrepancy is higher, at approximately  $\sim 25\%$ .

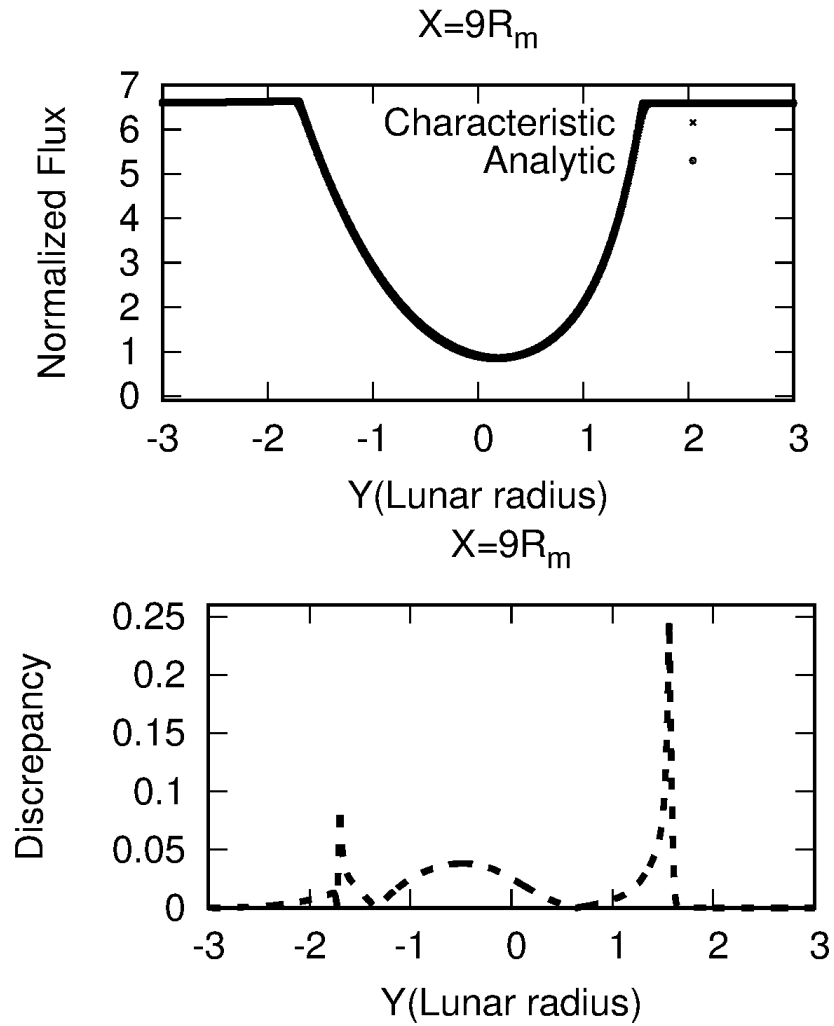


Figure 2.16: The normalized total parallel flux from the method of characteristics and the analytic model are plotted along  $Y$  at  $X = 9 R_m$  for the case where  $\alpha = 33^\circ$  (upper panel). The differences between the net parallel fluxes from the method of characteristics and the analytic model in absolute value is shown along  $Y$  at  $X = 9 R_m$  for the case where  $\alpha = 33^\circ$  (lower panel).

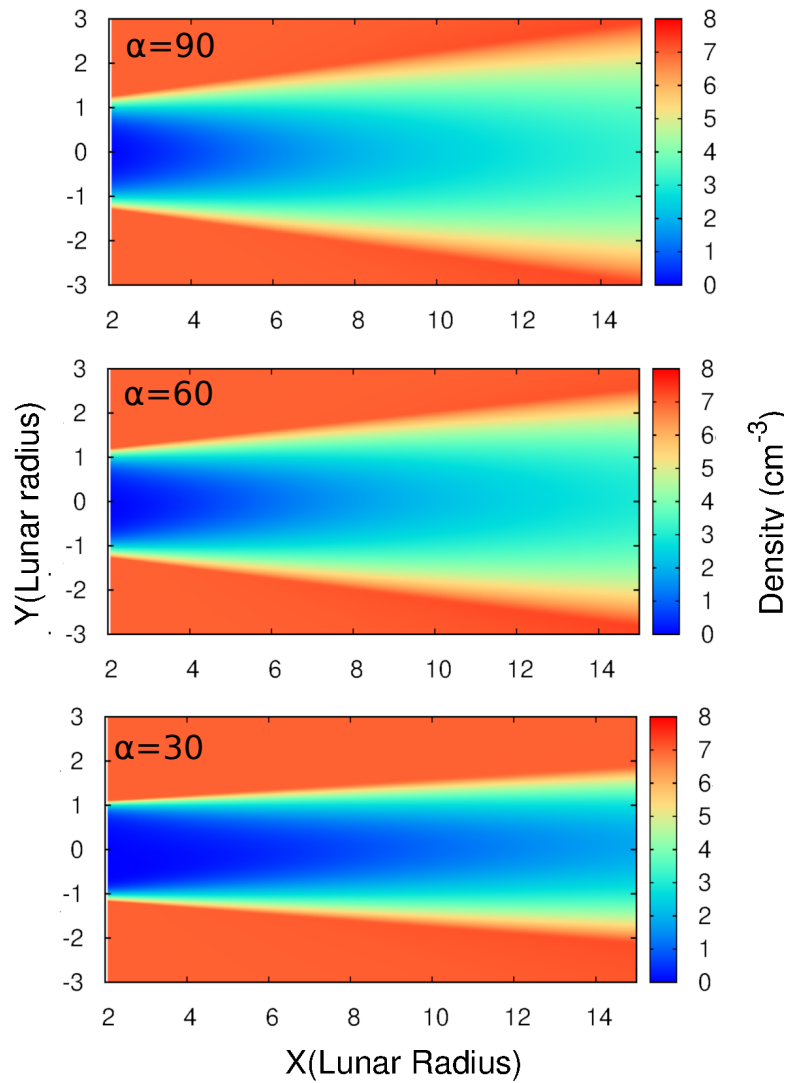


Figure 2.17: Computed total density of the plasma with the method of characteristics for three different IMF orientations. From bottom to top,  $\alpha = 30^\circ$ ,  $\alpha = 60^\circ$  and  $\alpha = 90^\circ$ .

# Chapter 3

## Hybrid-kinetic and Finite element models

In this chapter two other computer models are introduced to scrutinize some features of the lunar wake. These approaches are: a hybrid-kinetic model and a finite element model. A short description of each model is provided and the codes are adjusted to be compatible with the two-dimensional model of the wake model presented in the previous chapter. Results obtained from these models are compared with the ones from the method of characteristics to examine the similarities and differences.

### 3.1 Hybrid-kinetic model

Hybrid-kinetic models, in which ions are treated kinetically and electrons as a fluid, have been applied to study macroscopic and fine-scale kinetic aspects of lunar wake dynamics. These codes are used to model phenomena that occur on shorter time and distance scales than be treated by MHD and yet do not resolve processes that occur on electron particle scales. The relevant scales are then the ion gyro-radius and ion inertial length for spatial scales, and inverse ion gyrofrequency for time scales. In space physics, these length scales typically are on the order of 10's to 100's of km and times are on the order of seconds; satellite instrumentation [76] readily resolves these ion scales. Research has been done to stimulate the lunar wake with different hybrid models. For example, 2D hybrid-kinetic models have revealed that low-

frequency electromagnetic turbulence [70] dominates the downstream region of the lunar wake ( $28R_M < x < 40R_M$ ). Kallio [38] presented the first 3D hybrid simulation of the Moon-solar wind interaction and showed that a long tail ( $> 10 R_m$ ) of depleted plasma density forms in the night-side, along with an enhancement in the magnetic field in the wake boundary and a decreased field in the center of the wake. Wang et al. [74] used a 3D hybrid code to study electromagnetic disturbances in the solar wind and showed that the magnetic field was enhanced by a factor of about 1.4 in the middle of the lunar wake, with depletions at the two sides due to the lunar absorption effect. A similar approach used by Holmstrom et al. [28] predicts the occurrence of kinks in the magnetic field at the wake boundary. A 3D hybrid model was also applied to investigate a view of the current systems in the lunar wake, and it was shown that the current is confined around the vacuum region as well as rarefaction boundaries [14]. A 1D hybrid code was used for the first time to demonstrate the formation of the standing shock wave behind the Moon [34]. It was used to show that the shock is created by the interaction of counterstreaming ion beams in the plane containing the solar wind velocity and the magnetic field.

### 3.1.1 Implementation the hybrid code

The 2D hybrid-kinetic electromagnetic model, previously used by Paral [58] to model the solar wind interaction with planet Mercury, is employed in order to study the solar wind interaction with the Moon [18]. This model ignores electron kinetic effects but correctly accounts for ion gyro-radius effects that are important for small ion scale structures like discontinuities formed in the lunar wake. The approximations made in the hybrid models are: **1- Quasi-neutrality**, **2- Darwin approximation**, **3- Adiabatic pressure**, **4- Massless Electrons**. Electrons are treated as a massless, charge-neutralizing fluid, which prohibits parallel electric fields from forming, while ions are considered as particles. With this assumption, the plasma mass density is only the ion mass density, and the electron gyrofrequency and the electron plasma frequency are neglected from the equations. Quasi-neutrality is only valid for grid resolutions larger than the Debye Length  $\lambda_D$  which leads to  $\nabla \cdot \mathbf{J} = 0$ .

Where  $\mathbf{J} = \sum \mathbf{J}_s$  is the total current density, and this condition removes most electrostatic instabilities [13]. Besides, the low frequency magnetostatic (Darwin) approximation is made by ignoring the displacement current in Maxwell's equations. The Darwin approximation leads to a set of equations which describe the temporal and spatial evolution of the electromagnetic fields and the plasma [37], [52]. The equation of motion of ion particles of species  $s$  under the influence of Coulomb and Lorentz forces are

$$\frac{d\mathbf{X}_s}{dt} = \mathbf{V}_s, \quad (3.1)$$

$$\frac{d\mathbf{V}_s}{dt} = \frac{q_s}{m_s} (\mathbf{E} + \mathbf{V}_s \times \mathbf{B}). \quad (3.2)$$

Where,  $\mathbf{X}_s, \mathbf{V}_s, m_s$  and  $q_s$  are positions, velocities, masses and charges of ion species respectively. Electric and magnetic fields are respectively as  $\mathbf{E}$  and  $\mathbf{B}$ . Electrons are treated as a fluid and conservation of the momentum for electrons can be used to consider the electron dynamics,

$$\frac{\partial(n_e)}{\partial t} + \nabla \cdot (n_e \mathbf{u}_e) = 0, \quad (3.3)$$

$$\frac{\partial(m_e n_e \mathbf{u}_e)}{\partial t} + \nabla \cdot (m_e n_e \mathbf{u}_e \mathbf{u}_e) = n_e q_e (\mathbf{E} + \mathbf{u}_e \times \mathbf{B}) - \nabla p_e. \quad (3.4)$$

Electron quantities are expressed with the subscript  $e$ :  $n_e, m_e, \mathbf{u}_e$  and  $q_e = -e$  are density, mass, fluid velocity and charge, respectively. The electron current density and electron fluid pressure are,  $\mathbf{J}_e = -n_e e \mathbf{u}_e$  and  $p_e$ . The first and the second term on the left side of this equation account for the time and spatial variations of electron momentum per unit volume respectively. By doing some algebra and considering the continuity equation 3.3, the left side of this equation can be expressed as the total time derivative (refer to Eq. (1.6)),

$$\frac{d\mathbf{u}_e}{dt} = \frac{\partial \mathbf{u}_e}{\partial t} + (\mathbf{u}_e \cdot \nabla) \mathbf{u}_e. \quad (3.5)$$

Henceforth, the right-hand side of the momentum equation represents the variations of forces per unit volume; the first term is the electromagnetic force, and the second term is the pressure gradient force [20], [60]. Therefore consistently with the massless electron assumption the electron momentum equation

becomes,

$$n_e m_e \frac{d\mathbf{u}_e}{dt} = -n_e e \mathbf{E} + \mathbf{J}_e \times \mathbf{B} - \nabla p_e = 0. \quad (3.6)$$

Therefore, an approximated form of Ampere's law is used to obtain total current density  $\mathbf{J} = \mathbf{J}_e + \mathbf{J}_i$ ,

$$\nabla \times \mathbf{B} = \mu_0 \mathbf{J}. \quad (3.7)$$

Now, the eqs. 3.6 and 3.7 are combined and the electric field becomes,

$$\mathbf{E} = -\frac{\mathbf{J}_i \times \mathbf{B}}{\rho} + \frac{(\nabla \times \mathbf{B}) \times \mathbf{B}}{\mu_0 \rho} - \frac{\nabla p_e}{\rho} + R \frac{\nabla \times \mathbf{B}}{\mu_0}, \quad (3.8)$$

where  $\rho = n_s q_s$  is the charge density and  $\mu_0$  is magnetic permeability of free space. As it can be seen an artificial resistivity  $R$  is added to Eq. 3.8 which causes damping of high frequency waves that would interact with electrons [58]. The magnetic field is advanced in time with Faraday's law ( $\partial \mathbf{B} / \partial t = -\nabla \times \mathbf{E}$ ). Then, Eq. 3.8 is combined with the Faraday's law and the time evolution of magnetic field becomes

$$\frac{\partial \mathbf{B}}{\partial t} = \nabla \times \left( \frac{\mathbf{J}_i \times \mathbf{B}}{\rho} \right) - \nabla \times \left( \frac{(\nabla \times \mathbf{B}) \times \mathbf{B}}{\rho \mu_0} \right) - R \nabla \times \left( \frac{\nabla \times \mathbf{B}}{\mu_0} \right). \quad (3.9)$$

To close this system of equations an adiabatic electron pressure is assumed to respond adiabatically with changes in density, as

$$p_e = p_{e0} \left( \frac{n_e}{n_{e0}} \right)^\gamma, \quad (3.10)$$

where,  $\gamma$ , is the adiabatic index,  $p_{e0}$  and  $n_{e0}$  are electron pressure and number density of the unperturbed plasma region. A set of equations which describe the temporal and spatial evolution of the electromagnetic fields and the plasma are hence derived [37], [52]. Choosing the inner boundary conditions at the lunar surface is very important in hybrid simulations of the Moon. The solar wind is incident at the lunar surface on the day-side and it is absorbed by it, so the inner boundary should be defined in a way to remove all the ions on the night-side. However, this boundary condition makes a discontinuity in the density of ions from the ambient values outside the Moon, to the zero value inside the Moon. This discontinuity causes numerical oscillations and

instabilities in calculating the fields. A solution to this consists of removing ions gradually from the inner boundary to avoid a discontinuity [28]. In other words, the hybrid code imposes a lower bound on density for the numerical stability which is affected by the number of particles per computational cell. In my simulations, particles penetrate the Moon from the day-side in the upper boundary and  $\sim 85\%$  of particles are prevented from moving to the wake. The remaining 15% are artificially allowed to enter the wake on the night side, in order to prevent numerical instabilities.

### 3.1.2 Results obtained from the method of characteristics, and the hybrid model

I now compare results obtained from the method of characteristics with those of the 2D hybrid model. This serves to assess the validity of the assumptions made in the analytic model (or the method of characteristics), and its skill in describing the main features of the lunar wake. A summary of the main similarities and differences between the method of characteristics and the hybrid model is given in Table. 3.1. One constraint is introduced in the

Table 3.1: Main similarities and differences between the method of characteristics and the hybrid model

	Characteristics	Hybrid
Similarities	2D cylindrical	
	isothermal fluid electrons	
Differences	magnetized fluid ions	kinetic ions
	stationary	time dependent
	uniform and constant $\mathbf{B}$	solves for $\mathbf{E}$ and $\mathbf{B}$
	$M_{\perp}$ constant	$M_{\perp}$ variable

hybrid model: the time evolution of the solar wind magnetic field both inside and outside of the Moon is artificially turned off to be consistent with the assumption made in the analytic and characteristics model. All simulations made with the hybrid code are carried out until steady state was obtained. We note that although several models have proposed to simulate convection and diffusion of the IMF through the Moon, these models are not ideal for comparison because they make ad hoc assumptions that cause perturbations

in  $\mathbf{B}$  to depend on their specific implementation. This is primarily a result of the low-density plasma inside the wake; for models to be numerically stable, particles are artificially injected into the wake from the night-side of the Moon. A more physical assumption for assuming that  $\mathbf{B}$  is constant is that because of the low conductivity of the Moon, the IMF penetrates more or less unimpeded. The constant magnetic field approximation is also supported by the relatively small variations in  $\mathbf{B}$  observed with ARTEMIS [75]. While variations in  $\mathbf{B}$  within the wake are not accounted for in the analytic model, some features of wake physics are reproduced using this model. In the 2D hybrid code, the solar wind flow is assumed to be in the  $+x$  direction, and the solar wind magnetic field  $\mathbf{B}_{\text{IMF}}$  is in the  $+y$  direction ( $\alpha = 90^\circ$ ) with a magnitude of  $\sim 6$  nT [68]. The solar wind speed is 295.6 km/s [75], the background density is  $n_{\text{sw}} = 3.14$  cm $^{-3}$ , the electron and ion temperatures are  $T_e \simeq 14.3$  eV ( $\beta_e \simeq 0.5$ ) and  $T_i \simeq 5.7$  eV ( $\beta_i \simeq 0.2$ ). The dimensions of the simulation box used in the hybrid model is  $(400 \times 400)$  ( $c/\omega_{p,i0}$ ) where  $c$  is the speed of light,  $\omega_{p,i0}$  is the proton plasma frequency in the ambient solar wind, and  $c/\omega_{p,i0}$  is the inertial length of the solar wind protons is  $\sim 129.58$  km. In the hybrid code the grid cell size and time step are set to be  $(0.5 \times 0.5)(c/\omega_{p,i0})$  and  $\Delta t = 0.006 \Omega_{i0}^{-1}$ , respectively, where  $\Omega_{i0} \sim 0.38$  s $^{-1}$  is the proton gyrofrequency in the solar wind. With these parameters, the simulation domain used in the hybrid simulations extends over  $+11 R_M$  in  $X$  and  $\pm 5 R_M$  in  $Y$ , where  $R_M \sim 1737$  km. Specifically, with the parameters given above, the sound speed is  $C_s \sim 48.8$  km/s and the corresponding upstream Mach number is  $M_\perp \simeq 6$  and  $M_\parallel = 0$ . The same parameters are used in the analytic model and the method of characteristics to be able to compare the results. These parameters correspond to those from the first flyby of ARTEMIS P1 through the lunar wake [18], [68], [75] and are also used in the Ch. 2. Recall that in the hybrid code the perpendicular velocity is not assumed to be constant, while it is invariant in the analytic (characteristics) model. As a first comparison, Figures 3.1 and 3.2 show the perpendicular Mach number, normalized to its upstream value, and the density obtained from the hybrid model. In contrast to the assumption of constant perpendicular velocity (in  $Y$  direction) made in the analytic model,

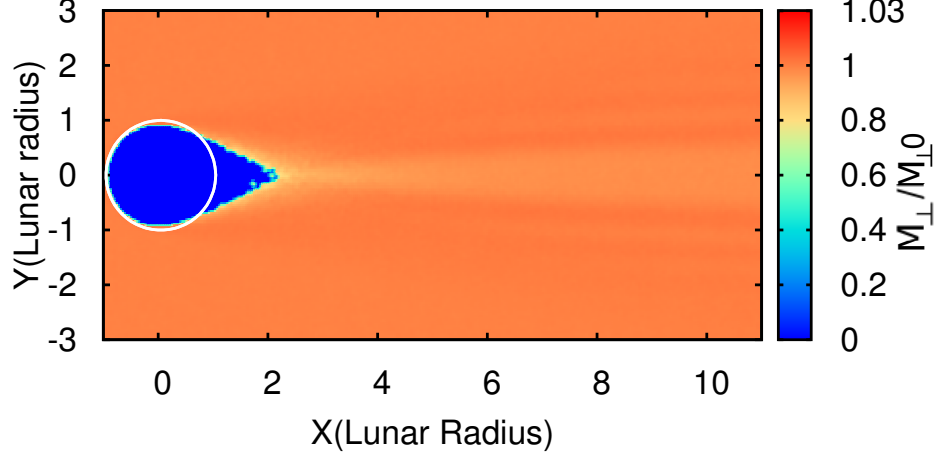


Figure 3.1: Ratio of the perpendicular Mach number to its upstream value  $\frac{M_{\perp}}{M_{0\perp}}$  in the hybrid simulation domain.

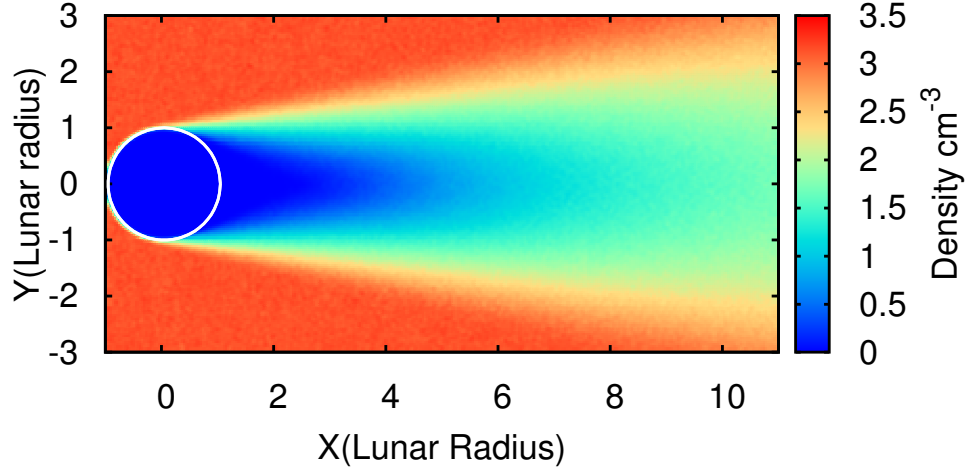


Figure 3.2: Normalized density of the plasma in the hybrid simulation domain.

Fig. 3.1 shows small variations in  $v_{\perp}$  in the wake region. In particular,  $M_{\perp}$  decreased in the immediate downstream region. From Fig. 3.2, however, these variations are seen to occur in the depleted density regions, where statistical errors in  $M_{\perp}$  are large. As discussed in Ch. 2, the perpendicular velocity can be expressed as,

$$\mathbf{V}_{\perp} = - \left[ \frac{m}{Ze} (\mathbf{V} \cdot \nabla \mathbf{V}_{\perp}) \times \frac{\mathbf{B}}{B^2} + \frac{1}{nZe} \nabla_{\perp} P_i \times \frac{\mathbf{B}}{B^2} + \nabla_{\perp} \phi \times \frac{\mathbf{B}}{B^2} \right], \quad (3.11)$$

Where,  $m$ ,  $Z$ ,  $\phi$  and  $e$  are, respectively, the ion mass, the ion charge-number, electric potential, and the electron charge. The first term in this equation is the polarization drift, the second term is known as the diamagnetic drift,

and the last term is the  $\mathbf{E} \times \mathbf{B}$  drifts. The analytic (characteristics) analysis addresses the case where the ion gyroradius (in the background magnetic field  $B_{IMF}$ ) is much smaller than the object, so that the perpendicular plasma flow is strongly constrained [31] and the polarization drift can be neglected. The diamagnetic drift is perpendicular to the magnetic field as well as the perpendicular pressure gradient, so it does not have any component in the plane of  $\mathbf{V}_{SW} - \mathbf{B}$ . Therefore, in this configuration, the only component of the perpendicular velocity (Fig. 3.1) comes from the  $\mathbf{E} \times \mathbf{B}$  drift term. In the hybrid code, to be comparable with the analytic (characteristics) model, the time evolution of the solar wind magnetic field is artificially turned off. As a result, the  $\mathbf{E} \times \mathbf{B}$  drift must be uniform in this simulation because  $\mathbf{B}$  and  $\mathbf{E}_z$  have just their uniform values in the external solar wind which is not constant close to the Moon surface (less than  $3 R_m$ ). In this area, very few particles are present, and statistical errors are more significant. The results of the hybrid model are sensitive to the ad hoc conditions. For example, the hybrid code imposes a density floor; that is, a lower plasma density, for stability reasons and is affected by the number of particles per computational cell. The perpendicular Mach number, assumed to be constant in the model based on the method of characteristics, is found to be closer to being constant, as the density floor is lowered. In the final analysis, injecting  $\sim 15\%$  of incident solar wind ions in the wake region,  $M_{\perp}$  is found to be constant within  $\sim 9\%$  in regions where the density is significant (say, above  $2.8\%$  of the background density or  $X \geq 2.1 R_m$ ). In those regions, the maximum relative difference is of order  $9\%$ , which supports the assumption made in the analytic model that  $M_{\perp}$  is approximately constant. Figure 3.3 shows normalized densities obtained from the hybrid and the method of characteristics as a function of the vertical coordinate  $Y$ , at selected values of  $X$  in the wake region. In both cases, the density is found to be minimum at the center of the wake and increases as expected away from the Moon. Differences in the density profiles obtained with the two models are visible from this figure. Qualitatively, the density profile obtained from the hybrid model is narrower near the minimum, and broader in the wake edge region, than the density obtained with the method

of characteristics. Another difference is that the method of characteristics predicts smooth density profiles, while the ones obtained with the hybrid code show significant levels of short-scale variations, probably associated with waves and turbulence excited in the solar wind - Moon interaction. Quantitatively, the minimum density obtained with the method of characteristics is lower than in the hybrid model. These differences are relatively small and do not exceed 15% of the upstream density, from which I conclude that both models predict density profiles that are in reasonable agreement.

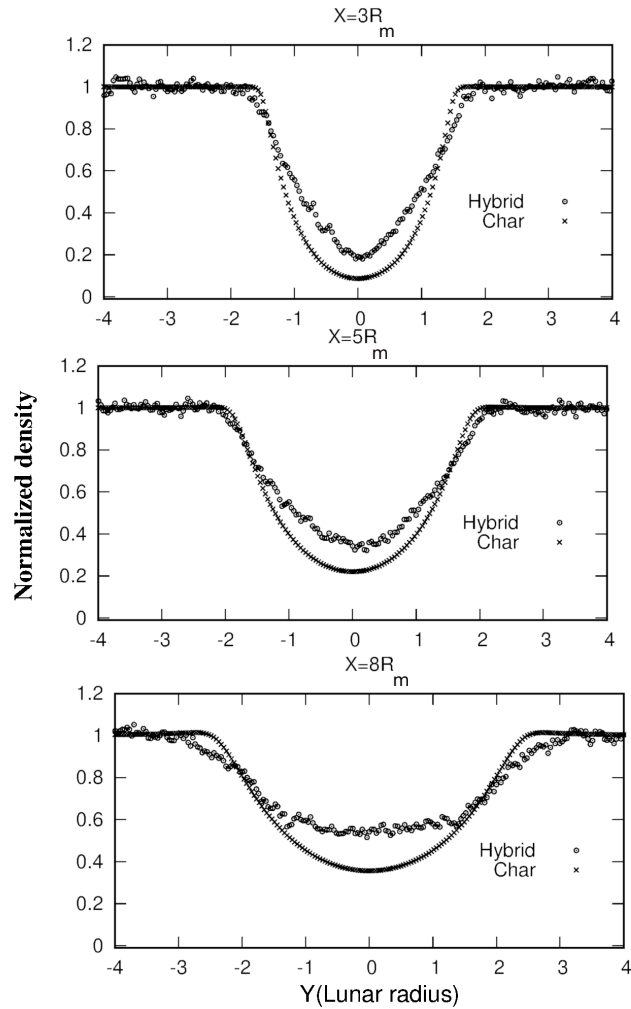


Figure 3.3: Comparison between the Normalized ion density of the hybrid code (circle) and the method of characteristics (cross) along  $Y$  at different cuts in  $X$ . From top to bottom,  $X = 3 R_m$ ,  $X = 5 R_M$  and  $X = 8 R_m$ .

## 3.2 Two-dimensional finite element model

A two-dimensional finite element model is used to solve systems of partial differential equations, whether time-dependent or stationary. The system of partial differential equations which govern plasma dynamics in the wake behind the Moon is nonlinear and cannot be solved analytically. In the finite element code, an arbitrary geometry is divided into a large number of cells where unknown functions are discretized. In this thesis, the computer code TOPO is used to simulate the night-side the Moon-solar wind interactions with finite element discretization on an unstructured triangular mesh. The code TOPO is a general purpose finite element code written by Prof. Richard Marchand [48]. In the paper [48], a detailed explanation of the finite element code (TOPO) is provided, and in this paper this code is used to simulate the plasma passing through the edge of a tokamak [48], [49]. The general equations which govern the transport of plasma and neutral particles can be expressed as,

$$\sum_{l=1}^N \left[ Z_{kl} \frac{\partial U_l}{\partial t} + \nabla \cdot (\mathbf{A}_{kl} U_l) + \nabla \cdot (\mathbf{B}_{kl} \cdot \nabla U_l) + C_{kl} U_l + \mathbf{D}_{kl} \cdot \nabla U_l \right] + S_k = 0 \quad (3.12)$$

Where the summation is over  $N$  coupled partial differential equations. Therefore,  $k$  and  $l$  range from 1 to  $N$ .  $U_l$  is the unknown function with index  $l$ . In addition,  $Z_{kl}$ ,  $\mathbf{A}_{kl}$ ,  $\mathbf{B}_{kl}$ ,  $C_{kl}$  and  $\mathbf{D}_{kl}$  are coupling coefficients, and  $S_k$  represents a source term in equation  $k$ . In order to solve the desired system of equations, an unstructured mesh is required. I used a program which is called ARANEA (written by Marchand et. al [51]), to generate unstructured triangular meshes. ARANEA is written in JAVA, with a full Graphics User Interface to generate unstructured triangular meshes on two-dimensional domains. The interested reader should refer to article [51] for more details. In order to download the program, refer to the CPC Program Library under catalog identifier:

[HTTP://cpc.cs.qub.ac.uk/summaries/ADOG](http://cpc.cs.qub.ac.uk/summaries/ADOG).

In the next section 3.2.1, TOPO is modified for simulating a normal shock, which has an analytic solution to assess the accuracy of the code. Then, in Sec. 3.2.2, the equations related to the interaction of plasma fluid with the

Moon are implemented in the code along with the proper boundary conditions to simulate the lunar wake.

### 3.2.1 Finite element code validation

Shock waves are formed when a flowing fluid moving at supersonic speed, encounters an obstacle. The speed of the fluid has an important role in forming shock fronts. If the speed of the plasma flow is much less than the speed of sound of the plasma, plasma density does not change discontinuously. When the speed of the plasma reaches the sound speed, compressibility effects are important, and shock waves appear [60]. In other words, discontinuities can occur during the motion of a compressible fluid which flows faster than the speed of sound [15], [57] and [80]. If the shock wave is perpendicular or inclined to the flow direction, it is called a normal or an oblique shock respectively. As an illustration, I consider a standard two-dimensional problem in gas-dynamics involving the flow of a supersonic compressible fluid in the absence of a magnetic field encountering a rigid wedge, thus forming an oblique shock. Figure 3.4 shows a rigid wedge with an angle  $\theta$  with respect to horizon ( $x - axis$ ). The discontinuities in the density, velocity, and pressure across the shock front can be determined from the:

- (i) mass conservation equation,
- (ii) momentum conservation equation, and
- (iii) ideal gas approximation [15].

In this example, fluid with mass density  $\rho_1 = n_1 m$  flows at supersonic speed with an upstream Mach number  $M_1 = V_1/C_s$ , and encounters a wedge. In the definition of the Mach number,  $C_s = \sqrt{kT/m}$ , where  $T$  is the temperature of the upstream fluid and  $m$  is the mass of a particle. The shock front exists with an angle  $\beta$  with respect to the  $X - axis$  and unlike normal shock waves which are always perpendicular to the flow velocity before and after the shock, the oblique shock waves are deflected upward downstream of the wedge as shown in Fig. 3.4. The conservation laws, along with the equations of state across the shock front, are applied to get a formula relating the Mach numbers of

the flow upstream  $M_1$ , and downstream  $M_2$ , the wedge (deflection angle)  $\theta$ , and, the shock wave angle  $\beta$ . The partial differential form of continuity and momentum equations are as below,

-Continuity,

$$\frac{\partial \rho}{\partial t} + \nabla \cdot (\rho \mathbf{V}) = 0, \quad (3.13)$$

-Momentum,

$$\frac{\partial (\rho \mathbf{V})}{\partial t} + \nabla \cdot (\rho \mathbf{V} \mathbf{V} + \overline{\overline{\mathbf{P}}}) = 0, \quad (3.14)$$

where,  $\rho = nm$  is the mass density of the fluid,  $\mathbf{V}$  is the velocity of the fluid and  $\overline{\overline{\mathbf{P}}} = pI$  is the isotropic stress tensor [35], [43]. Now, I consider a 2D surface with area  $A$  in which neutral fluid flows across it. Assuming a stationary state the first terms  $\frac{\partial}{\partial t}$ , in Eqs. 3.13 and 3.14 can be ignored. The steady state, volume integral conservation equations can be expressed as,

-Continuity,

$$\oiint nm \mathbf{V} \cdot \hat{n} dA = 0, \quad (3.15)$$

-Momentum,

$$\oiint nm \mathbf{V} (\mathbf{V} \cdot \hat{n}) dA = - \oiint \mathbf{P} \cdot \hat{n} dA, \quad (3.16)$$

where  $\mathbf{P}$  is the pressure of particles flowing through the shock front with area  $A$ . Unit vectors parallel and perpendicular to the shock front are,  $\hat{t}$  and  $\hat{n}$  respectively. In the upstream/downstream regions the velocities have two components parallel/tangential (with subscript  $t$ ) and perpendicular/normal (with subscript  $n$ ) to the shock front. The continuity equation 3.15 gives a condition on the normal component of the velocities (Mach numbers),

$$n_1 M_{n1} = n_2 M_{n2}, \quad (3.17)$$

$M_{n1}$  and  $M_{n2}$  are the components of Mach numbers (normalized velocities) normal to the shock in the upstream and downstream regions respectively. Densities before and after shocks are  $n_1$  and  $n_2$ .

The momentum equation 3.16 is a vector equation. By considering the tangential component of the normalized momentum conservation and using Eq. 3.17 it follows that the tangential component of the flow velocity does not change across an oblique shock

$$M_{t1} = M_{t2}. \quad (3.18)$$

The ideal gas approximation,  $p = nkT$  is assumed, so that the normal component of the momentum equation 3.16 gives,

$$n_1 + n_1 M_{n1}^2 = n_2 + n_2 M_{n2}^2. \quad (3.19)$$

This gives three equations 3.17-3.19 from which three unknowns  $n_2, M_{n2}$  and  $M_{t2}$  can be determined. According to Fig 3.4 the projections of the Mach

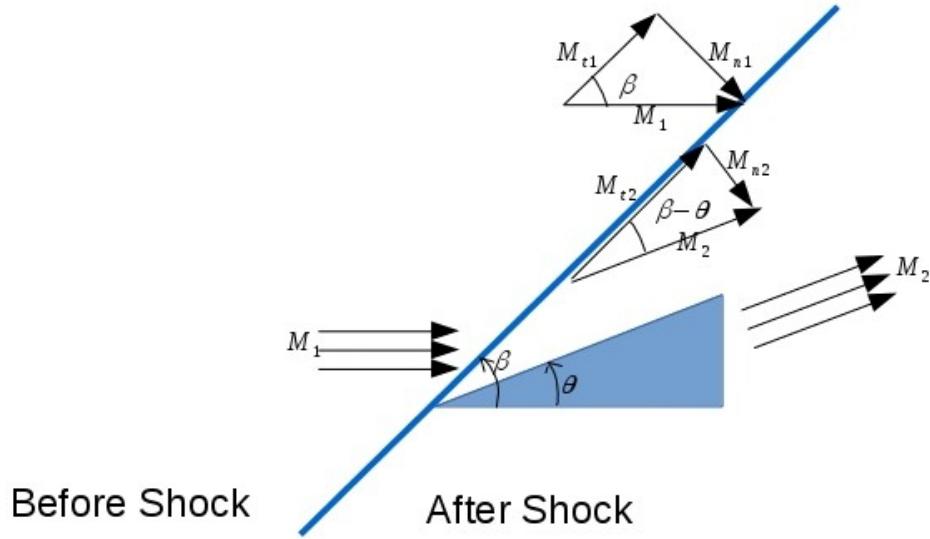


Figure 3.4: Oblique shock illustration.

numbers along the shock are

$$\begin{aligned} M_{t1} &= M_1 \cos(\beta), \\ M_{t2} &= M_2 \cos(\beta - \theta). \end{aligned} \quad (3.20)$$

Similarly the normal components of the Mach numbers are

$$\begin{aligned} M_{n1} &= M_1 \sin(\beta), \\ M_{n2} &= M_2 \sin(\beta - \theta). \end{aligned} \quad (3.21)$$

Referring to the geometry of the oblique shock shown in Fig. 3.4 and applying Eqs. 3.20-3.21, give

$$\begin{aligned}\tan(\beta) &= \frac{M_{n1}}{M_{t1}}, \\ \tan(\beta - \theta) &= \frac{M_{n2}}{M_{t2}}, \\ \frac{\tan(\beta)}{\tan(\beta - \theta)} &= \frac{n_2}{n_1} = \frac{M_{n1}}{M_{n2}}.\end{aligned}\tag{3.22}$$

Equation 3.17 is substituted in Eq. 3.19 to give

$$-M_{n1} [M_{n2}^2] + (1 + M_{n1}^2) [M_{n2}] - M_{n1} = 0.\tag{3.23}$$

The solutions to this quadratic equation are,  $M_{n2} = 1/M_{n1}$  and  $M_{n2} = M_{n1}$  of which only the first is physically acceptable (the second one gives no shock). This gives the formula relating the unknown shock wave angle,  $\beta$ , to the known variables such as the wedge angle (deflection angle) and the upstream Mach number (see the references [36], [17] and [71])

$$\tan(\beta - \theta) - \frac{2}{M_1^2 \sin(2\beta)} = 0.\tag{3.24}$$

Equation 3.24 can be solved straightforwardly using a root finder, thus giving shock wave angles for given wedge angles.

To validate the finite element code, the differential form of equations 3.15 and 3.16 are also solved with the TOPO. Two meshes with different wedge angle ( $\theta_1 \sim 15^\circ, \theta_2 \sim 20^\circ$ ) are generated with ARANEA. Two different flow velocities ( $M_{1,1} = 2, M_{1,2} = 4$ ) encountering these obstacles are considered. Simulations are carried out until a steady state is reached then the shock wave angle can be determined. The shock wave angles which are computed from the finite element code are compared with the analytic results in table 3.2.

The shock angles obtained analytically are seen to be in good agreement with computed values obtained with the finite element code as shown in the Table 3.2. Quantitatively, the accuracy ranges from  $\simeq 1\%$  to  $\simeq 4\%$  in the range of parameters considered. The table shows that when the upstream Mach number is smaller the discrepancy is less for the two wedge angles considered. Obviously, in numerical methods and computational simulations there

	Analytic	FEM	Percentage discrepancy
$M_1 = 2, \theta = 14.9^\circ$	$\beta = 41.62^\circ$	$\beta = 40.91^\circ$	1.7
$M_1 = 4, \theta = 14.9^\circ$	$\beta = 24.34^\circ$	$\beta = 23.74^\circ$	2.4
$M_1 = 2, \theta = 19.9^\circ$	$\beta = 46.58^\circ$	$\beta = 45.98^\circ$	1.2
$M_1 = 4, \theta = 19.9^\circ$	$\beta = 28.46^\circ$	$\beta = 27.32^\circ$	4.0

Table 3.2: The comparisons between computed shock angle analytically and via the Finite Element Model (FEM). It has computed for different upstream Mach numbers and two different wedge angles.

are always approximations which can cause discrepancies between results obtained with different models. One of the sources of numerical errors in the numerical solution of PDE's comes from the finite spatial distretization used in the finite elements. In conclusion, the good qualitative agreement between the two indicates that the finite element code is reliable and can be used to simulate the lunar wake.

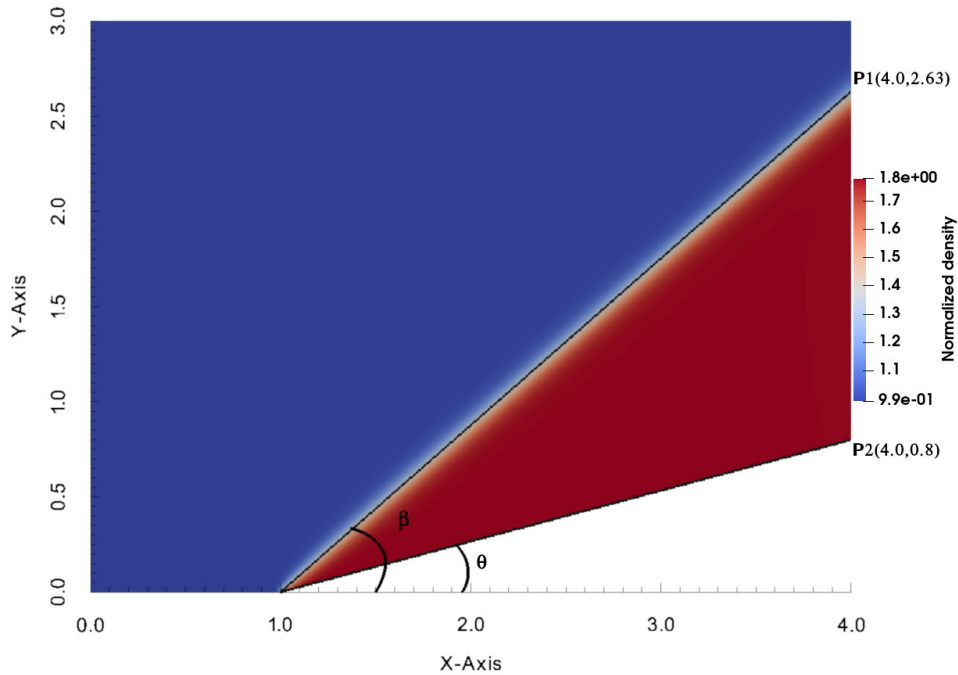


Figure 3.5: Computed oblique shock with the finite element code. The Mach number is 2 and the wedge angle is  $\theta = 14.9^\circ$ .

### 3.2.2 Use of the finite element code for the lunar wake case

In this section, the equations governing the dynamics of the quasi-neutral, isothermal fluids refilling the lunar wake are solved using the Finite Element Code (TOPO). In the absence of any interaction processes to create ions, the ion number density  $n_i$  is conserved during the motion of the fluid, which is described by the continuity equation 3.13:

$$\frac{\partial n_i}{\partial t} + \nabla \cdot (n_i \mathbf{V}_i) = 0. \quad (3.25)$$

The momentum conservation equation 3.14 connects the fluid velocity  $\mathbf{V}_i$  to density and electromagnetic forces acting on the fluid element [2]. I adopt the simplest possible fluid closure scheme, that the ion temperature,  $T_i$ , is invariant, so that the pressure is simply proportional to density [33],

$$\frac{\partial (n_i \mathbf{V}_i)}{\partial t} + \nabla \cdot (n_i \mathbf{V}_i \mathbf{V}_i) + \frac{T_i}{m_i} \nabla n_i - \frac{en_i Z}{m_i} (\mathbf{E} + \mathbf{V}_i \times \mathbf{B}) = 0. \quad (3.26)$$

In this expression,  $m_i$ ,  $n_i$ ,  $Z$ , and  $e$  are, respectively, the ion mass, the ion number density, the ion charge-number and the electron charge.  $\mathbf{E}$  and  $\mathbf{B}$  are the electric and magnetic fields. The assumptions made in the method of characteristics are also applied in the finite element code:

1. the perpendicular component of the velocity is constant,
2. the magnetic field is constant,
3. plasma is quasi-neutral.

An arbitrary angle  $\alpha$  between the interplanetary magnetic field  $\mathbf{B}$  and the flow velocity in the solar wind is considered. The  $X$  and  $Y$  components of the ion normalized velocity (Mach numbers) are

$$\begin{aligned} M_x &= M_{\parallel} \cos(\alpha) + M_{\perp} \sin(\alpha), \\ M_y &= M_{\parallel} \sin(\alpha) - M_{\perp} \cos(\alpha). \end{aligned} \quad (3.27)$$

Where the perpendicular Mach number,  $M_{\perp} = M_{sw} \sin(\alpha)$ , is considered as a constant in the calculations (see Fig. 3.6). Now, the normalized continuity

equation 3.25 becomes,

$$\frac{\partial n}{\partial t} + \nabla \cdot [n (M_{\parallel} \cos(\alpha) + M_{sw} \sin(\alpha)^2) \hat{x} + n (M_{\parallel} \sin(\alpha) - M_{sw} \sin(\alpha) \cos(\alpha)) \hat{y}] = 0. \quad (3.28)$$

The ion density is normalized to the density of the solar wind  $n = \frac{n_i}{n_{sw}}$  and velocities are normalized to the sound speed of the plasma. As the perpendicular velocity is assumed to be invariant, the parallel momentum of ions is responsible for the dynamics of the fluids in the plane of  $\mathbf{B} - \mathbf{V}_{sw}$ ,

$$n_i \frac{\partial \mathbf{V}_{\parallel}}{\partial t} + (n_i \mathbf{V} \cdot \nabla) \mathbf{V}_{\parallel} = -\frac{T_i}{m_i} \nabla_{\parallel} (n_i) + \frac{en_i Z}{m_i} \mathbf{E}_{\parallel}. \quad (3.29)$$

As the Debye length is much smaller than any length scale in the problem ( $n_e = Zn_i$ ), the plasma is assumed to be quasi-neutral and the electron parallel momentum equation gives the adiabatic relation between the electric field and the parallel pressure gradients,

$$E_{\parallel} = -\frac{T_e}{en_i} \nabla_{\parallel} (n_i). \quad (3.30)$$

Now, by applying Eq. 3.30 into the Eq. 3.29, the normalized parallel momentum equation in  $x - y$  coordinates becomes

$$\begin{aligned} n \frac{\partial M_{\parallel}}{\partial t} &+ n [M_{\parallel} \cos(\alpha) + M_{sw} \sin(\alpha)^2] \frac{\partial M_{\parallel}}{\partial x} \\ &+ n [M_{\parallel} \sin(\alpha) - M_{sw} \sin(\alpha) \cos(\alpha)] \frac{\partial M_{\parallel}}{\partial y} \\ &= - \left( \cos(\alpha) \frac{\partial n}{\partial x} + \sin(\alpha) \frac{\partial n}{\partial y} \right). \end{aligned} \quad (3.31)$$

In order to stabilize the simulations diffusion terms  $-D\nabla^2 n_i$ ,  $-D\nabla^2 \mathbf{V}_i$  are added to the continuity and the momentum equations 3.25, 3.31, where  $D$  is a constant diffusion coefficient related to fluid viscosity in these equations. This is needed because with this finite element code, discretization of the convection equations generates a small negative diffusion. A small artificial positive diffusion is therefore needed in order to ensure numerical stability. All of the coupling coefficients in the Eq. 3.12 can now be inserted in TOPO code along with the proper boundary conditions to do the simulations. The TOPO is capable of solving the fluid equations for multiple species. Effects from two

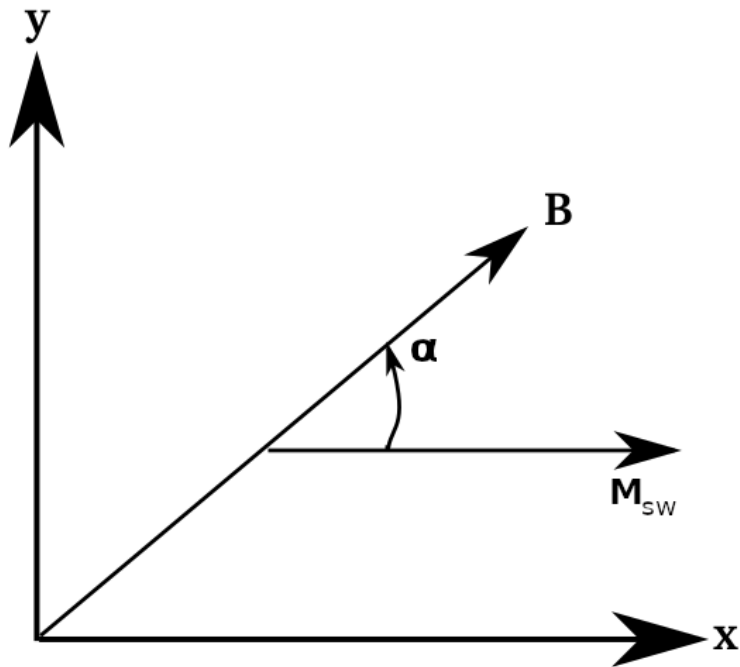


Figure 3.6: This figure shows the orientation of the interplanetary magnetic field  $\mathbf{B}$  and velocity (Mach number) in the solar wind  $M_{sw}$  in the  $x - y$  coordinate system.

ion fluids coming from either side of the Moon cross section in this 2D model are accounted for, labeling them with subscripts 1 and 2, corresponding to plasma entering from below and above, respectively as discussed in Ch. 2. Therefore, Eqs. 3.25, 3.31 are considered for each species which are characterized by a density  $n_{1,2}$  and a parallel Mach number  $M_{1,2\parallel}$ . The four equations (two continuity equations and two momentum equations corresponding to each ion fluid) are then solved simultaneously for the two-fluid system. The interaction between fluids 1 and 2 is included in the momentum equations of each species in the finite element code and the strength of this interaction can be varied arbitrarily as in the solutions obtained with the method of characteristics, in order to assess its impact on the results. Another interesting test which can be done with TOPO, which consists of running the code with the same configurations but for a single-ion fluid and to only solve its continuity and momentum equation. In order to do these simulations, an unstructured mesh on a two-dimensional domain is generated with ARANEA (see Fig. 3.7). In this 2D code the solar wind flow  $V_{sw} = 295.6\text{km/s}$  is in the  $+x$  direction, and the solar wind magnetic field  $\mathbf{B}_{\text{IMF}}$  is in the  $+y$  direction ( $\alpha = 90^\circ$ ) with a magnitude of  $6\text{nT}$ . The background density is assumed to be  $n_{sw} = 3.14\text{cm}^{-3}$ , the electron and ion temperatures are  $T_e \simeq 14.3\text{eV}$  and  $T_i \simeq 5.7\text{eV}$ . In that case, with the parameters given above, the sound speed is  $c_s \sim 48.8\text{km/s}$  and the corresponding upstream Mach number is  $M_\perp \simeq 6$  and  $M_\parallel = 0$ . These parameters correspond to those from the first flyby of ARTEMIS P1 through the lunar wake [18], [68], [75]. The element size and time step are set to be  $\delta = 0.038 R_m$  and  $\Delta = 0.001$  respectively. With these parameters, the simulation domain used in the finite element simulations extends up to  $+10 R_m$  in  $X$  and  $\pm 3 R_m$  in  $Y$ , where  $R_M \sim 1737\text{km}$ . The diffusion coefficient is set to be  $D = 0.02$  and simulations are carried out until a steady state is reached. Below the results from the finite element code for three possible cases are presented in figures 3.8, 3.9 and 3.10:

- Case 1- Two-fluid with coupling between the two ion fluids(RHS=1),
- Case 2- Two-fluid without coupling between the two ion fluids (RHS=0),

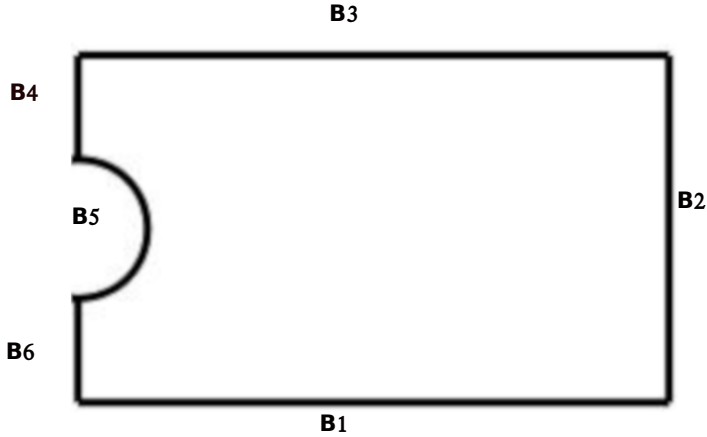


Figure 3.7: The two-dimensional domain of the lunar wake is used in ARANEA to generate an unstructured mesh for the finite element (TOPO) code.

- Case 3- Single-fluid.

In the third case, there is only one fluid, the up-down symmetry yields zero parallel flow velocity on the wake axis ( $Y = 0$ ). This constraint prevents plasma coming from below, to reach regions of the wake above  $Y = 0$ , and vice versa. In the second case where there are two fluids without coupling, there is no force to stop either fluid from going beyond the  $Y = 0$  axis. In this case, parallel velocities for each fluid can become large in absolute value, which explains the shorter region with practically zero density, compared with the other two cases shown in Fig. 3.8. In this analysis the electric field is proportional to parallel component of the gradient in logarithm of density. By comparing the first two cases, it is obvious that the electric field is smaller for the interacting fluids than for the non interacting fluids. In case 1, the electric field is the sum over the parallel pressure gradient of the two fluids that are equal and in opposite directions. Therefore, in the first case, the interactions between the two fluids reduce the flow of plasma entering the wake from below, above the  $Y = 0$  axis, and vice versa. This reduction is clearly seen in Figs. 3.8 and 3.9. As a result, in the second case as there is no constraint on the movement of ion fluid, the void region is the shortest in comparison to the other two cases where a force prevents fluids from reaching the opposite sides.

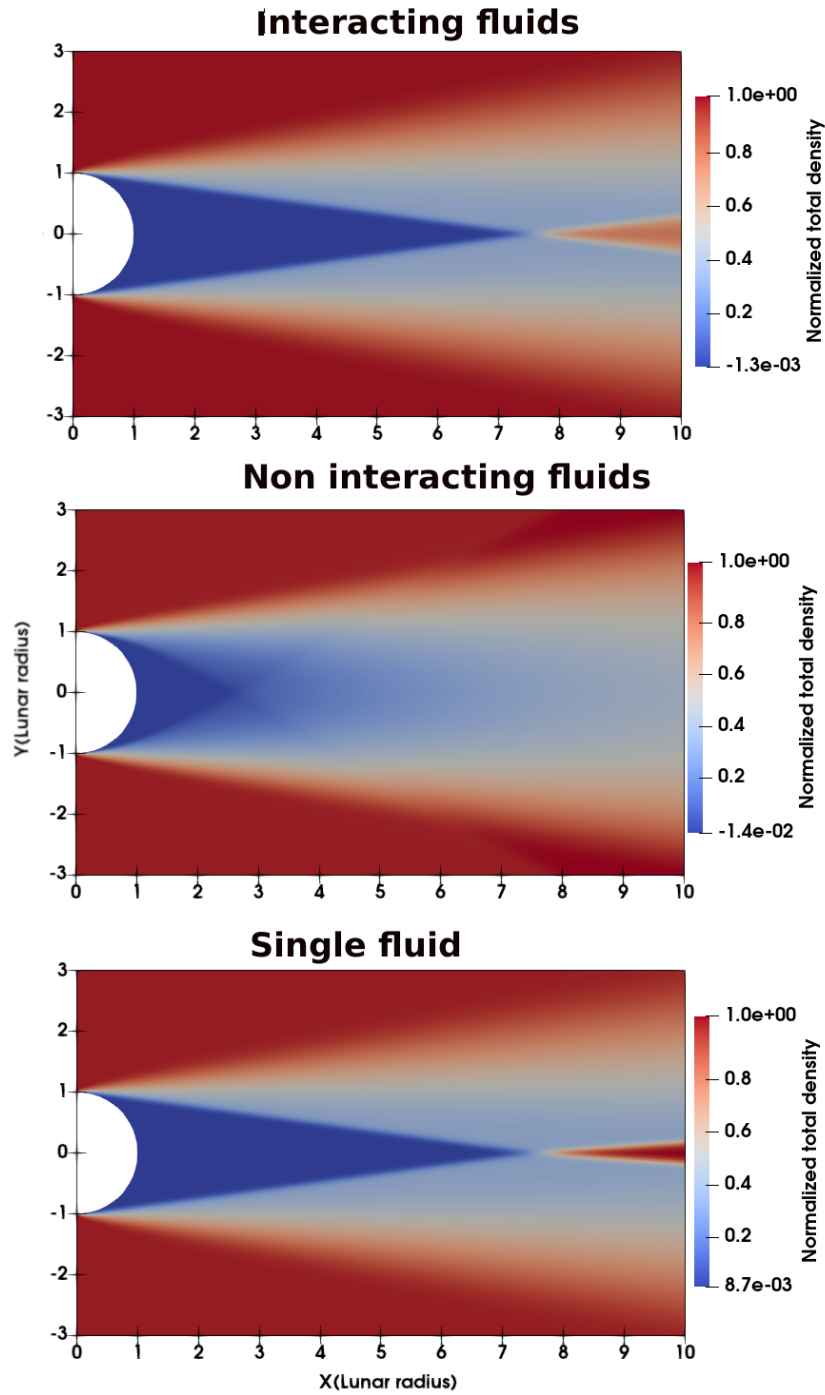


Figure 3.8: Normalized total density from the finite element code for three different cases. From top to bottom, 1- the interaction between the two fluids are considered, 2- interaction between the two fluids is ignored, and 3- a single-fluid is assumed in the simulation.

Comparing the single-fluid case and the two-fluid case with interactions (case 3 and case 1), it is obvious that when ions fill the wake far from the Moon, the normalized density of the single-fluid has a higher value in comparison to the two-fluid case. In the single-fluid approximation, the parallel fluid velocity must vanish at  $Y = 0$  by symmetry. As a result, plasma stops flowing along the vertical direction there, which explains the larger density resulting from an accumulation in density on the axis. In case 3, the density gradient of one fluid opposes, and decreases the parallel velocity of the other one. This is why plasma flow from below can reach the region above the  $Y = 0$  axis and vice versa, but less than when the fluids are not interacting. The parallel Mach number calculated with the finite element code for three different cases are plotted in Fig. 3.9. The upper/middle panel shows  $M_{1\parallel}$  calculated with the finite element model (FEM) for the interacting/non-interacting fluid tests. The bottom panel demonstrates the parallel Mach number of the plasma fluid for the single-fluid test. In order to understand the physics behind the three cases, I consider the  $M_{1\parallel}$  for comparisons. In the non-interacting case (the middle panel), plasma can accelerate upward parallel to the magnetic field to have large parallel velocity (170.87 km/s) because there are no forces opposing either fluid. In the other cases (single-fluid/interacting two-fluid as shown in the bottom/top panel) plasma is prevented from reaching the opposite side of the wake, and the maximum parallel velocity becomes 39.0 km/s. Normalized parallel flux  $\Gamma_{1,2\parallel} = (n_{1,2}M_{1,2\parallel})/n_{SW}$ , where  $n_{SW}$  is the upstream solar wind density and the net normalized flux  $\Gamma = \Gamma_{1\parallel} + \Gamma_{2\parallel}$  is calculated with the finite element code and shown in Fig 3.10. The parallel flux of the plasma moving up into the wake region of the Moon is shown in the top/middle panel when the interactions between the two fluids are/are not considered. The bottom panel shows the normalized parallel flux of the single-fluid plasma. As it is discussed, when the interaction between the two fluids is turned off (middle panel), plasma can reach the opposite side of the wake. In other words, there are some positive fluxes far from the Moon ( $X > 6.5 R_m$ ) and close to the upper boundary ( $Y > 2 R_m$ ) and conversely some negative fluxes close to the lower boundary. In the two-fluid cases since  $\alpha = 90$ , there is symmetry between

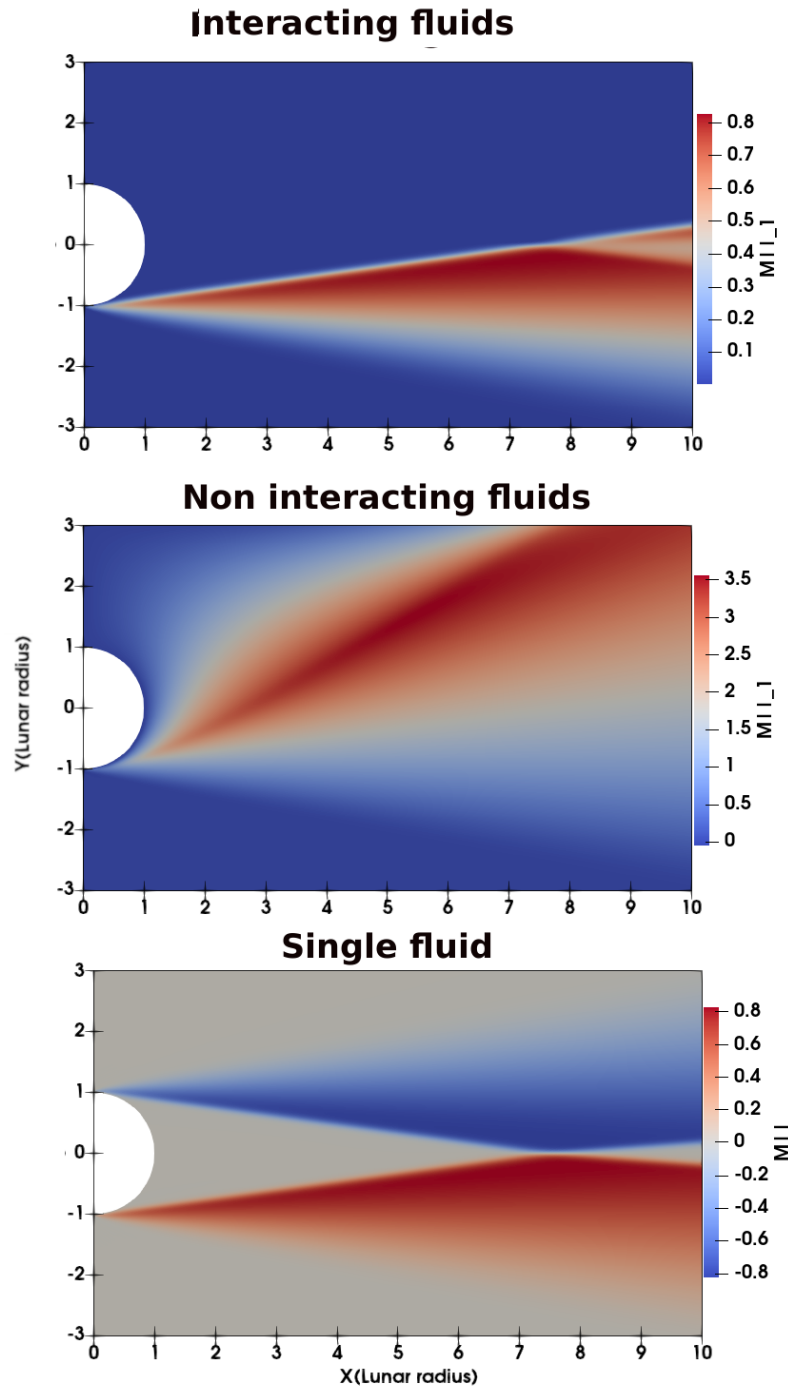


Figure 3.9: Parallel Mach number calculated with the finite element code for three different cases. Calculated parallel Mach number of the plasma moving up into the Moon intersection is shown in the top/middle panel when the interactions between the two ion fluids are/are not considered. The bottom panel shows the parallel normalized velocity of the single-fluid plasma calculated with the finite element code.

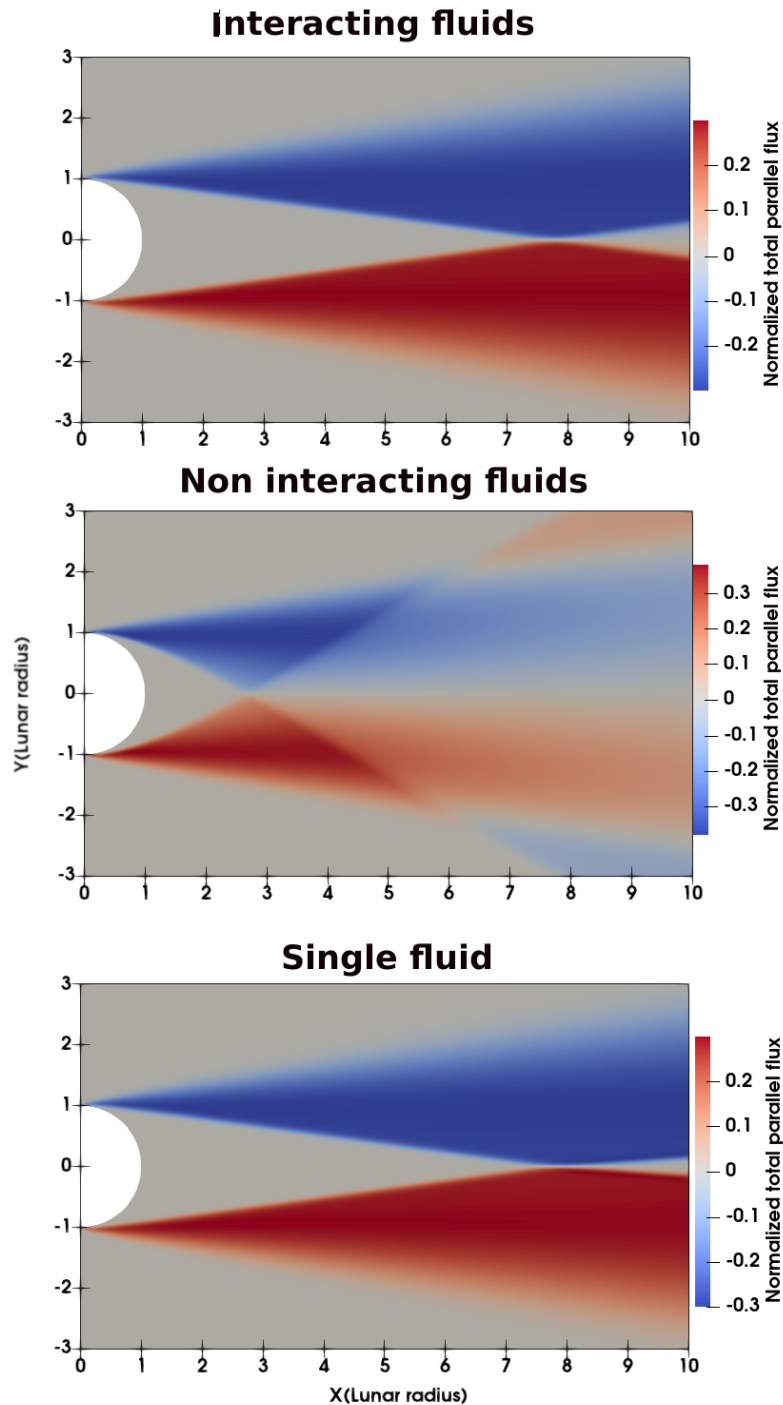


Figure 3.10: Normalized total parallel flux calculated with the finite element code for three different cases. The calculated parallel flux of the plasma moving up into the Moon intersection is shown in the top/middle panel when the interactions between the two ion fluids are/are not considered. The bottom panel shows the normalized parallel flux of the single-fluid plasma.

the two counterstreaming particle fluxes, and precisely in the middle of the wake at  $Y = 0$  the two fluxes are equal with opposite signs. There they cancel each other, and the net flux is zero. However, in the single-fluid simulation, the unique flux is exactly zero on the  $X - axis$ , and it is positive/negative below/above the  $Y$  axis. The main differences in the net parallel flux of the top and the bottom panel happen in the light shadow region, which is wider for the two-fluid, interacting rather than the one-fluid model. The zero net parallel flux in the light shadow region of the single-fluid model comes from the zero parallel Mach number, in contrast to the two-fluid models for which the positive and negative fluxes cancel each other at  $Y = 0$ .

### 3.2.3 Comparisons between results obtained with the finite element model and the method of characteristics

Table 3.3: Main similarities and differences between the method of characteristics and the finite element code

	Characteristics	Finite Element
Similarities	2D	
	Isothermal fluid electrons	
	Uniform $\mathbf{B}$	
	$M_{\perp}$ constant	
	Magnetized fluid ions	
Differences	Boundary conditions	
	Stationary	Time dependent

Figure 3.11 shows the normalized density obtained from the method of characteristics compared with the one from the finite element model (the interacting two-fluid case) along  $Y$ , at three values of  $X$  in the wake region. The density profile of the two models is seen to be minimum on axis at  $Y = 0$  and to increase gradually from both sides along the  $Y - axis$ . Qualitatively, the density profile obtained from the finite element model is narrower near the minimum, and broader in the wake edge region, than the density obtained with the method of characteristics. In addition, the finite element model creates a deeper void and shorter wake compared to what is obtained with the method

of characteristics. This is because in the method of characteristics the parallel velocities can get large numbers in absolute value (Fig. 2.9) while the parallel Mach in the finite element code is much smaller (Fig. 3.9). Another difference between the two models is found at  $X = 8 R_m$  where the finite element shows an increase in density on axis, absent with the method of characteristics. That is related to another feature expected for the solar wind interaction with the Moon, which is pointed out by Michel [53], [54] and is modeled by a 1D hybrid code for the first time by Israelevich and Ofman [34]. It is shown that a standing shock wave appears at  $\sim 7 R_m$  in the wake region. This feature of the wake appears in the results of the finite element simulations while it is not seen with the method of characteristics. In fact, in the finite element code, the supersonic flowing solar wind is imposed on the day-side of the Moon as the boundary condition and right after the solar wind fluid passes the Moon, a sharp decrease in the density appears on the night-side. This is what causes the shock fronts converging to the  $Y = 0$  axis. However, in the method of characteristics, the boundary started at around  $X = 2R_m$  which comes from the analytic model and the discontinuity does not appear in this analysis so the shock waves cannot be seen. The differences and similarities between the finite element model and the method of characteristics are listed in Table 3.3.

### 3.3 Comparisons between the densities obtained from the method of characteristics, the finite element model, and the hybrid model

Results from two different simulation models of the lunar wake, namely the finite element and hybrid models reveal some characteristic features of the Moon-solar wind interaction; both were compared with the method of characteristics. The differences and similarities were discussed. In this section, comparisons between the density of all three models, based on the hybrid code, the finite element approach, and the method of characteristics are presented and discussed. The parameters used to run the two codes are the same as the ones used in sections 3.1.1, and 3.2.2. In order to have a better appreciation of the results, normalized ion density of the two models is plotted along the vertical coordinate  $Y$  at four different  $X$  in the vacuum region in Figs. 3.12 and 3.13. In both cases, the density is found to be minimum at the center of the wake and it increases as expected away from the Moon. Qualitatively, the density profile obtained from the finite element model is deeper than the density obtained from the hybrid code because of this ad hoc assumption considered in the hybrid code. Specifically, in order for the hybrid simulations to be numerically stable, particles are injected into the wake from the night-side of the Moon, and this makes a wake with higher density in comparison with the other models which do not have this ad hoc assumption. This explains why the minimum density obtained from the hybrid code close to the Moon,  $X = 3 R_m$ , is  $\sim 0.19n_{Sw}$  which is higher than that obtained with the finite element model  $\sim 10^{-11}n_{Sw}$ . Further from the lunar surface,  $X = 7 R_m$ , these differences are relatively small and do not exceed 5% of the upstream density, from which I conclude that both models predict density profiles that are in relatively good agreement in the far wake region. Another difference is that the finite element code predicts smooth density profiles, while the ones obtained with the hybrid code show significant levels of short-scale variations, probably associated with waves and turbulence excited in the Moon-solar wind interaction. The bottom panel in the Fig. 3.13 shows an increase in normalized

density in the finite element model in the light shadow of the wake which is the result of the converging shock fronts as seen in Fig. 3.11 in this model while it is not seen in the hybrid code [34], [53] and, [54]. This peak corresponds to accumulation of plasma on the Y-axis at the end of the wake (it can also be seen from Fig. 3.10). A summary of the main similarities and differences between the finite element code and the hybrid model is given in Table 3.4

Table 3.4: Main similarities and differences between the finite element model and the hybrid models

	Finite Element	Hybrid
Similarities	2D cylindrical	
	Time dependent	
	isothermal fluid electrons	
Differences	magnetized fluid ions	kinetic ions
	uniform and constant $\mathbf{B}$	solves for $\mathbf{E}$ and $\mathbf{B}$ (optionally)
	$M_{\perp}$ constant	$M_{\perp}$ variable

The normalized densities in all approaches considered are plotted as a function of  $Y$  at various cuts in  $X$  in Fig. 3.14. In all cases, the shape of the wake is similar that the density has a minimum at the center of the wake and gets larger away from the  $Y = 0$  axis on both sides. Qualitatively, the density calculated from the hybrid code at the wake center is more significant compared to the other analyses. As discussed above some ions are injected in the wake on the night-side of the Moon to make the hybrid code stable numerically, so it causes higher number density in the hybrid code than in other models. One of the features of the Moon-solar wind interaction is the formation of shock waves behind the lunar surface [34], [53], [54] which is only captured in the finite element code results. The reason could be due to the ad hoc assumptions made in the hybrid code. For example, injection of some solar wind particles to the wake region for stability reasons. In the final analysis, all the models can present some features of the lunar wake. In order to further assess the two-fluid models including the method of characteristics and the finite element model with coupling for the Moon-solar wind interactions, they are compared with two ARTEMIS satellite observations in Ch. 5.

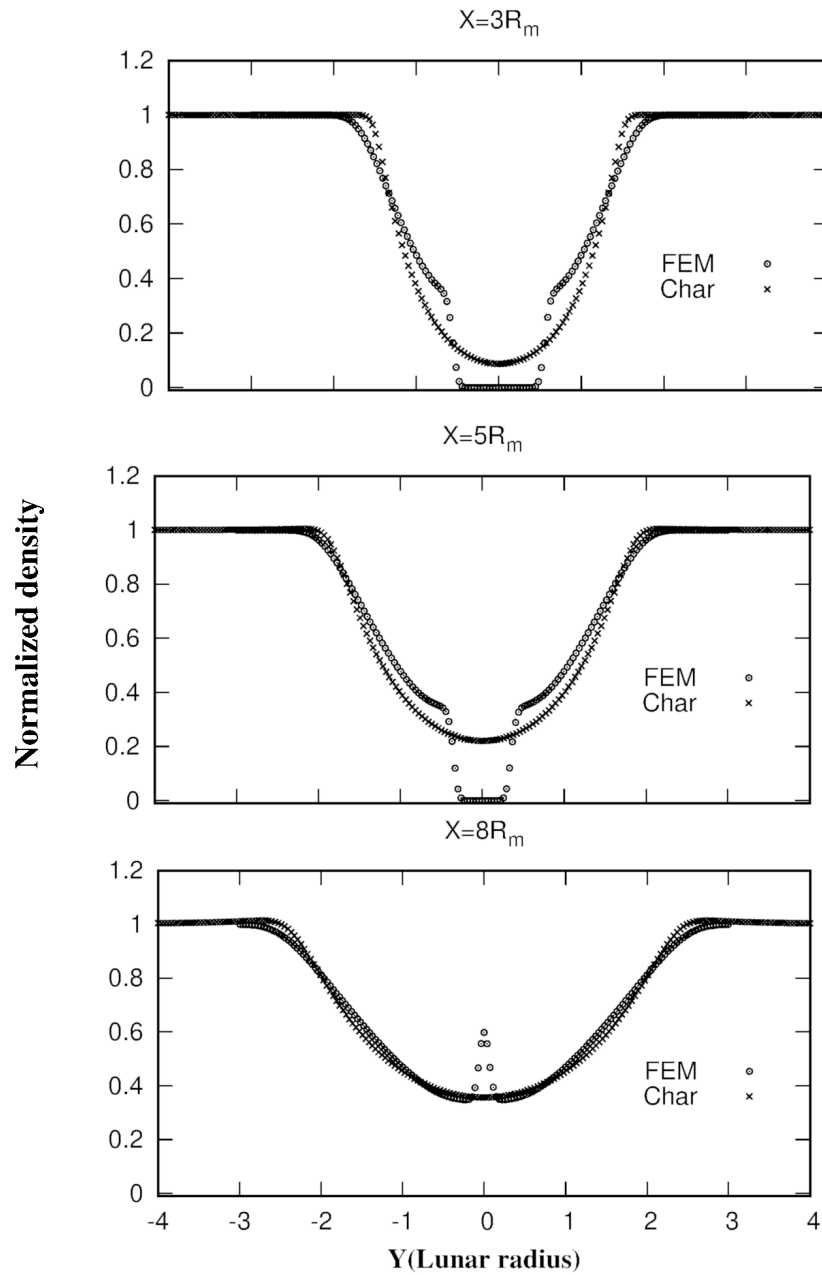


Figure 3.11: Comparison between the Normalized ion density calculated with the two-fluid interacting finite element model (circle) and the method of characteristics (cross) along  $Y$  at different cuts in  $X$ . From top to bottom,  $X = 3 R_m$ ,  $X = 5 R_m$  and  $X = 8 R_m$ .

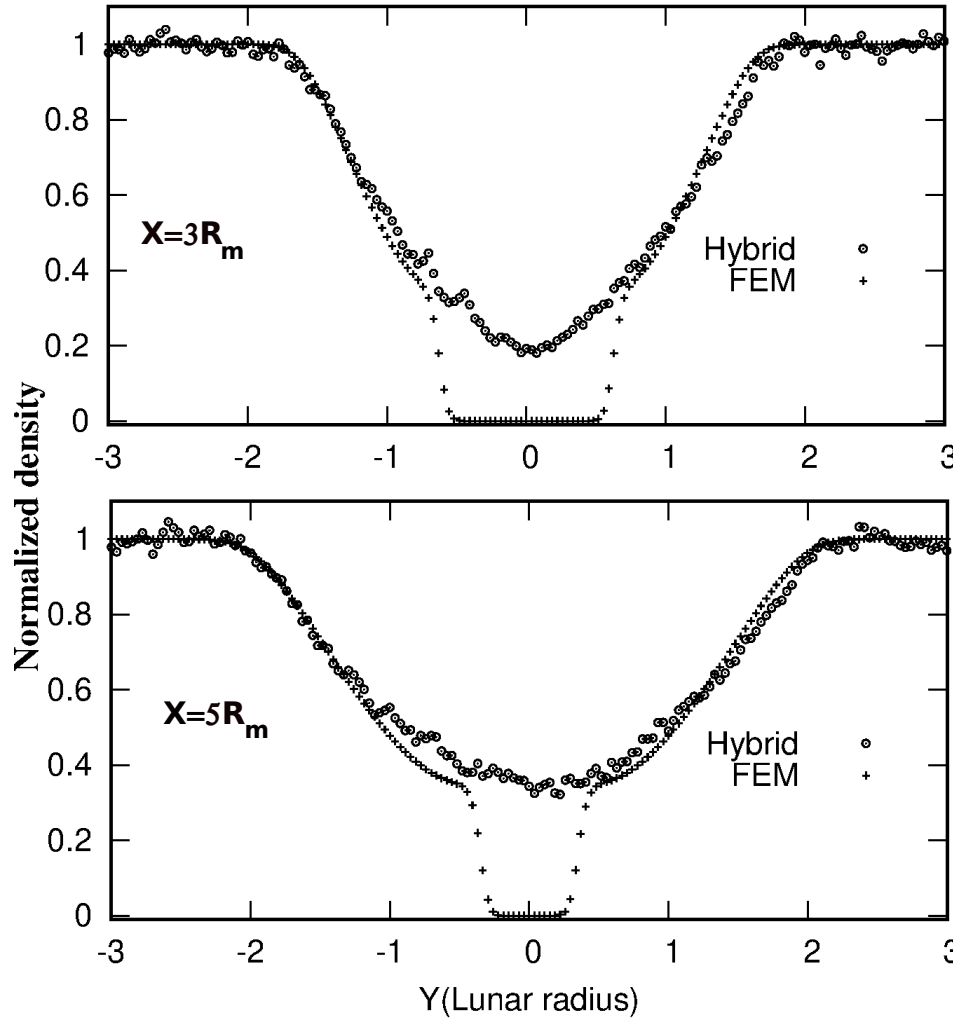


Figure 3.12: Normalized total density calculated with the finite element model (FEM) compared with the results of the hybrid code along  $Y$  at different cuts in  $X$ . From top to bottom,  $X = 3R_M$  and  $X = 5 R_m$ .

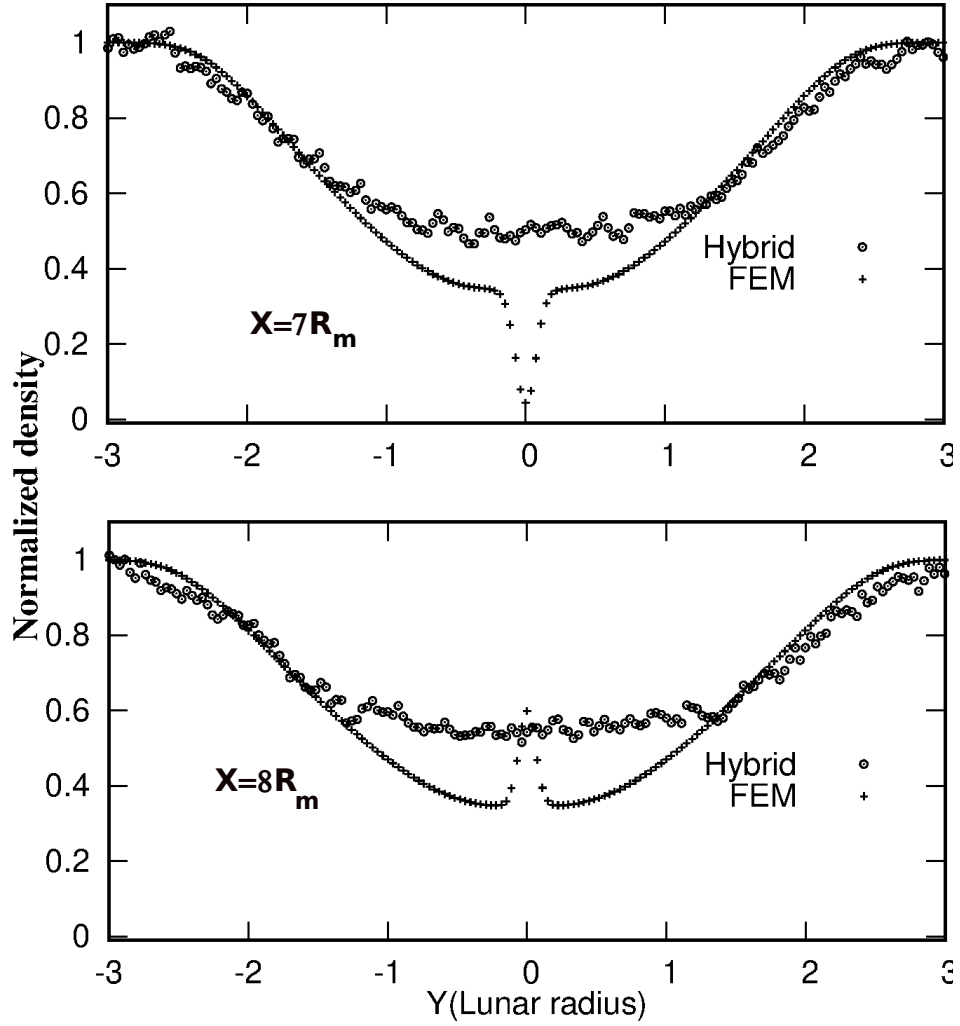


Figure 3.13: Normalized total density calculated with the finite element model (FEM) compared with the results of the hybrid code along  $Y$  at different cuts in  $X$ . From top to bottom,  $X = 7 R_m$  and  $X = 8 R_m$ .

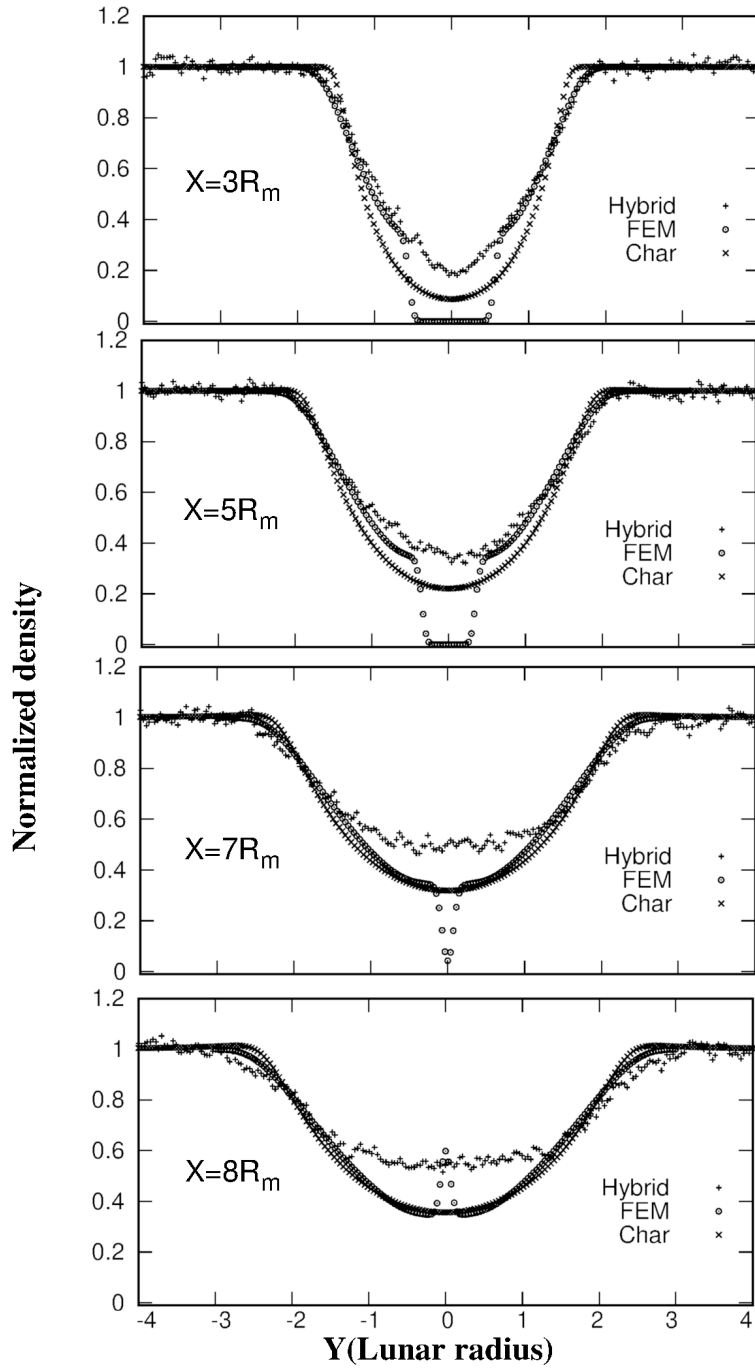


Figure 3.14: Normalized total density calculated with the finite element model (FEM), the hybrid code (Hyb) and, the method of characteristics (Char) are plotted as a function of  $Y$  at different cuts in  $X$ . From top to bottom,  $X = 3 R_m$ ,  $X = 5 R_m$ ,  $X = 7 R_m$  and,  $X = 8 R_m$ .

# Chapter 4

## Test-particle simulations

Fully kinetic descriptions offer the complete model to study a many-body system, but due to the complexity required computer time, it is not always practical in many cases. As kinetic simulations show the microscopic view of particles in a system, fluid approaches provide a macroscopic description of particles. Although fluid simulations are much simpler to implement, they cannot describe phenomena occurring in a very short time or fine space scales. Here, the test-particle method is applied to calculate particle trajectories by using approximated fields obtained from a low-level approach, such as fluid or analytic models without solving a fully self-consistent kinetic calculation. Test particle simulations produce approximate particle distribution functions which can be informative since they are as accurate as the possible from the fields used in the calculations of particle trajectories. Particle methods have been used to study different problems in space physics. For example, Wang et al. [73] shows a simple simulation model on electrostatic levitation of lunar dust particles (for a single dust particle) in the lunar terminator region. The electric field obtained from a full-particle PIC simulation is applied in a test-particle model to study the dust levitation. This method integrates the test-particle trajectories in the electric and magnetic fields. There are different types of formulations for test-particle models: (1) trajectory sampling, (2) forward Monte Carlo, (3) forward Liouville and (4) backward Liouville which are described in [50]. In a collisionless plasma, forward and backward Liouville method is used to conduct test-kinetic modeling. In these methods, Liouville's theorem

is applied to a one-particle distribution function which does not change in time ( $\frac{df}{dt} = 0$ ) along a particle trajectory. In the backward approach which is used in this thesis, for each test-particle, the equation of motion is integrated backward in time.

We recall that the distribution is the function of seven independent variables  $f(x, y, z, v_x, v_y, v_z, t)$  in the phase space  $(\mathbf{r}, \mathbf{v})$  at the time  $t$ . It is proportional to the probability density of points in the phase space at the time  $t$ . The test-particle code [72] calculates the particle distribution functions of given species at specified positions in space by using the particle backtracking (backward Liouville) approach. The code uses electric and magnetic fields obtained from the analytic model Ch. 2 to give a first approximation of the kinetic structure of a plasma.

## 4.1 Algebraic expression for parallel velocities

In this section, the analytic expression for electric fields in the lunar wake is derived. By using the electron parallel momentum equation and assuming that plasma is quasi-neutral because the Debye length is much smaller than any length scale in the problem ( $n_e = Zn$ ), one finds the familiar adiabatic relation between the electric potential and parallel pressure gradients as stated in Eq. (2.19). Perpendicular electric field has two components one is in the plane of magnetic field and solar wind flow  $\mathbf{B} - \mathbf{v}$  which comes from perpendicular pressure gradients and the  $-\mathbf{v} \times \mathbf{B}$  convective electric field. The electric field components in the plane of magnetic field and solar wind are,

$$E_{\parallel} = - \left( \frac{T_e}{e} \right) \left( \frac{1}{n_1 + n_2} \right) \left( \frac{1}{R_m} \right) (-n_1 \nabla_{\parallel} M_{1\parallel} + n_2 \nabla_{\parallel} M_{2\parallel}), \quad (4.1)$$

and,

$$E_{\perp} = - \left( \frac{T_e}{e} \right) \left( \frac{1}{n_1 + n_2} \right) \left( \frac{1}{R_m} \right) (-n_1 \nabla_{\perp} M_{1\parallel} + n_2 \nabla_{\perp} M_{2\parallel}), \quad (4.2)$$

where,  $T_e$  and  $e$  are electron temperature and charge respectively.  $M_{1,2}$  and  $n_{1,2}$  are the Mach number and the number density of fluid 1,2. All the coordinates are normalized to the lunar radius  $R_m$ . The goal is to find the analytic

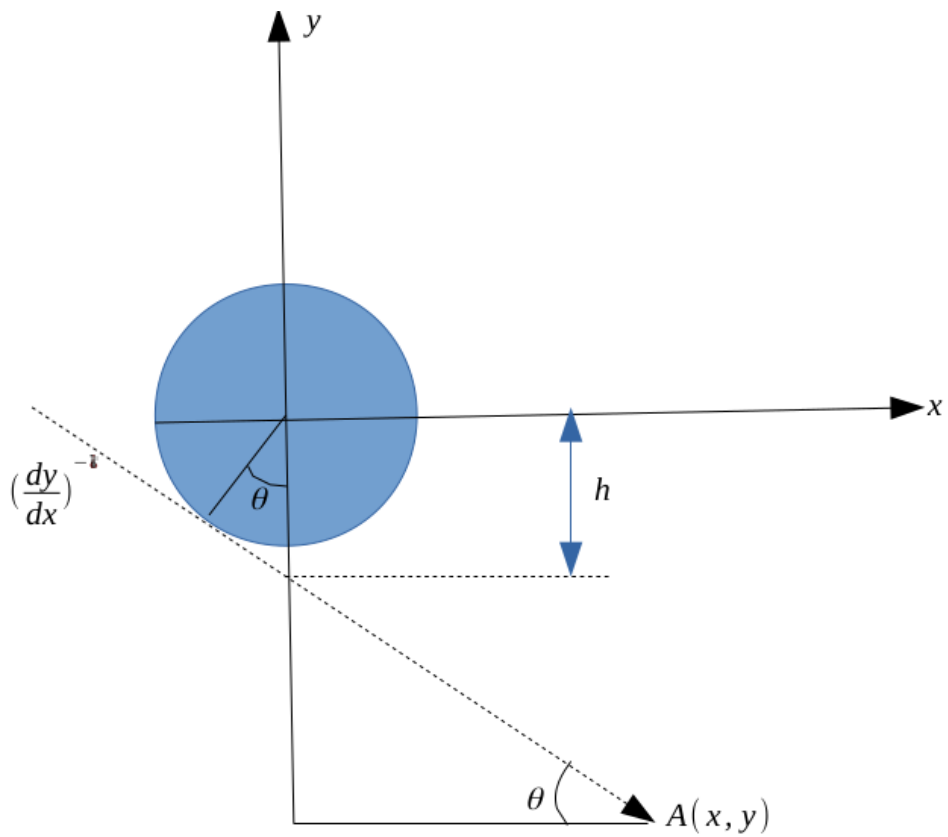


Figure 4.1: The negative characteristic  $(\frac{dy}{dx})^-$  is drawn for any arbitrary point  $A(x, y)$ . Intersection between  $(\frac{dy}{dx})^-$  and  $Y$  axis can indicate parameter  $h$ .

expression of parallel velocities corresponding to the ions expanding in the wake from both sides. For this purpose, the lower boundary between the wake and the unperturbed solar wind which is defined as the negative characteristics in Ch. 2 at any arbitrary point  $A(x, y)$  in front of the Moon are derived analytically (refer to the Eq. (2.29)),

$$\left. \frac{dy}{dx} \right|^- = \frac{-\sin(\alpha) - M_{\perp} \cos(\alpha) + M_{1\parallel} \sin(\alpha)}{-\cos(\alpha) + M_{\perp} \sin(\alpha) + M_{1\parallel} \cos(\alpha)}. \quad (4.3)$$

Referring to Fig. 4.1, simple geometric considerations show that,

$$\left. \frac{dy}{dx} \right|^- = \frac{y + h}{x}, \quad (4.4)$$

where, the intersection between the negative characteristic and the  $Y - axis$  is  $h$ . Assuming an angle  $\alpha$  between the magnetic field and the solar wind flow velocity, see Fig. 2.2,  $\theta$  is the angle between the negative characteristic with respect to the horizontal axis,

$$\cos(\theta) = \frac{1}{h}, \quad (4.5)$$

and,

$$\cos(\theta) = \frac{x}{\sqrt{x^2 + (h + y)^2}}. \quad (4.6)$$

The value of  $h$  can be found from eqs. (4.5) and (4.6),

$$h = \frac{-(x^2 + y^2)}{y - x\sqrt{x^2 + y^2 - 1}}. \quad (4.7)$$

Equations (4.3), (4.4), and (4.7) are combined and the analytic expression for the parallel velocity entering the wake from below the Moon becomes,

$$M_{1\parallel} = 1 - M_{\perp} \left\{ \frac{\cos(\alpha)[-y + x\sqrt{x^2 + y^2 - 1}] + \sin(\alpha)[x + y\sqrt{x^2 + y^2 - 1}]}{\cos(\alpha)[x + y\sqrt{x^2 + y^2 - 1}] + \sin(\alpha)[y - x\sqrt{x^2 + y^2 - 1}]} \right\}. \quad (4.8)$$

It is noticeable that  $M_{1\parallel}$  cannot be calculated with the analytic model beyond the line  $y' = \tan(\alpha)x - \frac{1}{\cos(\alpha)}$ .  $y'$  is tangent to the Moon from below with the slope of  $\tan(\alpha)$ . The negative characteristic is plotted as a function of  $M_{1\parallel}$  in Fig. 4.2. It can be seen that the negative characteristic cannot exceed by increasing  $M_{1\parallel}$ . There is no solution for  $M_{1\parallel}$  above the dash line  $y'$

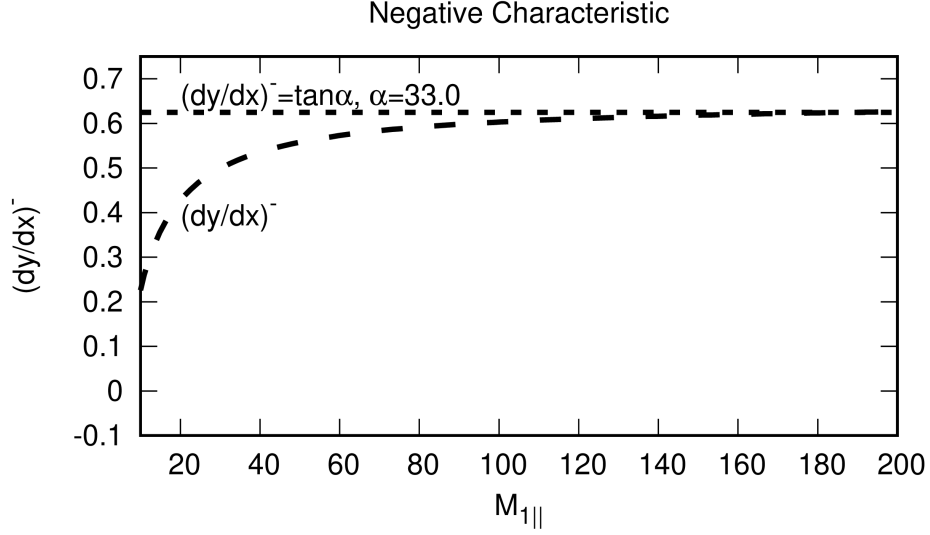


Figure 4.2: Negative characteristic plotted as a function of  $M_{1||}$ . It can be seen that the negative characteristic has an asymptotic limit of  $\tan(\alpha)$  as  $M_{1||}$  approaches infinity.

in the analytic model, which does not affect the accuracy of analytic model results because very few particles can reach this point from below. The upper boundary between the wake and the unperturbed solar wind which is defined as positive characteristic in Ch. 2 from the analytic expression and geometry are written respectively as,

$$\left. \frac{dy}{dx} \right|^+ = \frac{+\sin(\alpha) - M_{\perp} \cos(\alpha) + M_{2||} \sin(\alpha)}{+\cos(\alpha) + M_{\perp} \sin(\alpha) + M_{2||} \cos(\alpha)}, \quad (4.9)$$

and,

$$\left. \frac{dy}{dx} \right|^+ = \frac{y - h}{x}. \quad (4.10)$$

The intersection between the positive characteristic and ( $Y - axis$ ) gives  $h$ ,

$$h = \frac{(x^2 + y^2)}{y + x\sqrt{(x^2 + y^2 - 1)}}. \quad (4.11)$$

Then the parallel velocity entering the wake from above is formulated analytically as

$$M_{2||} = -1 - M_{\perp} \left\{ \frac{\cos(\alpha)[y + x\sqrt{x^2 + y^2 - 1}] + \sin(\alpha)[-x + y\sqrt{x^2 + y^2 - 1}]}{\cos(\alpha)[-x + y\sqrt{x^2 + y^2 - 1}] - \sin(\alpha)[y + x\sqrt{x^2 + y^2 - 1}]} \right\}. \quad (4.12)$$

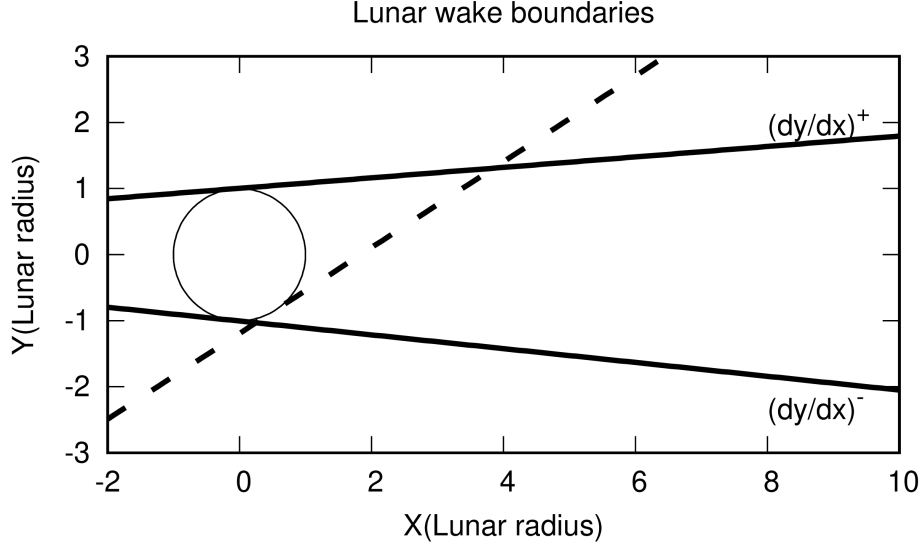


Figure 4.3: Negative and positive characteristics in the solar wind are in solid lines which shows the lunar wake boundaries. The analytic model cannot predict parallel velocity of ions entering to the wake from below  $M_{1\parallel}$  above the dashed line.

The analytic expressions for the electric field in the plane of the magnetic field and solar wind becomes,

$$E_{\parallel} = - \left( \frac{T_e}{e} \right) \left( \frac{M_{\perp}}{n_1 + n_2} \right) \left( \frac{x^2 + y^2}{\sqrt{x^2 + y^2 - 1}} \right) \left[ n_1 \frac{y - x\sqrt{x^2 + y^2 - 1}}{C1} + n_2 \frac{y + x\sqrt{x^2 + y^2 - 1}}{C2} \right] \quad (4.13)$$

and,

$$E_{\perp} = - \left( \frac{T_e}{e} \right) \left( \frac{M_{\perp}}{n_1 + n_2} \right) \left( \frac{x^2 + y^2}{\sqrt{x^2 + y^2 - 1}} \right) \left[ n_1 \frac{x + y\sqrt{x^2 + y^2 - 1}}{C1} + n_2 \frac{x - y\sqrt{x^2 + y^2 - 1}}{C2} \right], \quad (4.14)$$

where the denominators  $C1$  and  $C2$  are

$$C1 = \left[ \cos(\alpha) \left( x + y\sqrt{x^2 + y^2 - 1} \right) + \sin(\alpha) \left( y - x\sqrt{x^2 + y^2 - 1} \right) \right]^2, \\ C2 = \left[ \cos(\alpha) \left( -x + y\sqrt{x^2 + y^2 - 1} \right) - \sin(\alpha) \left( y + x\sqrt{x^2 + y^2 - 1} \right) \right]^2. \quad (4.15)$$

## 4.2 Maxwellian distribution function

A distribution function,  $f(\mathbf{X}, \mathbf{V}, t)$  varies in space, velocity, and time therefore there is no graphical representation of the six-dimensional phase space. However, by knowing the velocity dependence in a specific position in a space many of the characteristic features of the plasma can be understood [2]. There are different types of velocity space distribution functions known in the solar wind plasma. One of the well-studied distribution functions is the drifting Maxwellian distribution which is defined as,

$$f_s = n_s \left( \frac{m_s}{2\pi k_B T_s} \right)^{3/2} \exp \left( -\frac{m_s (\mathbf{V} - \mathbf{v}_s)^2}{2k_B T_s} \right), \quad (4.16)$$

This is an isothermal distribution in a thermal equilibrium. The left panel of Fig. 4.5 illustrates a drifting Maxwellian distribution function.

## 4.3 Results

The analytic electric fields (4.13)-(4.15) are applied to the test-particle code to determine the distribution function of ions inside and outside of the lunar wake in the night-side of the Moon. In these simulations the interplanetary magnetic field is  $\mathbf{B}_{\text{IMF}} = 5$  nT along the  $Y$  - *axis* and the solar wind flow is assumed to be in the  $+X$  direction with the magnitude of  $\sim 295.6$  km/s ( $\alpha = 90^\circ$ ). The background density is  $n_{\text{sw}} = 5$  cm $^{-3}$ , the electron and ion temperatures are  $T_e \simeq 10.0$  eV and  $T_i \simeq 5.7$  eV. Specifically, with the parameters given above, the sound speed is  $c_s \sim 48.8$  km/s and the corresponding upstream Mach number is  $M_\perp \simeq 6$  and  $M_\parallel = 0$ . Ions distribution function is calculated in different positions along the curve below Fig. 4.4

$$\begin{aligned} x_i &= 1.1R_m \cos(\eta_i), \\ y_i &= 1.1R_m \sin(\eta_i), \end{aligned} \quad (4.17)$$

$$-0.55\pi < \eta_i < -0.25\pi.$$

Figures 4.5-4.6 show distribution functions of hydrogen ions at different positions in front of the Moon. The velocities are normalized in ion thermal velocity,  $V_{Th} = \sqrt{\frac{T_i}{m_i}}$ . The distribution function is Maxwellian outside the

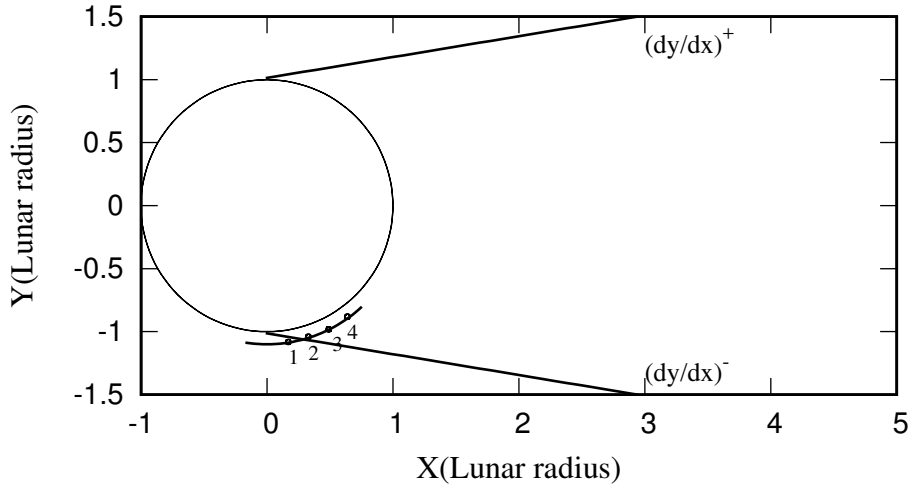


Figure 4.4: The calculations of distribution function and moments are done along this curve which is started somewhere in the terminator and enter the lunar wake from below.

wake as it is assumed in the analytic model. By moving to the wake, the ion distribution function is not Maxwellian anymore, which means that the ions are not in thermal equilibrium. The trajectory in which the calculations are conducted has been started in the unperturbed region at the lunar terminator,  $X \simeq -0.17 R_m$ ,  $Y \simeq -1.086 R_m$  as shown in Fig. 4.4. Next point in the trajectory  $X \simeq 0.33 R_m$  and  $Y \simeq -1.04 R_m$  is on the boundary of the wake and the other points are progressively are inside the wake area.

### 4.3.1 Moments of the distribution function

Macroscopic details of the distribution functions are functions of position and time and can be obtained by integrating the distribution function over the velocities. The general approach to calculate the k-th moment of a single particle distribution function  $f_s(\mathbf{r}, \mathbf{v}, t)$  is written as

$$\mathbf{M}_k(\mathbf{r}, t) = \int \mathbf{V}^k f_s(\mathbf{r}, \mathbf{v}, t) d^3\mathbf{V}. \quad (4.18)$$

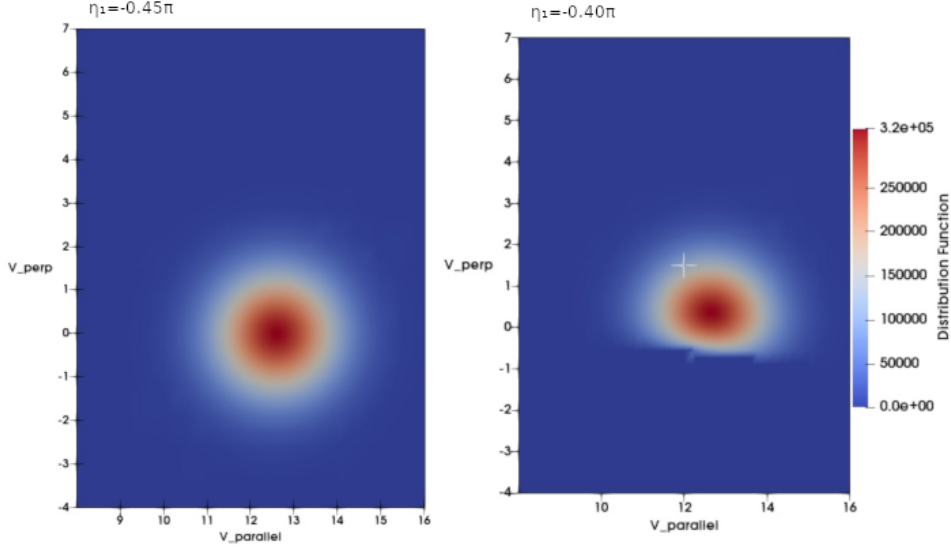


Figure 4.5: Distribution functions are plotted at two different positions in the day-side of the Moon with the distance of  $1.1R_m$  with lunar origin. The left one is Maxwellian because it is calculated in the unperturbed solar wind  $\eta = -0.45\pi$ . The right distribution is calculated inside the wake at  $\eta = -0.40\pi$

Here  $\mathbf{M}_k$  is the moment (macroscopic variable) of the distribution function and defining general tensor of rank  $k$  [27]. In Eq. 4.18,  $d^3\mathbf{V} = dv_x dv_y dv_z$ . The lower moments relate to familiar macroscopic variables appearing in fluid descriptions of plasma. Examples are given below.

- **Zeroth moment** of distribution function ( $k = 0$ ) gives the number density of particle  $s$  which has the unit of  $\text{m}^{-3}$  in SI,

$$n_s(\mathbf{r}, t) = \int f_s(\mathbf{r}, \mathbf{v}, t) d^3\mathbf{V}. \quad (4.19)$$

Figure 4.7 shows the density of ions penetrating the lunar wake from below along the curve (see Fig. 4.4), calculated from the zeroth moment of the distribution functions obtained from the test-particle code. This density is compared with the one predicted with the analytic model. Densities are normalized to the incident solar wind density. An excellent agreement between the two densities is obtained everywhere except for small variations in the wake, where the plasma is not in thermal equilibrium. A small deviation around  $\eta \sim -0.35\pi$  can be seen which could be due to the discretization errors. Close to the Moon, the density in the wake is a quasi perfect vacuum because very

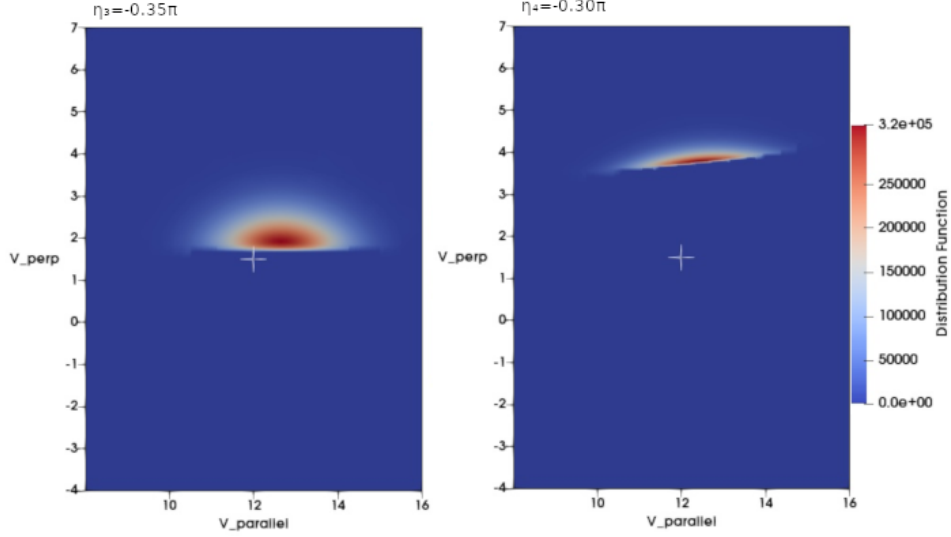


Figure 4.6: Ion distribution functions plotted at  $\eta = -0.35\pi$  &  $-0.30\pi$  which are in the lunar wake.

few ions can reach this point from both sides. In Ch. 2 it is shown that the density calculated analytically inside the wake ( $Y = 0$ ,  $X = 2R_M$ ) is  $\simeq 0.087n_{sw}$  which means there are only 0.27 ions per cubic cm in that region. Consequently, the calculated distribution function becomes increasingly singular. In those regions ( $-0.40\pi < \eta < -0.25\pi$ ) the maximum difference between the two densities is of order  $0.005n_{sw}$ , which is very small. However, in the unperturbed solar wind regions ( $-0.55\pi < \eta < -0.40\pi$ ) the discrepancies are even smaller and the maximum relative difference is of order 0.6% as listed in Table 4.1.

- **First moment** of distribution function ( $k = 1$ ) is the particle flux density of specie  $s$ ,

$$n_s \mathbf{V}_s(\mathbf{r}, t) = \int \mathbf{V} f_s(\mathbf{r}, \mathbf{v}, t) d^3\mathbf{V}, \quad (4.20)$$

where  $\mathbf{V}_s$  is called the plasma bulk flow velocity of particles of type  $s$ . In contrast to the assumption of constant perpendicular velocity made in the analytic model, Fig. 4.8 shows variations in  $M_\perp$  in the wake region. Quantitatively,  $M_\perp$  remains constant within  $\simeq 0.3\%$  almost everywhere in the solar wind area (refer to Table 4.1), the exception being in the wake region where the maximum discrepancy is of order  $\simeq 16\%$ . This agreement supports the

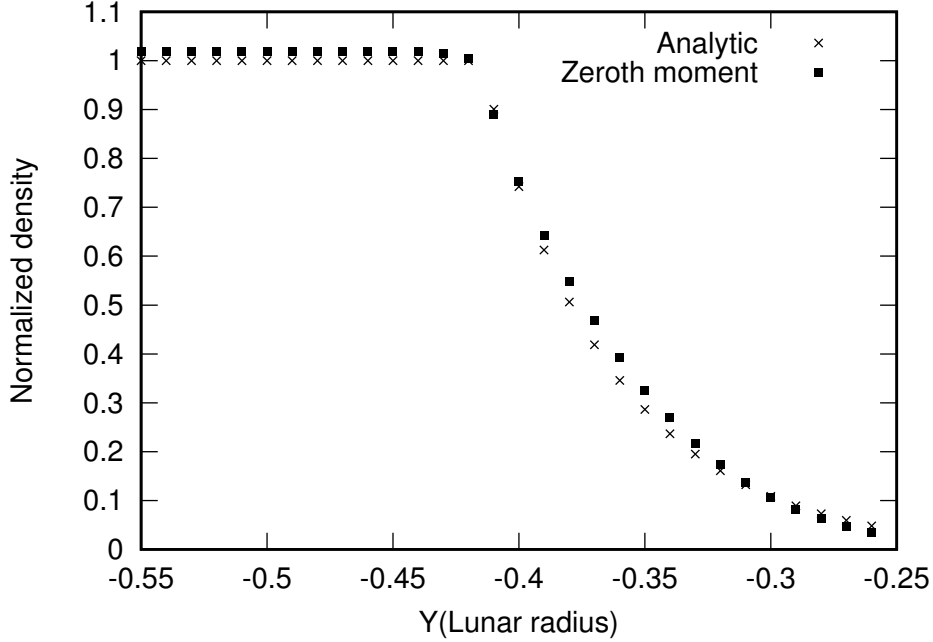


Figure 4.7: The zeroth moments of the ion distribution function is compared with the density of the ions entering to the Moon from the below.

assumption made in the analytic model that  $M_{\perp}$  is approximately constant. In the analytic model,  $Z$  components are not taken into account because in the assumed 2D cylindrical model,  $Z$  is an ignorable coordinate. The  $Z$  component of the flow velocity calculated from the distribution function remains very close to zero in the solar wind area as expected. In the wake region, the maximum absolute calculated value of Mach number in the  $Z$  direction,  $M_z$ , is  $\sim 0.25$ , which is very small as seen in Fig. 4.9. Figure 4.10 shows parallel Mach number of two models which are in a very good agreement. In the wake the maximum discrepancy between the calculated parallel velocity from the test-particle model and the one calculated analytically is  $\sim 0.64$  which is relatively small. In the solar wind, where plasma is described by a drifting Maxwellian velocity distribution function, as seen in Fig. 4.5, the maximum differences in  $M_{\parallel}$  are of order  $\sim 0.03$ .

- **Second moment** of distribution function explained the flow  $\mathbf{V}$  of momentum  $m_s \mathbf{V}$  in the laboratory frame,

$$P_s(\mathbf{r}, t) = \int m_s \mathbf{V} \mathbf{V} f_s(\mathbf{r}, \mathbf{v}, t) d^3 \mathbf{V}, \quad (4.21)$$

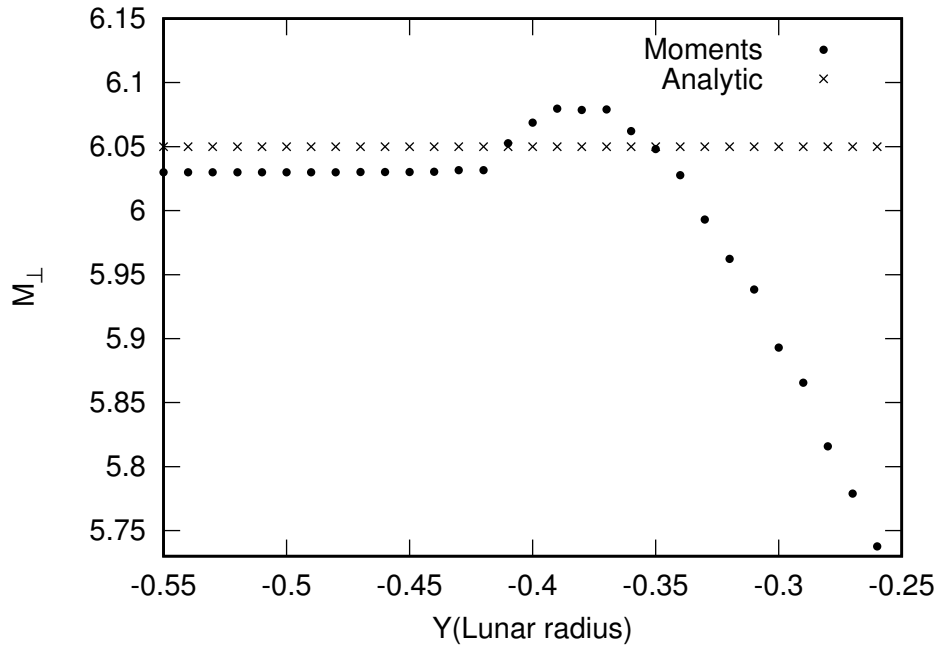


Figure 4.8: The validity of constant perpendicular velocity is examined by calculating  $M_{\perp}$  from distribution function obtained with test-particle code.

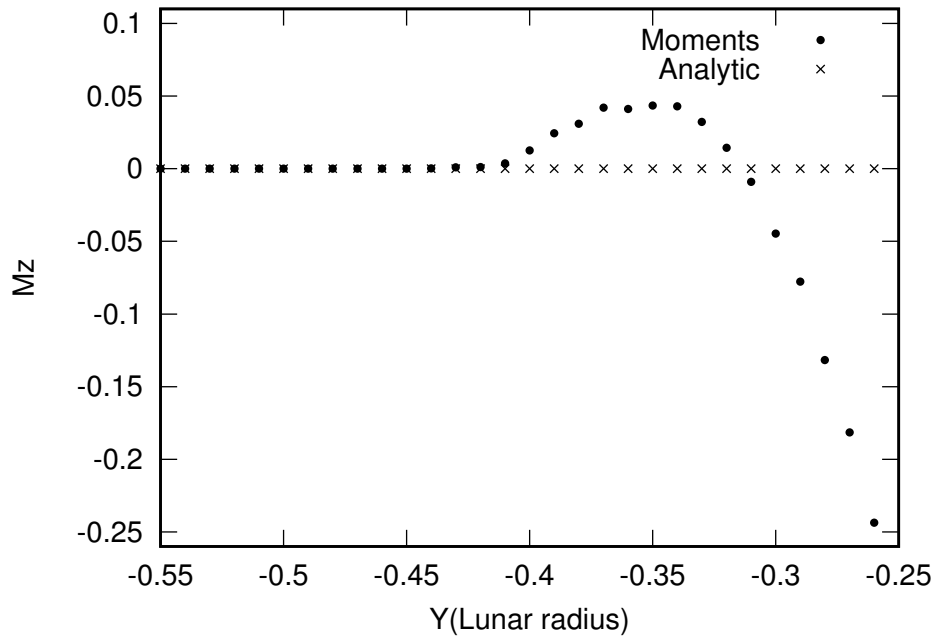


Figure 4.9: This figure shows variations of  $v_z$  in the test-particle code from zero which is assumed in the analytic model.

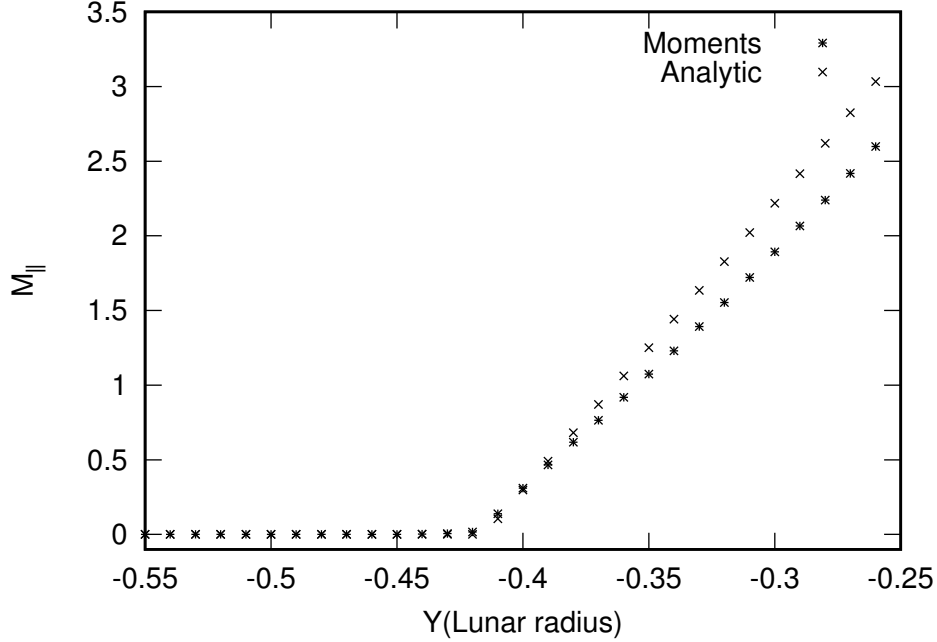


Figure 4.10:  $M_{\parallel}$  calculated from the first moment of the distribution function is compared with the parallel velocity entered to the wake from below.

$\mathbf{P}_s$  is called stress tensor. By calculating the second moment in the frame of the particle the pressure tensor  $\mathbf{p}_s$  is attained,

$$\mathbf{p}_s(\mathbf{r}, t) = \int m_s(\mathbf{V} - \mathbf{V}_s)(\mathbf{V} - \mathbf{V}_s)f_s(\mathbf{r}, \mathbf{v}, t)d^3\mathbf{V}. \quad (4.22)$$

In the Analytic model it is assumed that the ions are in thermal equilibrium so an isotropic pressure is expected

$$\mathbf{p}_s = \begin{pmatrix} p_{xx} & 0 & 0 \\ 0 & p_{yy} & 0 \\ 0 & 0 & p_{zz} \end{pmatrix}, \quad (4.23)$$

where,  $p_{xx} = p_{yy} = p_{zz} = p_s = 4.56 \times 10^{-3}$ (nPa). Another assumption made in the analytic models is the ideal gas equation of state which is described in Sec. 1.6.3. At  $\eta = -0.45\pi$  which is in the unperturbed solar wind area, calculated pressure tensor is

$$p_s(\text{nPa}) = \begin{pmatrix} 4.66 \times 10^{-3} & -1.85 \times 10^{-6} & 6.32 \times 10^{-8} \\ -1.85 \times 10^{-6} & 4.69 \times 10^{-3} & -1.63 \times 10^{-6} \\ 6.32 \times 10^{-8} & -1.63 \times 10^{-6} & 4.69 \times 10^{-3} \end{pmatrix}. \quad (4.24)$$

In this region of the solar wind, the off-diagonal elements are indicative of discretisation errors made in the test-particle method and the integration of

	Analytic	Moments of distribution function	Percentage discrepancy
$Dn$ (1/m <sup>3</sup> )	$5.00 \times 10^6$	$5.04 \times 10^{-6}$	0.64
$v_x$ (m/s)	$2.95 \times 105$	$2.94 \times 105$	0.34
$v_y$ (m/s)	0.00	$5.70 \times 10^{-4}$	-
$p_s$ (nPa)	$4.56 \times 10^{-3}$	$4.61 \times 10^{-3}$	1.01

Table 4.1: The moments calculated from the distribution function are compared with the assumptions were made in the analytic model. The distribution function is computed from test-particle code at the position which is perfectly outside the wake  $\eta = -0.45$  (in the solar wind region where plasma is assumed to be in thermodynamic equilibrium).

distribution functions to obtain the second order moments. The maximum relative difference between the diagonal elements and the assumed pressure in the analytic model is of order 1.0% (refer to Table. 4.1). For the perturbed regions inside wake  $\eta = -0.35\pi$ , the plasma is not in thermodynamic equilibrium and the pressure tensor is calculated as

$$p_s(\text{nPa}) = \begin{pmatrix} 1.52 \times 10^{-3} & -8.08 \times 10^{-6} & -7.61 \times 10^{-6} \\ -8.08 \times 10^{-6} & 2.39 \times 10^{-4} & -2.37 \times 10^{-5} \\ -7.61 \times 10^{-6} & -2.37 \times 10^{-5} & 1.51 \times 10^{-3} \end{pmatrix}, \quad (4.25)$$

whereas, the plasma fluid pressure of the analytic model is assumed  $1.30 \times 10^{-3}$ nPa. The diagonal elements of the pressure tensor Eq. (4.23) along with the pressure of the analytic model, are plotted in Fig. 4.11. The curve begins in the unperturbed region with  $n = n_{SW}$  and, ends inside the wake with  $n = 0$ . By the assumptions of ideal gas and isothermal fluid, diagonal elements of the pressure tensor are expected to decrease along this trajectory. Figure 4.11 illustrates a general qualitative agreement between the analytic pressure, and the ones are calculated from the test-particle analysis. Some significant variations can be seen between  $pyy$  and the analytic pressure inside the vacuum area. This shows that the pressure tensor becomes increasingly anisotropic as one penetrates the wake, contrary to the assumption of an isothermal isotropic ion distribution assumed in the analytic model.

Table 4.1 shows some of the macroscopic parameters calculated from the distribution function in the unperturbed solar wind area  $\eta = -0.45$  or  $X = 0.017R_m, Y = -1.08R_m$ , where the calculated distribution function with the

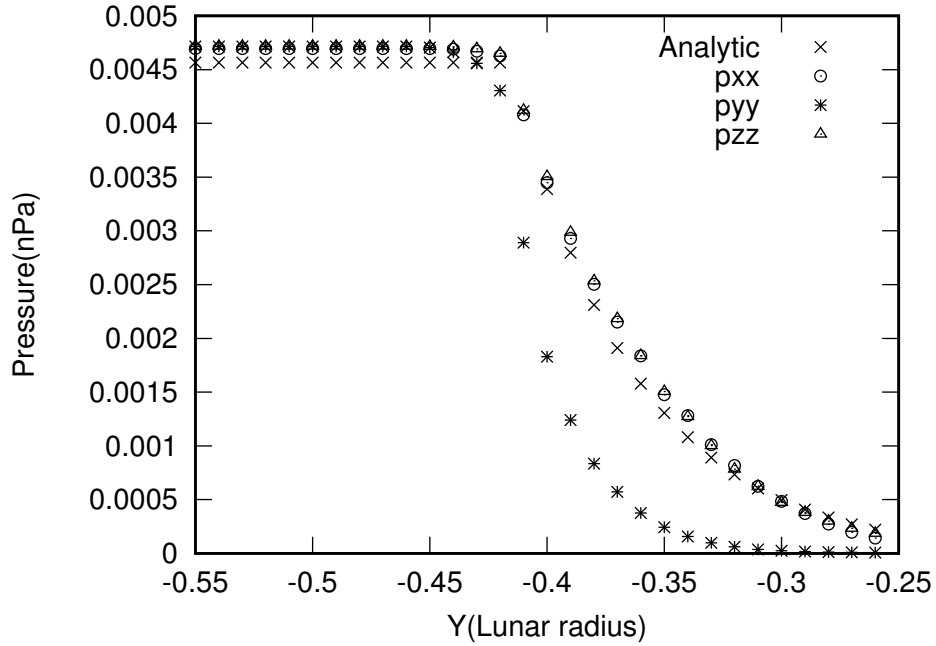


Figure 4.11: The diagonal elements of the pressure tensor is compared with the analytic pressure profile along the curve in Eq. (4.17).

test-particle code at this point is a Maxwellian. The discrepancies between the calculated moments and the analytic values are relatively small. Therefore, I conclude that the assumptions were made in the analytic model constitute good approximations.

# Chapter 5

## Comparisons with ARTEMIS observations

In 2010 two of the five in-orbit spacecraft ("probes") from the project "Time History of Events and Macroscale Interactions during Substorms" (THEMIS) were sent to lunar orbit to study the Moon-Solar wind interactions, which is known as "Acceleration, Reconnection, Turbulence, and Electrodynamics of the Moon's Interaction with the Sun" (ARTEMIS) [1]. ARTEMIS measures the density, velocity, and temperature of the ambient plasma from distances hundreds of kilometers to 120,000 km from the Moon surface. The Electrostatic Analyzers (ESA) of ARTEMIS can measure the particle distribution function of electrons and ions over the energy range from  $\sim 3$  eV to  $\sim 30$  keV [1]. The ARTEMIS mission has two identical probes, P1 and P2, in elliptical orbits, with approximate orbital periods of 28 hours [1]. While one of the probes is crossing the lunar wake, the other one is located outside the wake and far from the lunar surface to measure the undisturbed solar wind as a reference. In this chapter, I report two different ARTEMIS observations of the lunar wake in order to compare with the density calculated with the method of characteristics.

**Case 1:** 13 February 2010 between 08:53 and 09:29 UT [68], [75].

**Case 2:** 13 March 2013 between 08:35 and 09:35 UT [62].

In Sec. 5.1, a short description of mapping 3D results into the 2D plane of  $\mathbf{V}_{SW} - \mathbf{B}$  is provided. In Sec. 5.2, there is a short description of transformation between various coordinate systems. Finally, results from ARTEMIS are

presented and compared with the ones obtained from models presented in the previous chapters.

## 5.1 Mapping a 3D wake into 2D

The method of characteristics and the alternative models consider simplified 2D wake models. ARTEMIS observations however, are of a 3D actual wake. In order to compare model predictions and observations, I need to map the 3D results measured with ARTEMIS into the 2D plane of  $\mathbf{V}_{SW} - \mathbf{B}$ . The procedure makes use of the fact that the characteristics, the Mach vectors, and the magnetic field, all lie in a single plane. Following the trajectory of ARTEMIS satellite, at each time step, a plane of  $\mathbf{V}_{SW}$  and  $\mathbf{B}$  intersects the Moon sphere, which defines a circle with radius of  $R_c$ . This circle represents the Moon in my 2D model of the wake (see the Fig. 5.1). The size of this circle (the 2D Moon) varies with the position of the satellite along its trajectory. Furthermore, it can be seen that in the characteristics description of the wake and solar wind, the ratio  $n/n_0$ , and  $M_{\parallel}$ , only depend on the relative position  $\mathbf{r}/R_c$  in the  $\mathbf{B} - \mathbf{V}_{SW}$  plane. The alternative models, the finite element, and the hybrid models do not depend on the actual size of the Moon. In the particular case, where  $\mathbf{V}_{SW}$  is along  $X$  and  $\mathbf{B} \parallel \hat{y}$ , the 2D plane of interest is simply the  $X - Y$  plane and the radius of the Moon cross section in the  $X - Y$  plane containing the satellite is given by  $R_c - \sqrt{R_m^2 - z_{SC}^2}$ , where  $R_m$  is the lunar radius and  $z_{SC}$  is the  $z$  coordinate of the spacecraft. It should be noted that in this two-dimensional approximation, no plasma flow in the  $z$  direction perpendicular to the  $\mathbf{B} - \mathbf{V}_{SW}$  plane is taken into account. However, this is not always the case;  $\mathbf{V}_{SW}$  and  $\mathbf{B}$  can have any arbitrary directions in space. In this general case, a coordinate transformation is needed to put  $\mathbf{V}_{SW} \parallel \hat{x}$  and  $\mathbf{B}$  in a plane of  $X - Y$  which is reviewed in the next section 5.2.

## 5.2 Coordinate transformation

The transformation from one coordinate system to another is always required as many of the measured quantities with the satellites are vectors. For a

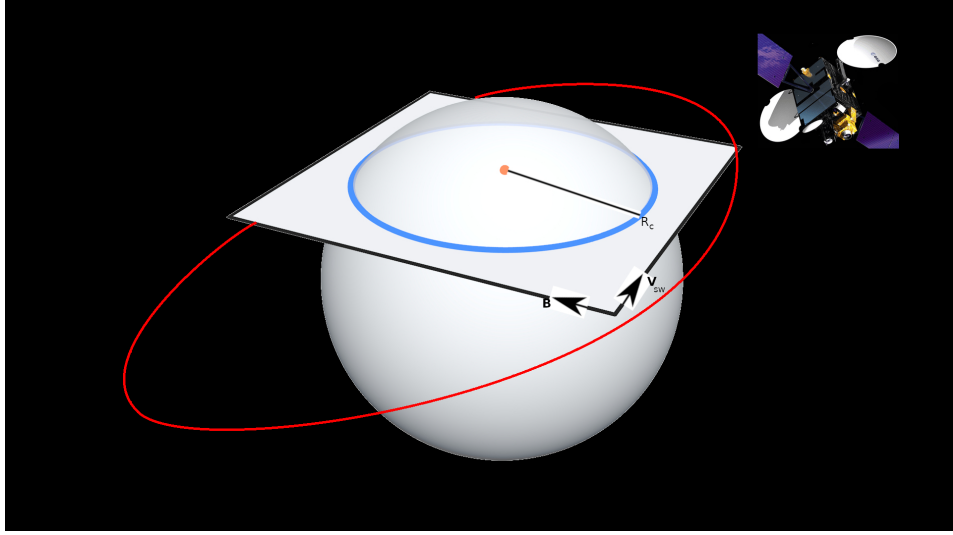


Figure 5.1: Following the trajectory of ARTEMIS satellite, at each time step, a plane of  $\mathbf{V}_{SW}$  and  $\mathbf{B}$  intersects the Moon sphere, which defines a circle with radius of  $R_c$ .

rotation, the conversion is usually done with a transformation matrix  $\mathbf{R}$  [24]. By rotating one system clockwise about one of the axis, one can transform a vector from one system to another. Some of the basic rotations are listed below. In all cases the rotation matrix transforms the original coordinate system by an arbitrary angle  $\theta$  about a given axis clockwise. The inverse of each matrix rotation leads to rotate the system counter-clockwise,

$\mathbf{R}_y(\theta)$  rotates the coordinate system about  $\hat{y}$ :

$$\mathbf{R}_y(\theta) = \begin{bmatrix} \cos(\theta) & 0 & \sin(\theta) \\ 0 & 1 & 0 \\ -\sin(\theta) & 0 & \cos(\theta) \end{bmatrix}, \quad (5.1)$$

$\mathbf{R}_x(\theta)$  rotates the coordinate system about  $\hat{x}$ :

$$\mathbf{R}_x(\theta) = \begin{bmatrix} 1 & 0 & 0 \\ 0 & \cos(\theta) & -\sin(\theta) \\ 0 & \sin(\theta) & \cos(\theta) \end{bmatrix}, \quad (5.2)$$

$\mathbf{R}_z(\theta)$  rotates the coordinate system about  $\hat{z}$ :

$$\mathbf{R}_z(\theta) = \begin{bmatrix} \cos(\theta) & -\sin(\theta) & 0 \\ \sin(\theta) & \cos(\theta) & 0 \\ 0 & 0 & 1 \end{bmatrix}. \quad (5.3)$$

In general, the vector positions of ARTEMIS trajectory in a coordinate system are  $\mathbf{pos} = (x, y, z)$ . Moreover, the solar wind velocity and magnetic

field vectors in the same coordinate system are given  $\mathbf{V}_{SW} = (v_x, v_y, v_z)$  and,  $\mathbf{B} = (B_x, B_y, B_z)$  respectively. I need to transform the old system to a new coordinate system  $(\acute{x}, \acute{y}, \acute{z})$  in which  $\mathbf{V}_{SW} \parallel \acute{x}$ . In addition, the magnetic field vector should be in a plane of  $\acute{x} - \acute{y}$  or  $\acute{x} - \acute{z}$ . In order to achieve this, these rotations need to be done :

1.  $\mathbf{R}_y(\alpha_1)$  will transform the vectors to an intermediate coordinate system,  $(\check{x}, \check{y}, \check{z})$ , in which the solar wind velocity in this system has just two components  $\check{\mathbf{V}}_{SW} = (\check{v}_x, \check{v}_y, 0)$ . The angle  $\alpha_1$  is

$$\tan(\alpha_1) = \frac{v_z}{v_x}, \quad (5.4)$$

2.  $\mathbf{R}_z^{-1}(\alpha_2)$  will transform the vectors from the previous system  $\acute{x} - \acute{y}$  or  $\acute{x} - \acute{z}$  to another intermediate coordinate system,  $(x'', y'', z'')$ . In this system the solar wind velocity has just one components  $\mathbf{V}_{SW}'' = (v_x'', 0, 0)$ .  $\alpha_2$  becomes,

$$\sin(\alpha_2) = \frac{\check{v}_y}{\sqrt{v_x^2 + v_y^2 + v_z^2}}, \quad (5.5)$$

3.  $\mathbf{R}_x(\alpha_3)$  will transform the vectors from the last intermediate system  $(x'', y'', z'')$  to the desired coordinate system  $(\acute{x}, \acute{y}, \acute{z})$ . By this last rotation the magnetic field and solar wind velocity are now in a same plane  $\acute{x} - \acute{z}$ . The angle  $\alpha_3$  becomes,

$$\tan(\alpha_3) = \frac{B_y''}{B_z''}. \quad (5.6)$$

## 5.3 Results

### 5.3.1 Case 1: 13 February 2010 between 08:53 and 09:29 UT

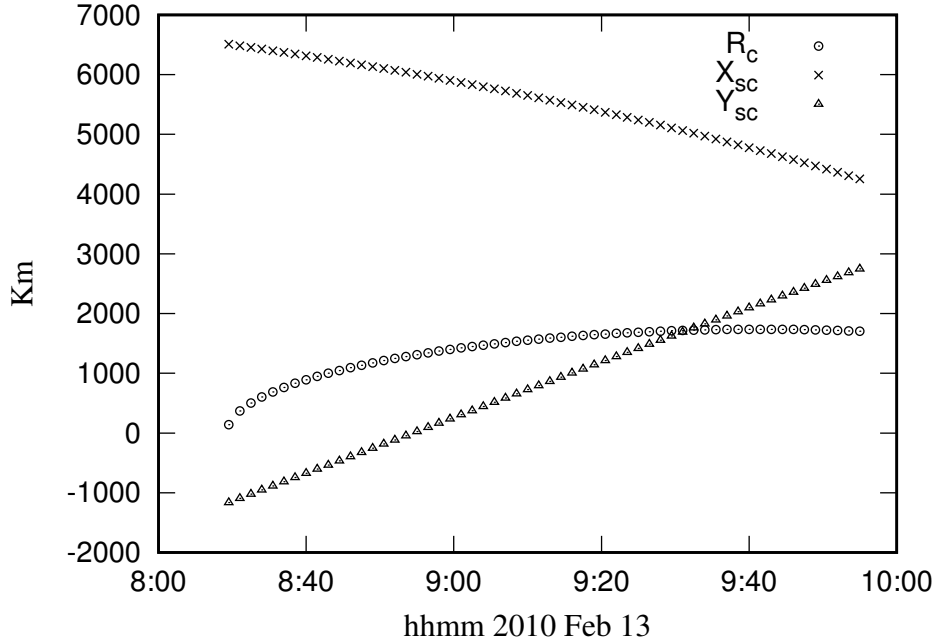


Figure 5.2: The coordinates related to the trajectory of P1 spacecraft of ARTEMIS mission on 13 February 2010 between 08:53 and 09:29 UT ( $X_{SC}$ ,  $Y_{SC}$ ) is plotted with the corresponding radius of cross section  $R_c$ .

On February 2010 ARTEMIS P1 (formerly THEMIS-B) passed for the first time through the lunar wake at a distance of  $\sim 3.5 R_m$  from the Moon center downstream [68], [75], while the P2 spacecraft of ARTEMIS (formerly THEMIS-C) was located in the solar wind which is chosen to be a reference for providing input to the models. In this first flyby, the Moon was located outside the magnetosphere, between the Earth and the Sun, so the solar wind was not perturbed by the presence of the Earth's magnetosphere. This event occurred on 13 February 2010 between 08:53 and 09:29 UT [68], [75]. The ambient plasma parameters are taken from ARTEMIS P2 where it was in the undisturbed solar wind region where ion and electron temperatures were

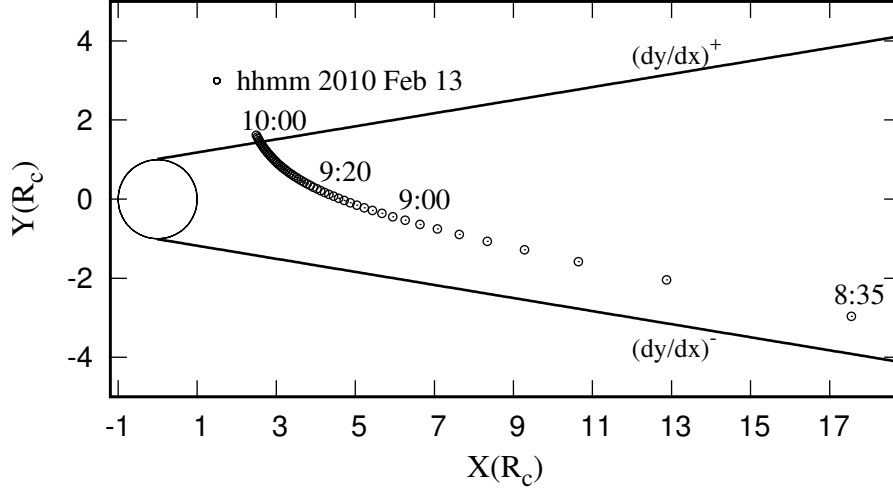


Figure 5.3: Trajectory of P1 spacecraft of ARTEMIS mission on 13 February 2010 between 08:35 and 09:29 UT mapped to a 2D plane containing  $\mathbf{B}$  and  $M_{\perp}$ . The boundary of wake which is calculated with the method of characteristics is marked with the top and bottom solid lines.

respectively  $T_i = 5.7$  eV and  $T_e = 14.3$  eV. The measured Interplanetary Magnetic Field was  $\mathbf{B}_{IMF} = [0.0, 6.0, 0.0]$  nT. The solar wind flow velocity and density were  $\mathbf{V}_{SW} = [-295.0, 0.0, 0.0]$  km/s and  $n_{SW} = 3.14$  cm $^{-3}$  respectively. The vectors,  $\mathbf{B}_{IMF}$  and  $\mathbf{V}_{SW}$  were given in Selenocentric Solar Ecliptic (SSE) coordinates. In these coordinates, the  $X$ -axis is along the Moon-Sun direction, positive towards the Sun. The  $Z$ -axis is perpendicular to the plane of the Earth's orbit around the Sun (ecliptic plane), positive north, and the  $Y$ -axis completes the right-handed set [75]. SSE coordinates are similar to those in Geocentric solar ecliptic (GSE) coordinates, except that the origin of the coordinates is at the center of the Moon instead of at the center of the Sun. First, the 3D results of the lunar wake are required to be mapped to a 2D plane containing  $\mathbf{B}$  and  $M_{\perp}$  as described in Sec. 5.1. For this special case where  $\mathbf{V}_{SW}$  is along  $X$  and  $\mathbf{B} \parallel \hat{y}$ , the 2D plane of interest is the  $X - Y$  plane and the radius of the Moon in that plane is given by  $R_c = \sqrt{R_m^2 - y_{SC}^2}$ . Figure 5.2 shows the real positions of the P1 satellite through the first flyby and the

radius of the Moon cross section  $R_c$  at these positions tends to small when the absolute value of  $y_{SC}$  is close to the Moon. This happened when P1 was entering the wake from below at about 8:35 UT as illustrated in Fig. 5.3. This figure demonstrates the 2D wake boundary from the method of characteristics as well as the normalized positions of the P1 spacecraft through this flyby. By approaching the center of the Moon  $R_c$  becomes larger. Between 8:40 and 10:00 UT, P1 ranges from  $X \sim 18 R_c, Y \sim -3 R_c$  to  $X \sim 2.5 R_c, Y \sim 1.6 R_c$  which from Fig. 5.3 is inside the wake. It can be seen that initially, it is relatively far from the Moon, and that it gradually approaches the lunar surface where the analytic model is most accurate. The density calculated with the method of characteristics, along the P1 spacecraft trajectory is compared with in situ measurements in Fig. 5.4. The density obtained with the method of

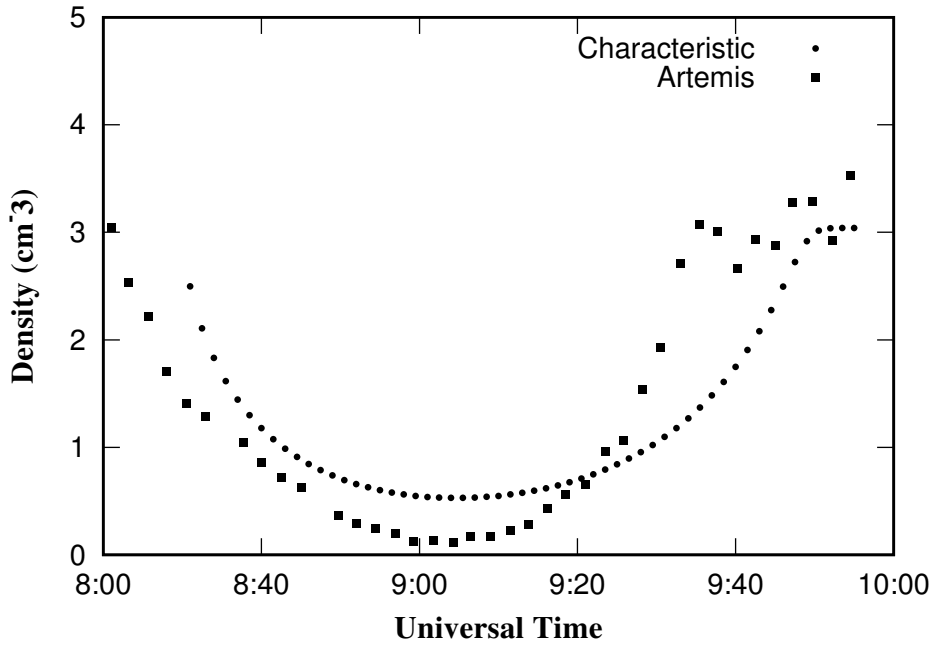


Figure 5.4: Ion density in ARTEMIS data (square) with the method of characteristics (filled circle) are plotted along the trajectory of the P1 spacecraft during the first flyby.

characteristics is seen to be in good agreement with measured values. Quantitatively, the two densities agree within  $\simeq 8\%$  with respect to upstream (unperturbed) density almost everywhere. Qualitatively, the shapes of the wakes are similar. Density measured from ARTEMIS shows some variations, and

the method of characteristics density profile is smooth. Besides, the minimum density measured from ARTEMIS is around  $\sim 0.174$  of the background plasma density, which is lower in comparison to the method of characteristics wake depth which is  $\sim 0.167 n_{SW}$ . The good qualitative and quantitative agreement between the method of characteristics and ARTEMIS densities indicates that the assumptions are made to build this model are approximately correct, and this 2D model can capture some of the main features of the lunar wake. The ion density in ARTEMIS data (cross) is also compared with the density calculated with the finite element method (circle) along the trajectory of the first ARTEMIS flyby as shown in Fig. 5.5. There is a sharp discontinuity in the density in ARTEMIS between 9:20 to 9:45 UT, it may be due to the formation of a shock front on the night-side of the Moon. In the finite element model, a sharp drop of density in the wake can be seen as discussed in the Ch. 3. Quantitatively, the two densities agree within  $\simeq 3\%$  almost everywhere except near the edge of the wake. The depth of the wake from ARTEMIS data and the finite element model is  $\sim 3.9\%$  of the background plasma density, while the one calculated with the method of characteristics is higher  $\sim 16.2\%$  as seen in Fig. 5.6. I conclude that in this comparison, the finite element model has a better agreement with ARTEMIS measurement.

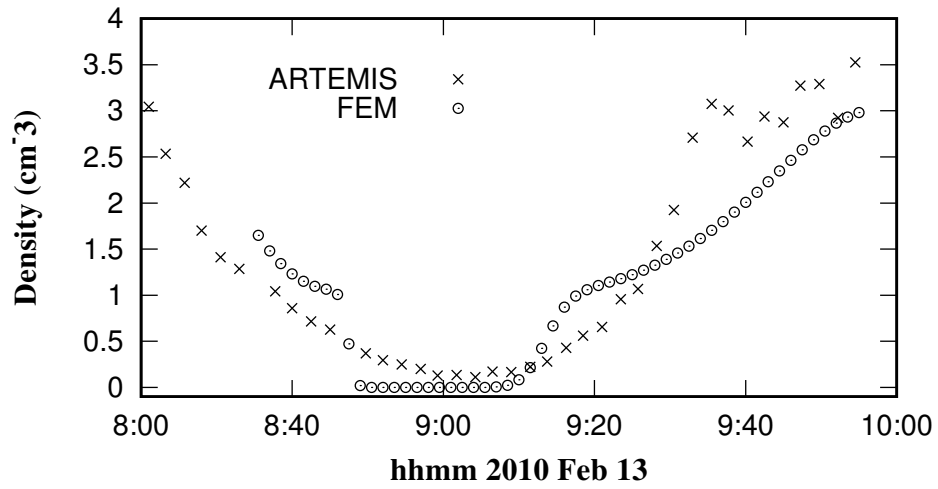


Figure 5.5: Ion density computed with the finite element model (FEM) compared with ARTEMIS data along the trajectory of the P1 spacecraft of ARTEMIS mission on 13 February 2010 between 08:53 and 09:29 UT

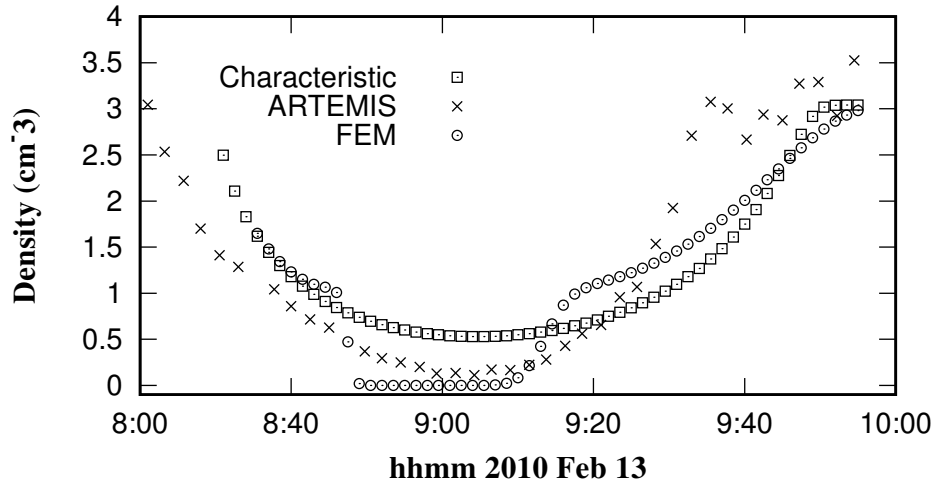


Figure 5.6: Ion density computed with the finite element model (FEM) compared with that computed with the method of characteristics and ARTEMIS data along the trajectory of the P1 spacecraft of ARTEMIS mission on 13 February 2010 between 08:53 and 09:29 UT

### 5.3.2 Case 2: 13 March 2013 between 08:35 and 09:35 UT

Another ARTEMIS observation of the lunar wake was made during high beta plasma conditions where the magnetic field lines were not perpendicular to the solar wind velocity upstream, which makes a different interesting condition for checking the accuracy of the method of characteristics. I compare the measured density from observations with results obtained from the method of characteristics in order to assess the validity of the model under these circumstances. This observation is chosen because the ambient plasma conditions were relatively steady [62]. Also, the angle between the magnetic field and the solar wind velocity,  $\alpha$ , was different from  $90^\circ$ . ARTEMIS P1 crossed the lunar wake on 13 March 2013 from 08:35 coordinated universal time (UTC) for about 60 minutes while P2 was in the solar wind. In this event, the Moon was located at  $[56.9, 19.8, 3.1] R_E$  Geocentric solar ecliptic (GSE) coordinate system, where  $R_E$  is the radius of the Earth [62]. ARTEMIS P1 entered the

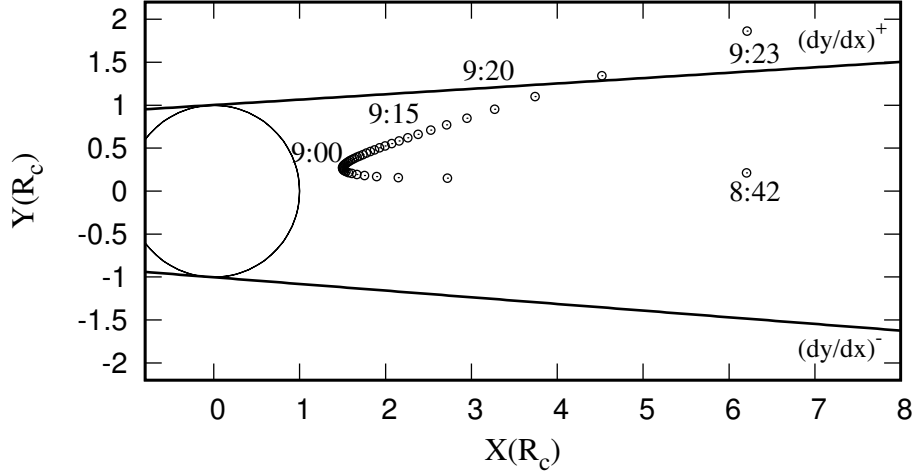


Figure 5.7: The trajectory of P1 spacecraft of ARTEMIS mission on 13 March 2013 between 08:35 and 09:35 UT is mapped to a 2D plane containing  $\mathbf{B}$  and  $M_{\perp}$ . The boundary of wake which is calculated with the method of characteristics is plotted.

wake from below where it was very close to the lunar surface  $\simeq 0.75R_m$  and left the wake from above at  $\simeq 2.0 R_m$ . The ambient plasma parameters were taken from ARTEMIS P2 where it is in the undisturbed area with ion and electron temperatures were  $T_i = 5$  eV and  $T_e = 9$  eV. The measured Interplanetary Magnetic Field was low  $\mathbf{B}_{IMF} = (-1.5, 0.0, -1.0)$  nT which gives a high beta plasma with  $\beta_e \simeq 7.8$  and  $\beta_i \simeq 4$ . The solar wind flow velocity and density were  $\mathbf{V}_{sw} = (-320.0, 15.0, 0.0)$  km/s and  $n_{sw} = 7.0 \text{ cm}^{-3}$  respectively. The vectors,  $\mathbf{B}_{IMF}$  and  $\mathbf{V}_{sw}$  are given in SSE coordinates. Measurements of the ambient plasma are taken from a paper published to measure the lunar diamagnetic fields in the wake [62]. In this paper, two ARTEMIS events are considered. In both cases, the plasma beta was significantly higher than normal. Measurements are compared with results from the hybrid simulations. Figure 5.7 shows the trajectory of P1 along with the predicted boundaries of the lunar wake from the analytic model in a 2D plane defined by  $\mathbf{B}$  and  $M_{\perp}$  during this flyby. It can be seen that, as measured relative to the radius of

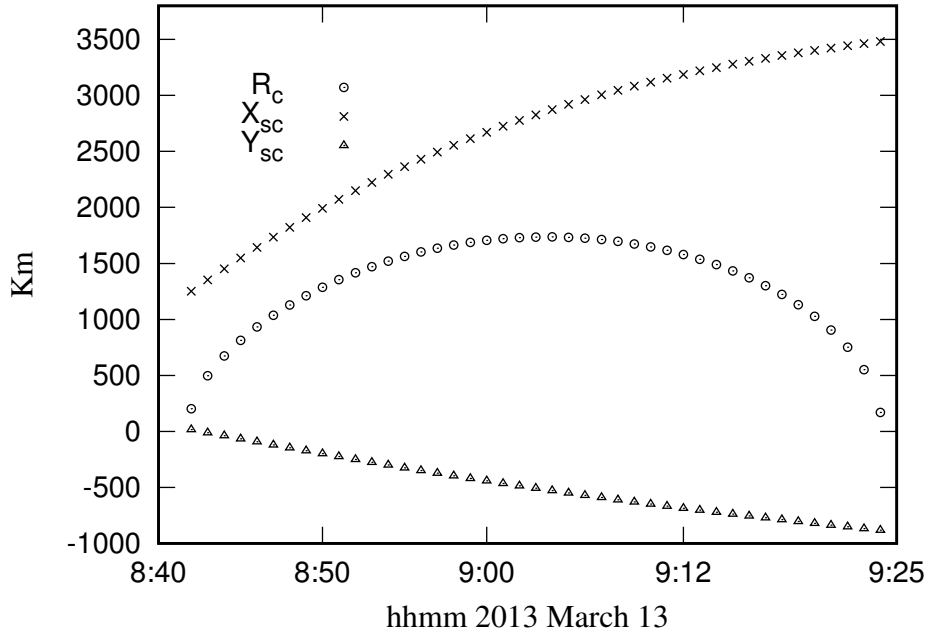


Figure 5.8: Coordinates related to the trajectory of P1 spacecraft of ARTEMIS mission on 13 March 2013 between 08:35 and 09:35 UT ( $X_{SC}$ ,  $Y_{SC}$ ) plotted with the corresponding radius of cross section  $R_c$ .

the 2D moon cross section, P1 is in the wake far from the Moon surface at the beginning of the flight at 8:42 UT. It gradually approaches the Moon surface and exits the lunar wake at 9:22 UT. The radius of the 2D cross section of the Moon, as well as the coordinates of P1 spacecraft, are plotted in Fig. 5.8. At the beginning 8:40 UT and the end 9:23 UT of the flyby the radius of the 2D Moon ( $R_c$ ) is small, but it increases in the middle of the flight at 9:00 UT. The density calculated with the method of characteristics, the finite element code and the one measured with ARTEMIS satellite through the flyby on 13 March 2013 are compared in Figure 5.9. The density obtained from the method of characteristics and the finite element model are in excellent agreement. Qualitatively, the density of the finite element model is higher in the center of the wake in comparison to the one from the method of characteristics. Quantitatively, the two densities agree within  $\simeq 5\%$  almost everywhere. The measured density from ARTEMIS on this event is entirely consistent with the results of the two models in the wake. Quantitatively, the three densities agree within  $\simeq 5\%$  with respect to the upstream density in the depth of the wake. However,

the wake measured density from ARTEMIS is to be broader compared with the results of the other models illustrated in Fig. 5.9. Mapping the 3D results from ARTEMIS to the 2D wake likely causes some of the differences between the results from observations and the models.

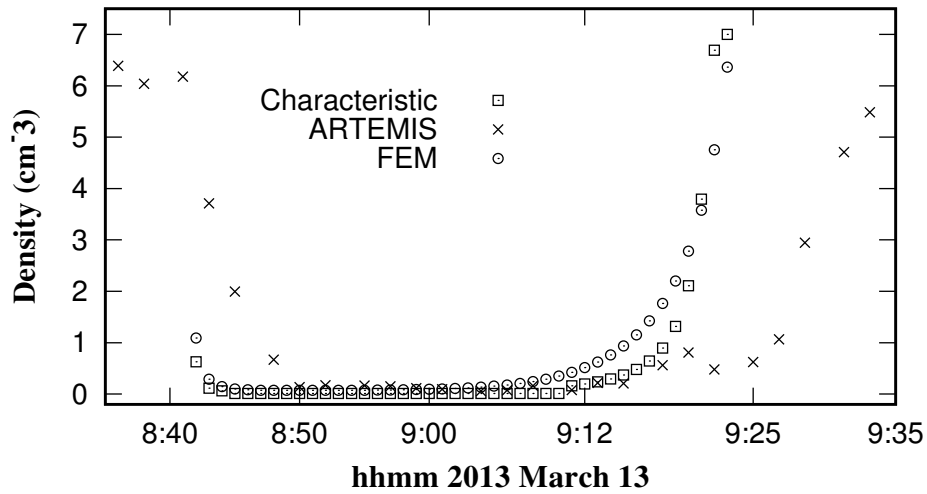


Figure 5.9: Ion density computed with the finite element model (FEM) compared with the ones from the method of characteristics and ARTEMIS data along the trajectory of the P1 spacecraft of ARTEMIS mission on 13 March 2013 between 08:35 and 09:35 UT.

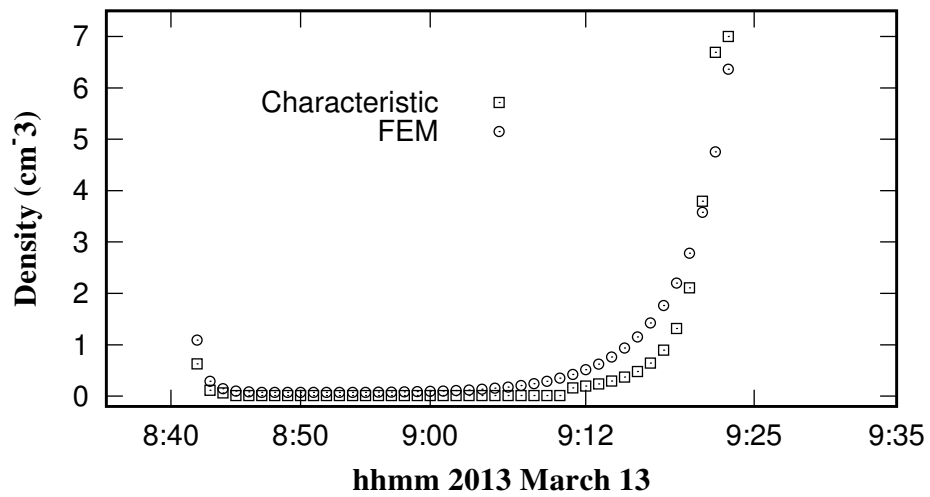


Figure 5.10: Ion density computed with the method of characteristics compared with the ones from the finite element model along the trajectory of the P1 spacecraft of ARTEMIS mission on 13 March 2013 between 08:35 and 09:35 UT.

# Chapter 6

## Summary and conclusions

In this thesis some important features of the interaction between the Moon and the solar wind in the night-side are investigated, using different models. The formation of the conical shape plasma depletion in the downstream region (the lunar wake) for two different magnetic field orientations is studied with kinetic and fluid approaches. Earlier works based on sophisticated 3D models including extensive physical processes have been developed and used to study this problem. These advanced models however, require considerable development time and computational resources. This has been the motivation for considering simplified two-dimensional models that can be solved analytically, or with relatively modest computational efforts. Each model reproduced some important features of the lunar wake while requiring significantly less computer time. More specifically, goals of this thesis are:

1. To assess the applicability of of four relatively simple and computationally fast models, to reproduce some of the main features of the lunar wake. This is done by making cross-comparisons between the different models, and by comparing model predictions with ARTEMIS observations.
2. To check the validity of the approximations made in in the construction of the fluid models, using test-particle simulations.

Four different models are presented to study the Moon-solar wind interactions and in particular the formation of the wake. They are, 1- the hybrid-kinetic, 2-

the analytic model, 3- the method of characteristics and, 4- the finite element model. Ions are treated as particles in the hybrid-kinetic model and as fluids in the other methods. However, electrons are approximated as an isothermal massless fluid in all approaches.

Two-fluid models are developed for the first time to account for the dynamics of the two counterstreaming ion fluids parallel to the magnetic field in which the interaction between the two fluids is taken into account (the method of characteristics) or not (the analytic model). These models are based on a 2D fluid approach first proposed by Hutchinson, [30], [31], [33] to study a single entry point of the lunar wake. The model relies on the fact that ions are strongly magnetized in order to reduce the 3D wake problem to an approximate 2D problem. All these methods (Hutchinson model, the analytic model and, the method of characteristics) are solved by using characteristics for a system of first order partial differential equations. Density, parallel velocity and parallel flux calculated from the two-fluid model with coupling (the method of characteristics) are compared with the ones in which coupling is neglected (the analytic model). Along the magnetic field lines, electric fields are proportional to the gradient of the logarithm of the density which is larger when coupling is not taken into account. This results in larger parallel speeds when coupling is ignored, and lower ones when it is taken into account. With the method of characteristics, in which coupling is taken into account, this is why plasma entering from below the wake, can be accelerated upward and cross the wake axis, and vice versa. Solutions found with the analytic model, in which coupling is ignored, show similar features, but in this case, nothing opposes the acceleration of either fluid, thus leading to larger parallel velocities. The results from the method of characteristics and the analytic model are in a relatively good agreement. This agreement indicates the neglect of the coupling between the two fluids in the characteristics analysis is a good approximation.

The 2D hybrid-kinetic electromagnetic model, previously used by Paral [58]

to model the solar wind interaction with the planet Mercury, is used in order to study the solar wind interaction with the Moon [18]. The variation of the magnetic field in the hybrid code was artificially turned off in the calculations in order to reproduce the assumptions made in the two-fluid models. The perpendicular velocity is assumed to be constant in the fluid models which is not the case in the hybrid approach. However, the normalized Mach number  $M_{\perp}$  is found to be constant within  $\sim 9\%$  in regions where the density is above 2.8% of the upstream solar wind density. This supports the assumption made in the fluid models that  $M_{\perp}$  is approximately constant.

The finite element code (TOPO) [48] is used to model the lunar wake. The validity of the finite element code is checked by reproducing analytic results for a simple shock polar problem. The shock angles obtained analytically are seen to be in agreement with computed values obtained with the finite element code. Quantitatively, the accuracy ranged from  $\simeq 1\%$  to  $\simeq 4\%$  in the range of parameters considered. When applied to the formation of the Moon wake, the expansion of ions along the magnetic field from the unperturbed region to the void area downstream of the Moon is simulated by considering ions as a single-fluid, a two-fluid with coupling and a two-fluid without coupling. The counterstreaming ion fluids in a non interacting two-fluid case can accelerate in the direction parallel to  $\mathbf{B}$  to have a large parallel velocity, because there are no forces opposing either fluid. However, in the single-fluid or two-fluid with coupling, plasma is prevented from reaching the opposite side of the wake, and the maximum parallel velocities are significantly lower. That is why plasma flow from below can reach the region above the  $Y = 0$  axis and vice versa, but less than when the fluids are not interacting. The main difference between the single-fluid models and the two-fluid approaches is that the parallel fluid velocity must vanish at  $Y = 0$  by symmetry, which is different from the two-fluid models, where the parallel velocity of either fluid (from below or from above) does not vanish on the  $Y=0$  axis. As a result, accumulation of ions on the axis farther downstream of the wake is larger in the single-fluid than in the interacting two-fluid test.

All these different fluid models were developed under certain approximations which limit the generality of the results. For example, in the hybrid code for stability purposes,  $\sim 15\%$  of the solar wind particles had to be injected into the wake in order to prevent numerical instabilities, which causes a higher minimum density calculated from this approach in comparisons to the ones from other approaches. Conversely, the finite element model creates the deepest wake of all models. The reason is that in the method of characteristics and the analytic model the parallel fluid velocities can become very large in comparisons to the ones in the finite element code. Another difference between these models was found at around  $X = 8R_m$  where the finite element shows an increase in density on the axis, absent with the other methods considered. That is related to the formation of the shock wave in the solar wind interaction with the Moon, which was pointed out in [53], [54] and was modeled with a hybrid code for the first time [34]. In fact, the boundary in the method of characteristics starts at around  $X = 2R_m$  where the boundary condition is constructed from the analytic model and the discontinuity does not appear in this analysis so the shock waves cannot be seen. Also, the formation of the shock wave is not captured in the hybrid-kinetic model because of the injection of the solar wind ions inside the wake. Cross comparisons between results from these models show that each model can capture various aspects of the physics of the lunar wake, and that all these models are found to agree qualitatively.

Two different ARTEMIS observations of the lunar wake with different interplanetary magnetic field orientations were reported for comparison purposes. In all approaches, the lunar wake was modeled in a 2D plane defined by the magnetic field and the solar wind velocity. ARTEMIS observations however, are made in a 3D actual wake. For comparison purposes, the 3D results measured with ARTEMIS were mapped into the 2D plane of  $\mathbf{V}_{SW} - \mathbf{B}$ . The depth of the wake from ARTEMIS data in its first flyby and from the finite element model is  $\sim 3.9\%$  of the background plasma density, while the one calculated

with the method of characteristics is higher by approximately 16.2%. Quantitatively, the density from the finite element model agreed within  $\simeq 3\%$  with the observed density from ARTEMIS almost everywhere except near the edge of the wake.

Moreover, ion particles were traced in the approximated fields assumed in the analytic model to calculate the distribution functions of ions inside the wake and in the unperturbed region using Liouville's theorem for a collisionless plasma, this was used to construct particle distribution functions on grid in velocity space. Then densities, velocities and stress tensor of ions are calculated by taking different moments of the obtained distribution functions. In the unperturbed region where the plasma is in thermodynamics equilibrium, the perpendicular velocity remains constant within  $\simeq 0.3\%$ , while in the wake region the discrepancy is higher of order  $\simeq 16\%$ . The maximum relative difference between the diagonal elements and the assumed pressure in the analytic model is of order 1.0%, and the off-diagonal elements are indicative of discretisation errors made in the test-particle method and the integration of distribution functions to obtain the second order moments. Therefore, I conclude that the assumptions were made in the analytic model constitute good approximations.

In conclusion, a result of the analytic model, which is not obtained from single-fluid numerical simulations such as MHD analyses, nor even from three-dimensional fluid codes, is an explicit expression for the parallel flow velocity of ions entering the wake from different locations around the Moon. In a fluid description of plasma, including multi-species models, only one density and flow velocity is considered for each species, whether that species is considered upstream or downstream of an obstacle. Thus, an important source of free energy and possible source of instability and turbulence in the wake is missing in these approaches. On the other hand, despite their simplicity, the simple two-dimensional models considered in this thesis, can reproduce some of the important features of the lunar wake such as density, parallel velocity and

particle flux as a function of positions which can then be used to benchmark model results against in situ observations.

**Future work** All the models considered are built under certain approximations which limit the generality of the results. For example, in the fluid models the assumptions are, 1- the magnetic field is uniform, 2- ions and electrons are isothermal fluids, 3- plasma is quasi-neutral, 4- the ion polarization drift is negligible, 5- electrons inertia is negligible, 6- the equation of state is that of an ideal gas and, 7- models are build in two dimensions. In future research one can improve these fluid models by avoiding some of these assumptions, in order to capture more of the physics. For example, one of the key goals of this thesis is to better understand the dynamics of ions expanding parallel to the magnetic field into the void region. Thus, extending the model to three dimensions, adding perpendicular drifts such as the polarization drift, the diamagnetic drift, and the  $\mathbf{E} \times \mathbf{B}$  drifts to the fluid equations should lead to significant improvements. On the other hand, a full pic code can be used to model the ions and electrons as particles to capture more physics in this interaction. More comparisons with ARTEMIS data considering other quantities such as, velocity, fluxes could also be considered in the future. Although the counterstreaming ion fluids can be captured by a 2D fluid models, an extension to three dimensions with kinetic descriptions should provide a significant improvement and lead to a better understanding of of the Moon wake dynamics problem.

# References

- [1] V. Angelopoulos, “The artemis mission,” *Space Sci. Rev.*, vol. 165, no. 1-4, pp. 3–25, 2011. 12, 23, 114
- [2] W. Baumjohann and R. A. Treumann, *Basic Space Plasma Physics*, 2nd. Imperial College Press, 1999, p. 159. 4, 5, 17, 28, 82, 105
- [3] W. Baumjohann and R. A. Treumann, *Advanced Space Plasma Physics*. London: Imperial College Press, 2001, p. 47. 4
- [4] A. Bers, *Handbook of Plasma Physics*. Amsterdam: North-Holland, 1983, p. 451. 22
- [5] A. Bhardwaj, M. Dhanya, R. Sridharan, S. Barabash, F. Yoshifumi, M. Wieser, M. Holmström, C. Lue, P. Wurz, A. Schaufelberger, and K. Asamura, *Interaction of solar wind with moon: An overview on the results from the sara experiment aboard chandrayaan-1*. World Scientific Publishing Co., 2012. 8
- [6] C. K. Birdsall and A. B. Langdon, “Plasma physics via computer simulation,” in. McGraw-Hill, 1985. 14
- [7] F. F. Chen, “Introduction to plasma physics and controlled fusion,” in, ser. Cambridge Atmospheric and Space Science Series. Springer US, 1984, pp. 2–3. 4
- [8] C. R. Chester, “Techniques in partial differential equations,” in. McGraw-Hill, 1970. 40
- [9] T. E. Cravens, “The solar wind interaction with planets and other solar system bodies,” in *Physics of Solar System Plasmas*, ser. Cambridge Atmospheric and Space Science Series. Cambridge University Press, 1997, pp. 270–342. 6, 7, 9
- [10] I. Crawford, M. Anand, C. Cockell, H. Falcke, D. Green, R. Jaumann, and M. Wicczorek, “Back to the moon: The scientific rationale for resuming lunar surface exploration,” *Planetary and Space Science*, vol. 74, no. 1, pp. 3–14, 2012, Scientific Preparations For Lunar Exploration. 12
- [11] J. Dawson, “Particle simulation of plasmas.,” *Reviews of Modern Physics*, vol. 55, no. 2, pp. 403–447, 1983. 14, 15

- [12] W. Farrell, M. Kaiser, J. Steinberg, and S. Bale, “A simple simulation of a plasma void: Applications to wind observations of the lunar wake,” *J. Geophys. Res. (USA)*, vol. 103, no. A10, pp. 23 653–60, 1998. 16
- [13] S. Fatemi, “Modeling the lunar plasma wake,” Licentiate Thesis, Luleå University of Technology, SE-971 87 Luleå, Sweden, 2011. 69
- [14] S. Fatemi, M. Holmström, Y. Futaana, S. Barabash, and C. Lue, “The lunar wake current systems,” *Geophysical Research Letters*, vol. 40, no. 1, pp. 17–21, 2013. 68
- [15] V. C. A. Ferraro and C. Plumpton, “An introduction to magneto-fluid mechanics,” in. Oxford: Clarendon Press, 1966. 77
- [16] M. O. Fillingim, J. S. Halekas, D. A. Brain, W. M. Farrell, Y. Futaana, M. Holmstrom, G. H. Jones, E. Kallio, T. Nakagawa, E. Roussos, and Y. Saito, “Kinetic Plasma Processes at Airless Bodies,” *AGU Fall Meeting Abstracts*, P43D–1938, Dec. 2012. 8
- [17] R. Fitzpatrick, *Theoretical Fluid Mechanics*. IOP Publishing, 2017. 80
- [18] H. Gharaee, R. Rankin, R. Marchand, and J. Paral, “Properties of the lunar wake predicted by analytic models and hybrid-kinetic simulations,” *JOURNAL OF GEOPHYSICAL RESEARCH-SPACE PHYSICS*, vol. 120, 2015. 20, 47, 68, 72, 85, 130
- [19] A. V. Gurevich, L. V. Pariiskaya, and L. P. Pitaevskii, “Self-similar motion of rarefield plasma,” *Soviet Physics JETP*, vol. 22, no. 2, 1966. 10, 25, 26
- [20] D. Gurnett and A. Bhattacharjee, “Introduction to plasma physics,” in. Cambridge University Press, 2004, pp. 75–85. 4, 17–19, 28, 69
- [21] J. Halekas, S. Bale, D. Mitchell, and R. Lin, “Electrons and magnetic fields in the lunar plasma wake,” *Journal of Geophysical Research: Space Physics*, vol. 110, no. A7, 2005. 10, 26, 61
- [22] J. Halekas, D. Brain, and M. Holmstrom, *Moon’s Plasma Wake*. New York: John Wiley and Sons, Inc., 2015. 6, 8, 23
- [23] J. Halekas, Y. Saito, G. Delory, and W. Farrell, “New views of the lunar plasma environment,” *Planet. Space Sci. (UK)*, vol. 59, no. 14, pp. 1681–94, 2011. 61
- [24] M. A. Hapgood, “Space physics coordinate transformations: A user guide,” *Planetary and Space Science*, vol. 40, no. 5, pp. 711–717, 1992. 116
- [25] Y. Harada, *Interactions of Earth’s magnetotail plasma with the surface, plasma, and magnetic anomalies of the moon*. Tokyo, Japan: Springer, 2015. 8, 11–13
- [26] E. Harnett and R. Winglee, “2.5D particle and MHD simulations of mini-magnetospheres at the moon,” *J. Geophys. Res. (USA)*, vol. 107, no. A12, pp. 4–1, 2002. 21

- [27] R. D. Hazeltine and F. Waelbroeck, “The framework of plasma physics,” in. Reading, Mass: Perseus Books, 1998. 107
- [28] M. Holmstrom, S. Fatemi, Y. Futaana, and H. Nilsson, “The interaction between the moon and the solar wind,” *Earth Planet. Space (Japan)*, vol. 64, no. 2, pp. 237–45, 2011. 17, 61, 68, 71
- [29] A. J. Hundhausen, “Composition and dynamics of the solar wind plasma,” in *Solar-Terrestrial Physics/1970*, E. R. Dyer, Ed., Dordrecht: Springer Netherlands, 1972. 5
- [30] I. Hutchinson, “Ion collection by oblique surfaces of an object in a transversely flowing strongly magnetized plasma,” *Phys. Rev. Lett. (USA)*, vol. 101, no. 3, 035004 (4 pp.) 2008. 10, 26, 129
- [31] I. Hutchinson, “Oblique ion collection in the drift approximation: How magnetized mach probes really work,” *Physics Of Plasmas*, vol. 15, no. 12, p. 123 503, 2008. 1, 10, 26, 30, 74, 129
- [32] I. Hutchinson, “Electron velocity distribution instability in magnetized plasma wakes and artificial electron mass,” *J. Geophys. Res., Space Phys. (USA)*, vol. 117, no. A03101, 2012. 31
- [33] I. Hutchinson, “Near-lunar proton velocity distribution explained by electrostatic acceleration,” *J. Geophys. Res., Space Phys. (USA)*, vol. 118, no. 5, pp. 1825–7, 2013. 10, 26, 30, 82, 129
- [34] P. Israelevich and L. Ofman, “Hybrid simulation of the shock wave trailing the moon,” *Journal of Geophysical Research (Space Physics)*, vol. 117, Apr. 2012. 61, 68, 92, 94, 131
- [35] J. D. Jackson, *Classical electrodynamics*. New York: Wiley, 1975. 78
- [36] H. K. Joumaa, “Analytic characterization of oblique shock waves in flows around wedges,” 2018. 80
- [37] J. Paral, “Hybrid-kinetic modelling of space plasma with application to mercury,” P.hD Thesis, University of alberta, Alberta, 2013. 69, 70
- [38] E. Kallio, “Formation of the lunar wake in quasi-neutral hybrid model,” *Geophysical Research Letters*, vol. 32, no. 6, pp. 1–5, 2005. 16, 68
- [39] K. Khurana, V. Angelopoulos, C. W. Carlson, G. T. Delory, W. M. Farrell, R. E. Grimm, I. Garrick-Bethell, J. S. Halekas, L. L. Hood, M. Horanyi, R. J. Lillis, R. P. Lin, C. R. Neal, M. E. Purucker, C. T. Russell, G. Schubert, D. G. Sibeck, and P. Travnicek, “Lunar science with artemis: A journey from the moon’s exosphere to its core,” *Planetary Science Decadal Survey*, p. 8, 2011. 10, 12, 23
- [40] S. Kimura and T. Nakagawa, “Electromagnetic full particle simulation of the electric field structure around the moon and the lunar wake,” *Earth Planets Space (Japan)*, vol. 60, no. 6, pp. 591–9, 2008. 16

- [41] M. G. Kivelson and C. Russell, "Introduction to space physics," in. Cambridge Unive. Press, 1995, p. 91. 5, 6
- [42] L. Krista, "The evolution and space weather effects of solar coronal holes," Oct. 2012. 5
- [43] P. K. Kundu, "Fluid mechanics," in. Academic. Press Inc., 1990, pp. 373–381. 18, 78
- [44] L. D. Landau and E. M. Lifshitz, "Fluid mechanics," in. Oxford: Pergamon, 1987, pp. 259–262. 18
- [45] A. Lipatov, U. Motschmann, and T. Bagdonat, "3d hybrid simulations of the interaction of the solar wind with a weak comet," *Planetary and Space Science*, vol. 50, no. 4, 2002. 16
- [46] H. Luhr, J. Wicht, S. A. Gilder, and M. Holschneider, "Magnetic fields in the solar system planets, moons and solar wind interactions," in. Springer Nature, 2018, pp. 4–5. 9
- [47] E. F. Lyon, H. S. Bridge, and J. H. Binsack, "Explorer 35 plasma measurements in the vicinity of the moon," *Journal of Geophysical Research (1896-1977)*, vol. 72, no. 23, pp. 6113–6117, 1967. 12
- [48] R. Marchand and M. Simard, "Finite element modelling of TdeV edge and divertor with ExB drifts," *Nuclear Fusion*, vol. 37, no. 11, pp. 1629–1639, 1997. 2, 76, 130
- [49] R. Marchand, "Finite element modelling of transport in a tokamak edge and divertor," *Plasma physics and controlled fusion*, vol. 44, no. 6, p. 871, 2002. 76
- [50] R. Marchand, "Test-particle simulation of space plasmas.," *COMMUNICATIONS IN COMPUTATIONAL PHYSICS*, vol. 8, no. 3, pp. 471–483, 2010. 2, 99
- [51] R. Marchand, M. Charbonneau-Lefort, M. Dumberry, and B. Pronovost, "Aranea, a program for generating unstructured triangular meshes with a java graphics user interface," *Computer Physics Communications*, vol. 139, no. 2, pp. 172–185, 2001. 76
- [52] A. Matthews, "Current advance method and cyclic leapfrog for 2D multi-species hybrid plasma simulations," *J. Comput. Phys.*, vol. 112, pp. 102–116, 1994. 69, 70
- [53] F. C. Michel, "Shock wave trailing the moon," *Journal of Geophysical Research*, vol. 72, pp. 5508–5509, 1967. 2, 92, 94, 131
- [54] F. C. Michel, "Magnetic field structure behind the moon," *J. Geophys. Res.*, vol. 73, pp. 1533–1542, 1968. 2, 61, 92, 94, 131
- [55] T. G. Northrop, "The guiding center approximation to charged particle motion," *Annals of Physics*, vol. 15, no. 1, pp. 79–101, 1961. 28

- [56] K. Ogilvie, R. Fitzenreiter, C. Owen, W. Farrell, J. Steinberg, A. Lazarus, and R. Torbert, "Observations of the lunar plasma wake from the wind spacecraft on december 27, 1994.," *Geophysical Research Letters*, vol. 23, no. 10, pp. 1255–1258, 1996. 10, 12, 25, 26, 61
- [57] B. P. V., U. V. V., and D. P. V., "Oblique shock wave reflection from the wall," *Naucno-tehniceskij Vestnik Informacionnyh Tehnologij, Mehaniki i Optiki*, no. 2, p. 338, 2015. 77
- [58] J. Paral and R. Rankin, "Dawn-dusk asymmetry in the kelvin-helmholtz instability at mercury," *Nat. Commun. (UK)*, vol. 4, 1645 (5 pp.) 2013. 2, 68, 70, 129
- [59] E. N. Parker, "Dynamics of the Interplanetary Gas and Magnetic Fields.," *The Astrophysical Journal*, vol. 128, p. 664, Nov. 1958. 5
- [60] G. K. Parks, "Physics of space plasmas," in. Westviews Press, 2004, pp. 496–499. 15, 17, 18, 69, 77
- [61] R. Pathria and D. Beale Paul, "Statistical mechanics,3rd ed.," in. Boston: Academic Press, 2011. 18
- [62] R. Poppe A., S. Fatemi, S. Halekas J., M. Holmström, and T. Delory G., "Artemis observations of extreme diamagnetic fields in the lunar wake," *Geophysical Research Letters*, vol. 41, no. 11, 2014. 23, 61, 114, 123, 124
- [63] E. Roussos, J. Müller, S. Simon, A. Böswetter, U. Motschmann, N. Krupp, M. Fränz, J. Woch, K. K. Khurana, and M. K. Dougherty, "Plasma and fields in the wake of rhea: 3-d hybrid simulation and comparison with cassini data," *Annales Geophysicae*, vol. 26, no. 3, 2008. 16
- [64] U. Samir, K. Wright, and N. Stone, "The expansion of a plasma into a vacuum: Basic phenomena and processes and applications to space plasma physics," *Reviews of Geophysics*, vol. 21, no. 7, pp. 1631–1646, 10, 25, 26
- [65] D. G. Sibeck, V. Angelopoulos, D. A. Brain, G. T. Delory, J. P. Eastwood, W. M. Farrell, R. E. Grimm, J. S. Halekas, H. Hasegawa, P. Hellinger, K. K. Khurana, R. J. Lillis, M. Øieroset, T.-D. Phan, J. Raeder, C. T. Russell, D. Schriver, J. A. Slavin, P. M. Travnicek, and J. M. Weygand, "Artemis science objectives," *Space Science Reviews*, vol. 165, no. 1, pp. 59–91, 2011. 61
- [66] N. R. C. Solar and S. P. S. Committee, "The sun to the earth and beyond: Panel reports," in. Washington, DC: National Academies Press, 2003. 20
- [67] T. H. Stix, *The theory of plasma waves*. New York, McGraw-Hill, 1962. 22
- [68] J. Tao, R. Ergun, D. Newman, J. S. Halekas, L. Andersson, V. Angelopoulos, J. Bonnell, J. McFadden, C. M. Cully, H.-U. Auster, K.-H. Glassmeier, D. Larson, W. Baumjohann, and G. M.V., "Kinetic instabilities in the lunar wake: ARTEMIS observations," *J. Geophys. Res. (USA)*, vol. 117, no. A03106, 2012. 16, 23, 49, 72, 85, 114, 1

- [69] G. Toth, B. van der Holst, I. Sokolov, D. De Zeeuw, T. Gombosi, F. Fang, W. Manchester, X. Meng, D. Najib, K. Powell, Q. Stout, A. Glocer, Y.-J. Ma, and M. Opher, “Adaptive numerical algorithms in space weather modeling,” *J. Comput. Phys. (USA)*, vol. 231, no. 3, pp. 870–903, 2012. 21
- [70] P. Travnicek, P. Hellinger, D. Schriver, and S. Bale, “Structure of the lunar wake: Two-dimensional global hybrid simulations,” *Geophys. Res. Lett. (USA)*, vol. 32, no. 6, 4 pp. 2005. 68
- [71] D. Vimercati, A. Kluwick, and A. Guardone, “Oblique waves in steady supersonic flows of bethe–zeldovich–thompson fluids,” *Journal of Fluid Mechanics*, vol. 855, 2018. 80
- [72] G. Voitcu, M. Echim, and R. Marchand, “Comparative study of forward and backward test-kinetic simulation approaches,” 2016. 100
- [73] J. Wang, X. He, and Y. Cao, “Modeling electrostatic levitation of dust particles on lunar surface,” *IEEE transactions on plasma science*, vol. 36, no. 5, 2008. 99
- [74] Y. C. Wang, J. Muller, W. H. Ip, and U. Motschmann, “A 3D hybrid simulation study of the electromagnetic field distributions in the lunar wake,” *Icarus (USA)*, vol. 216, no. 2, pp. 415–25, 2011. 16, 68
- [75] S. Wiehle, F. Plaschke, U. Motschmann, K. H. Glassmeier, H. U. Auster, V. Angelopoulos, J. Mueller, H. Kriegel, E. Georgescu, J. Halekas, D. G. Sibeck, and J. P. McFadden, “First lunar wake passage of ARTEMIS: Discrimination of wake effects and solar wind fluctuations by 3D hybrid simulations,” *Planetary and Space Science*, vol. 59, no. 8, pp. 661–671, 2011. 17, 23, 49, 72, 85, 114, 1
- [76] D. Winske, “Hybrid simulation codes with application to shocks and upstream waves,” in. Boston: Academic D. Reidel Publishing Company, 1985. 16, 67
- [77] L. Xie, L. Lei, Z. YiTeng, and D. Zeeuw, “Three-dimensional MHD simulation of the lunar wake,” *Sci. China Earth Sci. (China)*, vol. 56, no. 2, pp. 330–8, 2013. 21
- [78] H. Zhang, K. K. Khurana, Q. G. Zong, M. G. Kivelson, T. S. Hsu, W. X. Wan, Z. Pu, V. Angelopoulos, X. Cao, W. Y. F., Q. Q. Shi, W. L. Liu, A. M. Tian, and C. L. Tang, “Outward expansion of the lunar wake: Artemis observations,” *Geophysical Research Letters*, vol. 39, no. 17, 2012. 21
- [79] M. Zimmerman, W. Farrell, and A. Poppe, “Grid-free 2d plasma simulations of the complex interaction between the solar wind and small, near-earth asteroids,” *Icarus*, vol. 238, pp. 77–85, 2014. 8
- [80] M. Zocca, A. Guardone, G. Cammi, F. Cozzi, and A. Spinelli, “Experimental observation of oblique shock waves in steady non-ideal flows,” *Experiments in Fluids*, vol. 60, no. 6, May 2019. 77